



Doctoral School of Engineering / Applied Electronics /
Biomedical, Electromagnetism and Telecommunication Engineering

XXVIII CYCLE

**Processing and Quantitative Characterization of Skin Tissues Using
Optical Coherence Tomography and on Diagnostic Applications of
Electromagnetic Scattering**

Candidate: Saba Adabi

Supervisors:

Prof. Silvia Conforto

Prof. Lara Pajewski

Coordinator: Prof. Enrico Silva.....

To my parents Jeiran and Alireza who I love the most...

Acknowledgement

I want to take this opportunity to show my gratitude towards the people who have helped me in completing my PhD Thesis. First and the most, I want to deeply thank my mentors Prof. Silvia Conforto and Prof. Mohammadreza Nasiriavanaki. I appreciate all their contributions of time, ideas and lab facilities and to make my Ph.D. experience productive and stimulating. I thank my mentor Prof. Lara Pajewski who worked with me on electromagnetic scattering projects.

I appreciate the immense contribution of Prof. Daveluy and Prof. Mehregan from Wayne state dermatology department and Oakwood hospital for their help and fruitful discussion on the *in-vivo* OCT human studies. I wish to extend my warmest thanks to my friends and labmates in OPIRA lab, biomedical engineering department Wayne state university. I am grateful for my labmates in Roma Tre University, department of applied electronics engineering: Silvio, Carmen, Benish, as well as Dr. Micheala and Davide for being such a good friends and co-workers. I also thank my co-authors Anne, Elaheh Adeleh, Fabio, Faiza and Matin.

My gratitude is to my brother and my friends Fatemeh and Maryam for who they are...

To my parents who I love the most... and to the best sister in the whole world ; Sahar

Table of Contents

Introduction.....	7
1.1 Motivation and contributions.....	7
1.2 Organization of thesis	9
Background and Introduction	11
2.1 Optical Coherence Tomography	11
2.2 OCT system configurations.....	12
2.3 Light tissue interaction	15
2.4 Speckle theory and statistics in imaging system	17
2.5 Artifact mitigation in OCT imaging.....	20
2.5.1 Speckle reduction algorithms	20
2.5.2 Image blurring correction	22
2.7 Diagnostic applications of OCT in dermatology	24
2.7.1 Skin layer detection and Dermal-Epidermal junction localization.....	27
2.8 Summary	28
Intelligent speckle reduction algorithms	29
3.3 Intelligent Speckle reduction method.....	31
3.3.1 OCT speckle formulation with Rayleigh statistics.....	31
3.3.2 Implementation of the proposed method.....	32
3.3.3. OCT system	34
3.3.4 Experimental results and discussion	37
3.4 A Learnable Despeckling Framework	40
3.4.1 Digital filtering method.....	40
3.4.2 Feature extraction	42
3.4.3 Image quality assessment metrics.....	42
3.4.4 Learnable despeckling framework.....	44
3.4.2 Filter Classifier	45
3.4.5 Experimental Results and Discussions	47
3.5 Conclusions and outlook.....	54
A Cluster based Wiener Filtering method for OCT images	56
4.1 Introduction.....	56
4.2 Adaptive Wiener filtering	56

4.3 Cluster-based Wiener Filtering (CWF)	57
4.4 Optical phantom design	60
4.5 Results	61
4.5.1 Evaluation of clustering method on phantom images	62
4.5.2 Application of CWF on skin images	64
4.6 Discussion	67
4.7 Conclusion	68
Deconvolution methods for deblurring of OCT images	69
5.1 Introduction	69
5.2 Formalization of an iterative deblurring method based on Total Variation	70
5.3 Phantom construction for PSF extraction	72
5.4 Results and discussion	74
5.5 Conclusion	77
Localization of Dermal Epidermal Junction in OCT images of skin	78
6.1 Introduction	78
6.2 Methodology	78
6.3 Results and discussion	84
6.4 Conclusion	87
Universal in-vivo textural model for Human skin	88
7.1 Introduction	88
7.2 Materials and Methods	88
7.2.1 Data Analysis	89
7.2.3 Classification	90
7.2.4 Other imaging modalities	91
7.3 Results	92
7.3.1 Healthy skin in OCT images	92
7.3.2 Diseased skin in OCT images	94
7.3.3. Healthy skin analysis	95
7.3.4 Diseased skin; classification results	100
7.3.3 Imaging with other modalities	103
7.4 Discussion	107
7.5 Conclusion	108

Diagnostic applications of electromagnetic Scattering	111
8.1.2 Finite Difference Time Domain Modelling of cylindrical objects	112
8.1.3 Accurate wire-grid modelling of objects in a host medium.....	113
8.1.2 Objects partially hosted in different media	118
8.1.5 Arbitrary shaped objects	120
8.2 <i>Spectral representation of EM scattering from the objects in host medium.....</i>	121
8.2.2 Results	123
8.5 <i>Conclusion</i>	127
Electromagnetic thickness formulation for human arm layers toward soft tissue assessment	128
9.2 <i>Electromagnetic response of the structure.....</i>	130
9.2.1 Analytical model of human arm as a layered media	130
9.3 <i>Numerical verification</i>	132
9.4.1 Depth calculation formulation.....	132
9.5 <i>Numerical results and algorithm assessment.....</i>	134
9.6 <i>Conclusion</i>	135
Bibliography.....	136

Abstarct

Optical Coherence Tomography (OCT) is a non-invasive interferometry based technique that deals with many clinical applications including dermatology. Speckle noise in OCT images, degrades the image quality and makes the edges difficult to be resolved in the process of image reconstruction. Methods – both software and hardware – were developed to mitigate the speckle phenomenon in OCT images. Software based methods are post-processing techniques having the substantial privilege of being applicable in clinical environment where the hardware manipulation is impossible. In this thesis two different software-based speckle reduction methods are developed for OCT images; an adaptive cluster-based Wiener filter de-noising algorithm considering the architectural structure of skin layers, and an artificial neural network-based one referring to the statistical distribution of the speckle noise. Furthermore, a universal feature-based de-speckling framework using the inherent characteristics of the OCT image to select optimal filter, is demonstrated. Furthermore, to overcome this spatially variant blurriness problem, an iterative de-convolution total variation method is developed.

There is a critical need to systematically analyze OCT images of different sites and identify their significant qualitative and quantitative differences. Therefore, referring to structural OCT and intensity based data together with features dependent classification algorithms, a successful skin model has been developed via normal and cancerous classification. Prior to skin tissue characterization analysis, a skin layer detection algorithm based on graph theory for OCT images of skin is developed. The results of tissue analysis can be extended and added to OCT machine as a kernel for a less subjective cancer diagnosis.

In section2, this thesis deals with electromagnetic forward and inverse scattering problems for objects in a host medium, Finite Difference Time Domain (FDTD) modeling and signal processing associated with it.

Chapter 1

Introduction

1.1 Motivation and contributions

This work is originally contributed by two main topics both dealing with a computational pipeline for optical coherence tomography images of skin – i) OCT artifacts mitigations, ii) computational modeling and quantitative characterization of skin tissues using Optical Coherence tomograms – to introduce a human skin model through image feature analysis and pattern recognition.

Optical Coherence Tomography (OCT) is a non-invasive interferometry based technique that deals with many clinical applications including dermatology. Although OCT offers a submicron axial resolution of (1-15 micrometer) and can provide a fair penetration depth of 2-3 mm for bio-tissue characterization, the OCT images still suffer from some artifacts including a multiplicative grainy noise – called speckle – and blurriness. In the first part of this dissertation, methods and algorithms to mitigate those artifacts in OCT images were devised.

Speckle degrades the image quality and makes the edges difficult to be resolved in the process of image reconstruction. Methods – both software and hardware – were developed to mitigate the speckle phenomenon in OCT images. Software based methods are post-processing techniques having the substantial privilege of being applicable in clinical environment where the hardware manipulation is impossible. There are some digital filters devised to suppress the speckle in OCT images, mainly for ophthalmology application, but only few of them are based on the inherent characteristics of OCT images.

In this thesis two different software-based speckle reduction methods are developed for OCT images; an adaptive cluster-based Wiener filter denoising algorithm considering the architectural structure of skin layers, and an artificial neural network-based one referring to the statistical distribution of the speckle noise. Furthermore, a universal feature-based de-speckling framework using the inherent characteristics of the OCT image to select optimal filter, is demonstrated. On the other hand, due to imperfections of OCT components, in practice, an OCT setup cannot reach its theoretical resolution and generates blurred images. To overcome this spatially variant

blurriness problem, the Point Spread Function (PSF) of each sub-region of imaging system is estimated by using solid phantoms and then an iterative de-convolution total variation method is developed.

In the second part, referring to structural OCT and intensity based data together with features dependent classification algorithms, a successful skin model has been developed via normal and cancerous classification. According to specific functional needs, skin architecture varies across different parts of body, and so do the textural and morphological characteristics in the OCT images. There is, therefore, a critical need to systematically analyze OCT images of different sites and identify their significant qualitative and quantitative differences. It is demonstrated that such dynamic model in conjunction with decision-theoretic approaches can assist in the diagnosis of different microstructural cutaneous abnormalities, and hence aid in the determination of treatment. To this aim, a comprehensive analysis of in-vivo OCT healthy skin images for different sites of body in both epidermis and dermis is performed referring to their optical, textural, and statistical properties. Prior to skin tissue characterization analysis, a skin layer detection algorithm based on graph theory for OCT images of skin is developed. The proposed algorithm is performed in an interactive framework by a graphical representation of an attenuation coefficient map through a uniform-cost search method and a fuzzy-based nonlinear smoothing technique. The results of tissue analysis can be extended and added to OCT machine as a kernel for a less subjective cancer diagnosis. Furthermore, OCT images of specific sites have been compared to other imaging modalities in terms of visual inspection and speckle size.

The second section of this thesis deals with electromagnetic forward and inverse scattering problems for objects in a host medium, Finite Difference Time Domain (FDTD) modeling and signal processing associated with it. In this section, wire grid modeling of objects to pinpoint the scope of cost effective modeling for large arbitrary shaped objects is presented. Afterward, the results of spectral representation of Electromagnetic scattering from a cylindrical shape target by means of FDTD Modeling and its comparison with Cylindrical Wave Approach (CWA) is elaborated. Last but not the least the study of theoretical calculation of different layers of the human arm's thickness by using electromagnetic techniques in order to estimate the thickness of soft tissues is presented.

1.2 Organization of thesis

The work presented in the thesis is organized in two Sections and several chapters.

Section 1

In Chapter 2 a background on OCT technology fundamentals including speckle phenomenon, and configurations of OCT with application in dermatology are given. Afterward, an overview on current methods of artifacts suppression in OCT images, including speckle reduction and de-blurring techniques, is elaborated in this chapter.

In Chapter 3 firstly the effective developed algorithm for speckle suppression of OCT images (i.e. a Neural network based speckle reduction filter) and its evaluation is explained in detail. Then, the designed feature based framework for speckle suppression of OCT imaging of the skin is described.

In Chapter 4, the development of a cluster based Wiener filtering method for speckle reduction of OCT images and its results are elaborated.

Chapter 5 deals with developing the de-convolutional algorithms to overcome blurring artifact in OCT images and its comparison with few existing methods.

In Chapter 6, a skin layer detection algorithm based on graph theory for OCT images of skin is presented.

Chapter 7 deals with skin tissue characterization to systematically analyze OCT images of different sites and identify their significant qualitative and quantitative differences. Then a computational skin-modeling framework based on textural, geometrical, optical and morphological features for tissue characterization using pattern recognition is explained.

Section 2

In Chapter 8 an in-depth investigation of wire-grid modeling of objects in a host medium is presented. Moreover, the spectral representation of electromagnetic scattering from cylindrical shapes target by means of FDTD Modeling and its comparison with Cylindrical Wave Approach (CWA) is elaborated.

Chapter 9 deals with the theoretical calculation of different layers of the human arm by using electromagnetic techniques in order to estimate the thickness of soft tissues.

Section 1

Chapter 2

Background and Introduction

2.1 Optical Coherence Tomography

Optical imaging uses light to interrogate the morphological information of the compartments within a sample tissue. Optical imaging technologies can represent the internal structure of the sample across a range of spatial scales from micrometers to centimeters. Confocal Microscopy (CM) and Optical Coherence Tomography (OCT) are two modalities that work with the same principle. In CM [1], point illumination with a spatial pinhole is used in an optically conjugate plane in front of the detector to eliminate out-of-focus light. In CM, the depth resolution is inversely proportional to the square of the numerical aperture of the microscope objective lens. OCT is a non-invasive, non-ionizing optical imaging technique that is based on low coherence interferometry [2]. To form an OCT image, the magnitude and the time delay of the backscattered infrared light returned from a biological sample, are measured transversally [3, 4].

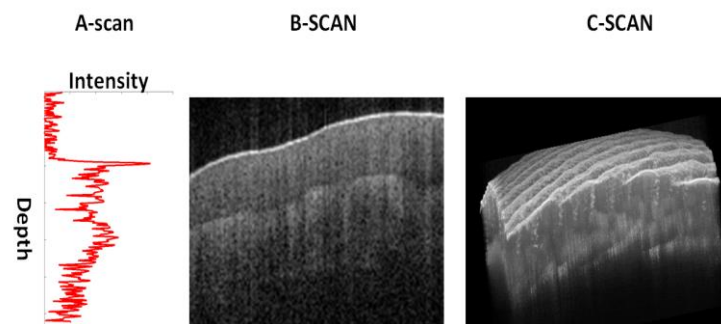


Figure 2.1 Measurements of backscattering versus depth in A-scans. B scan images displayed by a gray scale, are produced by scanning the OCT beam in a transverse direction to acquire a series of axial scans, Raster scanning of a stack of B-scans generates a 3D OCT image.

OCT is currently utilized in several medical and biomedical applications including dermatology [5] since it provides high resolution images and a moderate penetration depth, e.g., one to three millimeters.

Recently, OCT has been used as an optical biopsy method for differentiating among different tissues, e.g., healthy versus tumorous [6, 7]. Quantitative analysis of OCT images through extraction of optical properties has made OCT an even more powerful modality [8-10]. An OCT system is characterized by several parameters such as imaging speed, lateral and axial resolutions and penetration depth [11]. Figure 2.1 shows the OCT axial scan, cross section and volumetric images.

2.2 OCT system configurations

OCT is categorized into three types; time-domain OCT (TD-OCT), spectral domain OCT (SD-OCT) and swept source OCT (SS-OCT).

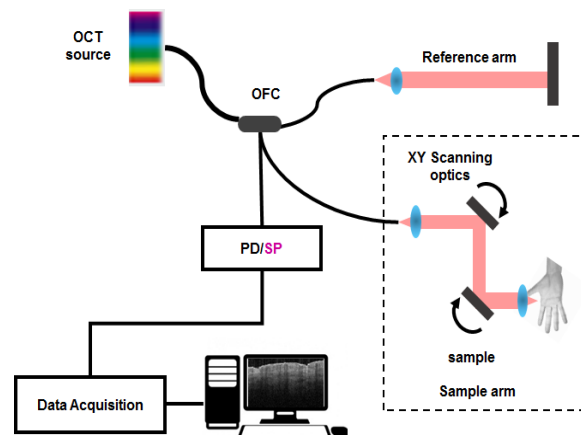


Figure 2. 2 Simplified schematic diagram of OCT imaging systems, OFC, Optical Fiber Coupler (OFC), PD(Photodetector), SP(spectrometer)

Conventional TD-OCT [12] normally consists of a light source, a splitter, lenses and two arms – a movable reference arm and a sample arm respectively. The output of the photo-detector is the auto-correlation (interference) of constructive fringe due to the coherence length of the light source. An OCT image is constructed based on the principle of time of flight and low coherence interferometry [13]. Fercher et al. in 1988 [14]

reported the first biological application of low-coherence interferometry by the measurement of the axial eye length. The interferometry is used to magnify the very small time delay between the backscattered light returned from the sample and the reflected light from a reference mirror. The basic components of an OCT system are a low coherent light source to be able to have the capability of sectioning the depth, a beam splitter to split light between two arms, a reference mirror, and some opto-electronic components such as objective lenses and XY galvo scanner [15].

The reflected light returned from the reference mirror (i.e corresponding mean intensities of the beam at reference and sample arms) is combined to form an interference signal at the photo-detector. It is possible to identify intensity peaks due to sharp refractive index variations between layers of the sample. Thereby, it is possible to infer about the structure of the studied sample.

The peak of the envelope of the interference signal is considered as one-pixel value of the OCT image corresponding to the sample point illuminated by the laser beam [3]. Performing a multiple scan in lateral directions, and moving the reference mirror can form a three-dimensional image. In the OCT technology, the transverse resolution is independent from axial resolution that is a distinctive feature of OCT compared to similar imaging modalities such as confocal microscopy [16]. The interference between the wavefront, coming back from the reference and sample arms, takes place only when the optical path difference is within the coherence length of the source. FD-OCT is realized in two ways: SD-OCT and SS-OCT.

In SD-OCT a detectors array captures the broadband spectral distribution of the light. The depth image is depended on the number of detectors in the array. To obtain the A-scan (amplitude-depth signal) a Fourier transformation is required. The advantages of this system over Time Domain OCT include higher sensitivity, greater sampling rate and recording speed and improved depth detection [12]. However, the decrease of the Signal to Noise Ratio, due to inadequate line-width, is the shortcoming of this technique.

SS-OCT [21] or time encoded frequency domain OCT privileged from merging all advantages of the two aforementioned systems by employing a tunable narrow line width laser. This source sweeps through wide optical bandwidth and gives a fine resolution and an improved SNR. Moreover, the detectors in SS-OCT are cost-effective photodetectors. In swept source OCT, a narrowband swept laser and a standard single element

photodetector detects the interference between light on the reference and sample arms. The axial reflectivity profile (A-scan) is obtained by applying the discrete Fourier transform (DFT) to the sampled detector signals. Some of the advantages over FD-OCT are lower sensitivity fall-off, higher image acquisition, higher detection efficiencies, and the opportunity to implement dual balanced detection [17].

The acquired SS-OCT signal is a photocurrent integrated over the line width δk of the swept laser source and can be given by equation (2.1).

$$i_{ss}(k) = \int_k^{k+\delta k} S(k) \cos(2\pi kz) dk \quad (2.1)$$

where k is the optical wavenumber, z is the optical path length difference between the sample and the reference arms, and $S(k)$ is the source's spectral density. Swept-source OCT offers a sensitivity advantage over typical TD-OCT systems. The signal to noise ratio of an SS-OCT system, for a single sample reflector, is driven by equation (1.2).

$$SNR_{SS-OCT} \approx M \frac{\rho R_S S_{TD-OCT}}{4q_e B_{SS-OCT}} \quad (1.2)$$

Where M is the number of samples, ρ is the detectors's responsivity, R_S is the sample reflectivity, S_{TD-OCT} is the sample's illumination power integrated over M and B_{SS-OCT} is the noise equivalent bandwidth of the system since depends on the frequency of the sweep, the SNR is affected by the properties of the used light source.

The selection of a laser source for SS-OCT is paramount and must consider several parameters such as wavelength sweep range, sweep repetition rate, the linearity of the sweep, radiant power, and instantaneous line width [21]. One of the most convenient sources for SS-OCT that meets the necessary criteria is Fourier-domain mode-locked laser (FDML), combining good imaging speed, instantaneous coherence length, and adequate spectral width [22]. This type of laser leads to an increase in imaging speed and depths. FDML lasers are based on a fiber-ring geometry with a semiconductor optical amplifier (SOA) as a gain medium, and a fiber Fabry-Perot filter as the tunable, narrowband optical bandpass filter. In FDML, a dispersion managed line is incorporated into the laser cavity and the narrowband filter is tuned periodically at the cavity round-trip time, producing a quasi-stationary operation mode. Light from one frequency sweep propagates through the laser cavity and returns to the filter at the

exact time when the transmission window of the optical bandpass filter is tuned to the same optical frequency. Consequently, light from the previous round trip is coupled back to the gain medium [28].

In OCT, the transverse resolution is associated with the focal length of the objective lens, and the axial resolution that is given in equation (2.3) is determined based on the coherence length of the light source used in the configuration of OCT; the shorter the coherence length, the finer the axial resolution is [1].

$$l_c = \frac{2c \ln(2) \lambda_0^2}{\pi \Delta \lambda} \quad (2.3)$$

where λ_0 is the central wavelength and is the Full Width Half Maximum (FWHM) of the power spectrum of the light source [3]. Important parameters of OCT imaging system are given in Figure 2.3.

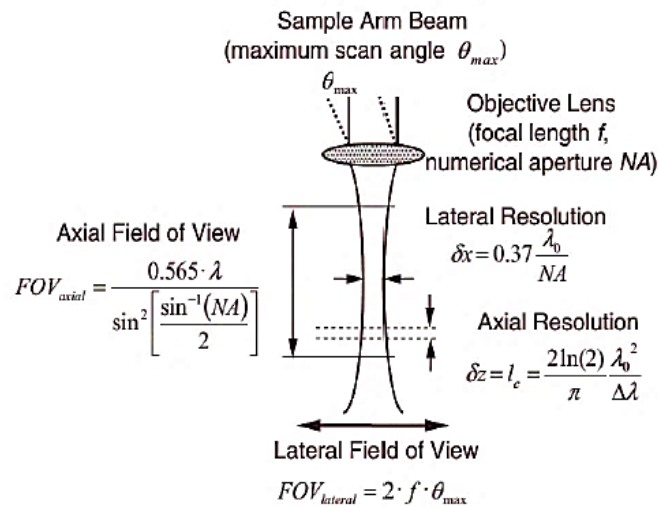


Figure 2. 3 Important OCT imaging parameters adopts from [8]

2.3 Light tissue interaction

Understanding how light penetrates biological tissues is essential to comprehend the different imaging modalities based on laser-tissue interaction.

In the tissue, photons may scatter, change their direction of flight based on the probability function or excite the absorbing molecule by an electronic transition. *Scattering* in biological tissues takes place when there is an alteration in the propagation direction without loss of energy. The scattering structures can be macroscopic like skin layers or they can be microscopic like cells. If the average distance between particles is greater than scatter size and wavelength, the single scattering theory can be applied. Mie or Raleigh theories can explain scattering of light by spherical particles. Mie theory obtains scattering coefficient by computing scattering efficiency, anisotropic factor (zero for Raleigh and 1 for Mie) and scattering cross section. The percentage of light reflected from tissue (reflectivity) is related to the scattering coefficient and to the part of light that is back scattered. Rayleigh scattering is rather isotropic, only depending on the polarization and the wavelength.

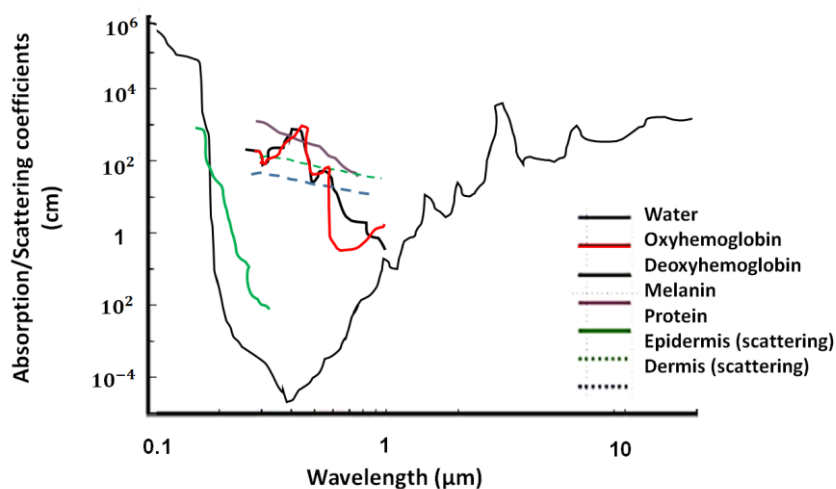


Figure 2. 4 Absorption and scattering spectra of tissue chromophores

Absorption by a chromophore causes either a quantized change in the distance between charges or a vibration transition. Absorbing molecular components of the tissue are porphyrin, hemoglobin, melanin, flavin, retinol, nuclear acids, deoxyribonucleic acid (DNA)/ribonucleic acid

(RNA). The effective cross section of a chromophore can be computed by multiplying the effective cross-section of absorption by the geometrical cross section. The absorption coefficient is $\mu_a = \rho_a \sigma_a$ (cm^{-1}) where ρ_a is the volume density of many chromophores.

In the near infrared and mid-infrared regions, the tissue absorption is dominated by water absorption, with the maximum at 3 μm . The inverse of the absorption coefficient defines the penetration depth (mean free path) into the absorbing medium. The Beer-Lambert's law, given by equation (2.4), allows to calculate the transmission of light through a slab with d dimension.

$$T = \frac{I}{I_0} = \exp(-\sigma_a N_a l) = \exp(-\mu_a l) \quad (2.4)$$

Where σ_a is the effective cross section absorption, N_a is the density of the absorbing molecules, l is the optical path, μ_a is the absorption coefficient. Figure 2.4 shows both absorption and scattering spectra of the tissue chromophores.

2.4 Speckle theory and statistics in imaging system

When a random medium employs a coherent light, a random intensity distribution – called speckle – will appear. Speckle, in fact, is a result of the interference of several elementary waves with random phases. Generally, there are two types of speckles: subjective and objective. Subjective speckles are generated in the image space of an optical system while objective speckles are produced in a free space. As biological tissues are considered non-uniform, the speckle phenomenon can cause errors in the related measurements. Therefore, speckle should be suppressed. The average speckle size in the far-field zone is $d_{ave} = \lambda/\varphi$, where λ the wavelength is and φ is the angle of observation. A temporal oscillation of the scattered field can be observed when imaging an object and moving the observation points. The amplitude of the transmission coefficients of a bio-tissue (a random phase screen) is given by the equation (2.5).

$$T_{Sp} = T_0 e^{(-i\Phi(x,y))} \quad (2.5)$$

Where T_0 is the independent amplitude, $\Phi(x, y)$, the random phase shift at (x, y) , is due to refractive index or thickness changes from point to point and it is given by equation (2.6).

$$\Phi(x, y) = \left(\frac{2\pi}{\lambda}\right) (n(x, y) - 1)h(x, y) \quad (2.6)$$

This phase fluctuation is also related to both standard deviation and optical length with a probability density function of Gaussian variations. The first order statistical properties of speckle are defined based on intensity probability distribution function (PDF) and contrast. Considering the ideal situation of scattered light with amplitude characterized by Gaussian statistics, the value of contrast is equal to 1. Hence, the PDF of individual speckle patterns from the most biological tissues is given by equation (2.7) and it shows that the destructive interference follows with the utmost probabilities.

$$p(I) = 4 \left(\frac{1}{I^2}\right) e^{\left(-\frac{2I}{I}\right)} \quad (2.7)$$

Equation (7) is a result of multiple scattering (the incoherent combination of two or more speckle patterns). For a single scattering event the equation (7) becomes $p(I) = \left(-\frac{1}{I}\right) e^{\left(-\frac{1}{I}\right)}$. There is also a partially developed speckle contribution where the contrast of speckle is smaller than unity and non-scattered components of the coherent beam interfere with the speckle field.

Using the cross-correlation function, the statistical behavior of the dynamic speckle (second order) can be explained by illumination conditions of the object for the formation of speckle patterns [18].

The Fresnel approximation in diffraction theory provides the speckle pattern by equation (2.8) [19].

$$E_{image} = \iint_{-\infty}^{\infty} d\xi d\eta E_{ob}(\xi, \eta) h(x, y; \xi, \eta) \quad (2.8)$$

Where E_{image} is the field in the image plane, $E_{ob}(\xi, \eta)$ is the field in the object plane and $h(x, y; \xi, \eta)$ is the point spread function (SPF) of the optical system between the object and the image planes.

The simplest configuration is the free space propagation. For biological tissues (considered as random media) based on Shapiro's calculation [20], the resulting field is given by (9) and it is expected to be Gaussian.

$$\langle E(r + \Delta r)E^*(r) \rangle = \exp\left(-\frac{\Delta r}{2l}\right) \frac{\sin(k\Delta r)}{k\Delta r} \quad (2.9)$$

Where r is a point on random medium, located at a small distance away and it is scattering mean free path, and k is wave number.

Using the spatial correlation of the image plane field given in equation (2.10), the speckle size in an imaging plane can be determined [21, 22].

$$\begin{aligned} \langle E_{im}(x_1, y_1)E_{im}^*(x_2, y_2) \rangle = \\ \iint_{-\infty}^{\infty} d\xi d\eta \iint_{-\infty}^{\infty} d\xi' d\eta' h(x_1, y_1; \xi, \eta) h^*(x_2, y_2; \xi', \eta') \times \\ \langle E_{ob}(\xi, \eta)E_{ob}^*(\xi', \eta') \rangle \end{aligned} \quad (2.10)$$

Considering that the mean intensity of the object plane is constant, after a variable substitution, equation (2.10) can be converted into (2.11).

$$\langle E_{im}(x + \Delta x, x + \Delta y)E_{im}^*(x, y) \rangle = \iint_{-\infty}^{\infty} d\xi' d\eta' h(\xi', \eta') h^*(\xi' - \Delta x, \eta' - \Delta y) \quad (2.11)$$

The intensity spatial correlation is computed by equation (2.12) after some math.

$$\begin{aligned} \langle I_{im}(x + \Delta x, x + \Delta y)I_{im}^*(x, y) \rangle = \langle I_{im} \rangle^2 \left[1 + \right. \\ \left. \left| \text{jinc}\left\{\frac{D}{2\lambda f} \sqrt{\Delta x^2 + \Delta y^2}\right\} \right|^2 \right] \end{aligned} \quad (2.12)$$

Where I_{im} is obtained by (13).

$$\langle I_{im} \rangle = \langle I_{ob} \rangle \iint_{-\infty}^{\infty} d\xi' d\eta' |h(\xi', \eta')|^2 \quad (2.13)$$

The width of the normalized plot of this intensity gives the mean speckle size in the speckle intensity pattern.

2.5 Artifact mitigation in OCT imaging

OCT imaging is a favorable high-resolution imaging method in medical and biomedical applications, and even if many modifications have already been applied on the OCT hardware and software the OCT images still suffer from artifacts. Two major artifacts in OCT images are speckle noise and blurring

2.5.1 Speckle reduction algorithms

In the OCT imaging, if the central wavelength of the light source is equal to or larger than the compartments within the sample under investigation, the interference of the reflected light with different amplitudes and phases generates a grainy texture in the image called speckle. Speckle degrades the quality of OCT images, particularly the borders of cellular layers [23]. The probability density function (PDF) of the speckle is approximated by Rayleigh distribution, or Rician distribution [24]. The speckle pattern is highly dependent on the microstructural content (size and density) of the sample being imaged. Due to such correlation, speckle is also known to carry some morphological information, thus it is not appropriate to consider it as an image noise. This issue has made finding a suitable solution to reduce the speckle quite challenging.

The speckle reduction methods are categorized into two main classes: software based and hardware based methods [8, 23, 25-32].

Software based speckle reduction methods rely on a mathematical model of the speckle, and they can be classified into adaptive and non-adaptive filters. The former is implemented based upon the local first order statistics, such as mean and variance, while the latter are implemented based on the overall statistics in the image. Software-based techniques mostly depend on digital filtering including Lee Filter (Lee) [33], the Hybrid Median Filtering (HMF) [34], and the Adaptive Wiener filter [39], Wavelet based methods [35], Wavelet based methods [11, 32, 36-38] and the diffusion-based method of thresholding with fuzzy logic [39]. Wiener filter is one of the most popular adaptive methods [40, 41]. Some of the non-adaptive algorithms are Kuwahara filter, Hybrid Median filter, Enhanced LEE filter (ELEE), Symmetric Nearest Neighborhood (SNN), thresholding with fuzzy logic [39] [42]. Wavelet based de-speckling has been a successful method in which the image is decomposed into its wavelet sub-bands, allowing to differentiate noise components through some signal processing [11, 32, 36-

38]. Considering the importance of the wavelet mother function in this method, Haar mother function has proven to be a fast and efficient solution, enabling speckle noise reduction without substantially diminishing contrast or spatial resolution in the image [43].

Ozcan et al. [40] concluded that by applying an enhanced-Lee or Wiener filter to OCT images of ex vivo bovine retina, the obtained OCT images were significantly improved. Wavelet-based despeckling methods [11, 32, 36-38] and a diffusion-based method with fuzzy logic thresholding [39] demonstrated better results compared to the previous techniques. In another study, Wu et al. developed a speckle reduction method using a total variation concept and first-order statistics extracted from OCT images, e.g., mean and variance [44]. Recently an adaptive speckle reduction method has been developed based on artificial neural networks (ANN) [45, 46]. ANN offer an intelligent solution that reduces speckle while preserving the morphological information of the image. In this method, the speckle is first modelled. A forward ANN trained by back-propagation is then used to estimate a noise parameter for the image, followed by a numerical solution to the inverse Rayleigh distribution function [47]. An improved version of this method is presented in next chapter [48].

The most common hardware-based speckle reduction method is the compounding. In compounding techniques [49], partially de-correlated images acquired from stationary samples are averaged. The quantities to be averaged specify the compounding procedure. Some of the quantities used in compounding methods are backscattering angles, central wavelengths, polarizations, and displacements. These results in techniques referred to as angular compounding, frequency compounding, polarization compounding, and spatial compounding, respectively [2, 28, 50, 51]. For instance, in the spatial compounding method, the averaging quantity is the tissue or the imaging probe motion, which comes from the inherent imperfection of the scanners used in the configuration of the imaging system [52]. Five different algorithms including averaging, random weighted averaging, random pixel selection and random pixel selection plus median filtering are used in another study to average their partially correlated images obtained from the spatial compounding method [52]. The authors demonstrated that the random pixel selection plus median filtering method is an efficient, simple, and edge-preserving de-speckling method compared to the common averaging method an artificial neural network based (ANN) method for speckle reduction has been introduced by

modeling the speckle using a Rayleigh distribution with a single noise parameter, sigma, for the entire image. The algorithm was tested on OCT images of *Drosophila* larvae [45-47, 52, 53]. However, there are still some deficiencies with existing algorithms to be addressed by developing new methods.

2.5.2 Image blurring correction

Blurriness stems from wavefront aberration in the imaging system [54]. The aberration is produced by the imperfections of optical devices that are used in the imaging systems and can result in resolution and contrast degradations. The most common way to reduce aberration is to use an adaptive optics (AO) system. AO systems are composed of i) a wavefront sensor (WFS) to measure the wavefront distortion, ii) a deformable mirror (DM), or a spatial light modulator (SLM) to correct the distortion, and iii) a control loop algorithm to control the correction process [55]. Recently, less-expensive sensor-less AO methods utilizing blind optimization have been studied [56-58].

In a sensor-less AO system, an optimization algorithm with a cost function, e.g. photo-detected intensity value, is used. The improvement of the cost function reduces the aberrations so resulting in less blurred images. Some of the effective optimization methods used in sensor-less AO systems are simulated annealing (SA) algorithm, genetic algorithm (GA), and particle swarm optimization (PSO) [53]. The performance of these three optimization methods have been compared in a sensor-less AO systems in [59].

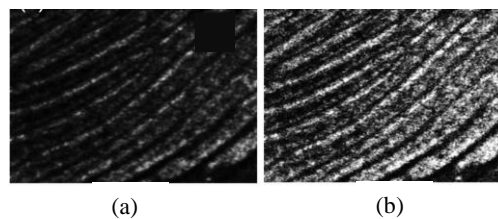


Figure 2. 5 OCT images of fingertip skin of a healthy individual (a) before and (b) after de-blurring procedures [59].

The other popular method to reduce blurring is deconvolution. In an imaging system, the output image can be interpreted as the convolution of the point spread function (PSF) of the system, $h(x,y)$, with the input signal generated by the interaction of the light with the sample. Lucy-Richardson [9] is the most popular iterative algorithm and the Wiener deconvolution [10] is the most preferred non-iterative algorithm. Multiple deconvolution techniques have been studied [60-64]. For some deconvolution methods, the point spread function (PSF) of the imaging system needs to be determined. There are two main methods to obtain the PSF; (a) analytical methods, (b) experimental methods based on imaging very small particles embedded in a solid tissue-mimicking phantom. Fish et al. successfully used the Lucy-Richardson algorithm, which is a well-established deconvolution algorithm, to deblur OCT images [65, 66]. Lucy-Richardson algorithm is based on the maximum-likelihood calculation to recover an undistorted image that has been blurred by a known PSF [66]. The calculation of the PSF based on phantoms is influenced by the phantom's size that needs to be correctly defined. As it is shown in Figure 2.6 only the green rectangles have the suitable size for PSF calculation, able to include almost one bright scatterer in the region of interest.

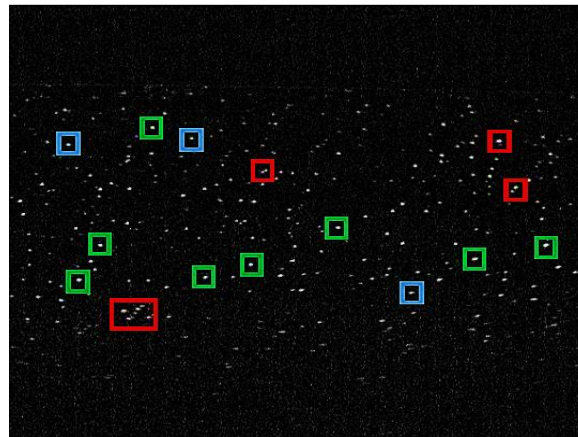


Figure 2.6 OCT optical phantom with different regions of interest to calculate PSF, only green ones are the correct ones

2.7 Diagnostic applications of OCT in dermatology

Histopathology is the golden standard especially for cancer diagnosis. Even if invasive and characterized by a high rate of false negatives, optic in medicine is still a promising approach due to the chance of approaching the cellular resolution. The comparison of different imaging modalities in terms of penetration depth and resolution, given in Figure 2.7, demonstrates that deeper imaging necessitates sacrificing spatial resolution. As matter of fact, OCT fills the gap between ultrasound (US) and Confocal Microscopy (CM). The resolution of US systems depends on the frequency of the sound wave used for imaging [67, 68] and it varies from 1mm to about 15 μ m. However, these high frequencies are greatly attenuated in the tissues so limiting the depth of penetration. On the other hand, the CM, with a high transverse image resolution of 1 μ m, is limited due to the dependence of the “depth performance” on the aperture of the microscope objective.

The foremost difference between US and OCT relates to the speed of light (3e8 m/s) and the speed of sound (only 1500 m/s). Due to femtoseconds time resolution of light, the direct electronic detection of light is almost impossible and measurement methods such as optical gating, optical correlation or interferometry are needed.

Currently clinical diagnosis of skin is including trained eye, palpation of the lesion and use of the ‘dermoscope’. For problematic lesions only a skilled histopathologist must perform a detailed biopsy. However, biopsy is invasive, leaves scars and cannot be repeated at the same site. Furthermore biopsy is not able to map the edges of a tumor [69].

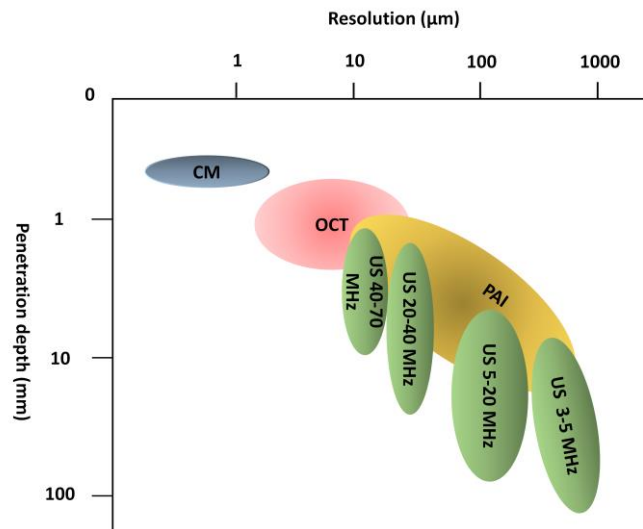


Figure 2.7 Resolution and depth tradeoffs in optical imaging modalities, Confocal Microscopy (CM), Optical Coherence Tomography (OCT), Ultrasound (US) and Photoacoustic Imaging (PAI)

OCT allows in-situ real time investigation of micromorphology and pathology without invasive tissue removal, thus allowing the same tissue sample to be monitored over time with repeated imaging. The desired wavelength to monitor skin with OCT is the 1300 nm where the scattering is governing phenomenon because of a fair conciliation between resolution of image and depth penetration [5]. Figure 2.7 shows a cartoon of skin compartments, their corresponding equivalent histology and OCT images. Welzel et. al published the first papers demonstrating the OCT for healthy skins and for diseased skin. Since there are some features of skin that can be clearly displayed such as sweat ducts and dermal epidermal junction, the OCT image interpretation is a topic of many current researches. The effectiveness of OCT has been shown in evaluation of skin cancer, various inflammatory and blistering skin conditions, physical and chemical skin damage, therapeutic effects, and surgical interventions [5, 13, 70-78]. OCT has been used as an optical biopsy method for differentiation among different tissues, e.g., healthy versus tumorous as well [6, 7]. Quantitative analysis of OCT images through extraction of optical properties has made OCT an even more powerful modality [8-10].

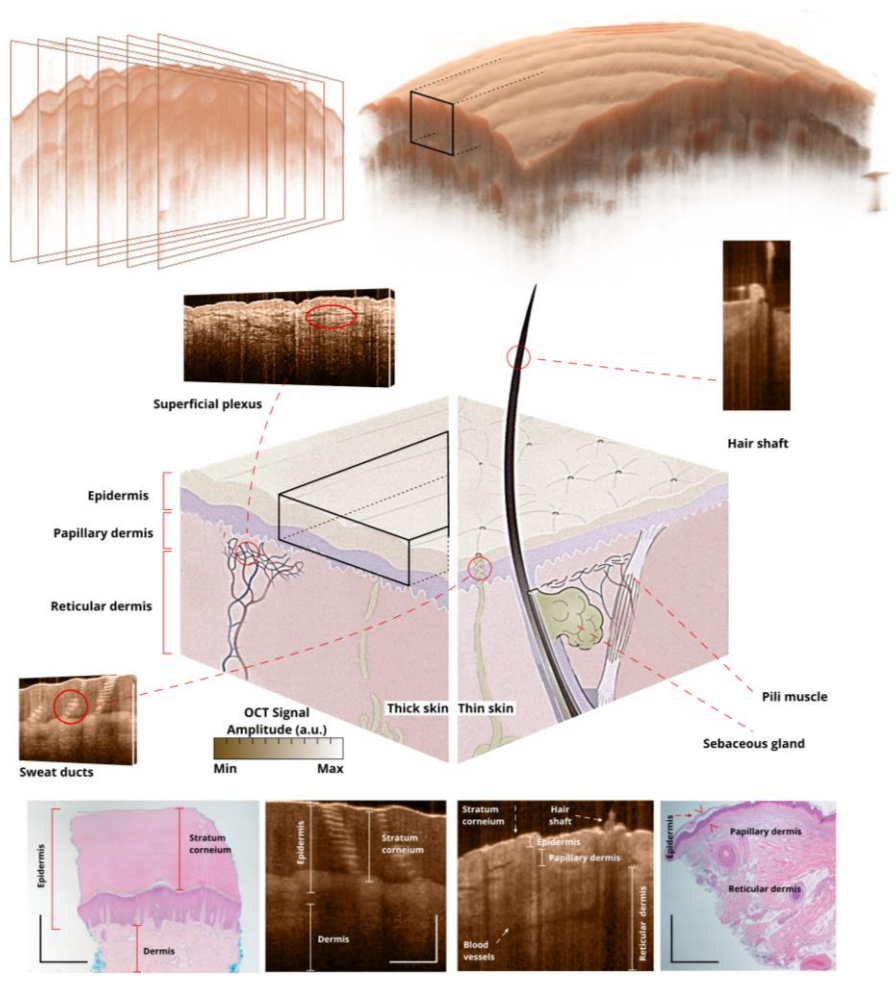


Figure 2.8 A cartoon of skin compartments, their corresponding equivalent histology and OCT images. The scale bar in OCT images is 200 μm .

The reflectivity of the skin results in a peak of the signal intensity at the surface of the skin. Stratum corneum skin layer reflects about the 5-7% of the incident light [3]. Below the entrance point of the skin surface, different layers and structures with variation in refractive index may be distinguished by the OCT. Some studies have demonstrated the ability of OCT to identify characteristics pertaining to the stratum corneum, the epidermis, the dermis, the hair follicles, the eccrine sweat ducts and sebaceous glands [69,

79-83]. The exact composition of the skin components may differ depending on the area of the body from which the skin originates.

Hence comparison between histology and OCT images can aid in characterizing skin components across different locations of the body. In addition to the signal intensity that is based on histologic information, OCT can provide a quantitative description of the tissues through optical properties, and in particular, the attenuation coefficient representing the intensity of the light beam that declines when it penetrates into a medium due to absorption and scattering. The optical properties information can be used for clinical diagnosis and characterization of skin [31, 84, 85].

In this dissertation, a comprehensive characterization of skin tissues using OCT is performed

2.7.1 Skin layer detection and Dermal-Epidermal junction localization

Knowledge about the location of the Dermal-Epidermal Junction (DEJ) plays an important role in evaluating many dermatological diseases [86, 87], for example Basal Cell Carcinoma (BCC), which is located in the deepest layer of the epidermis and invades the dermis [88-90]. Moreover, DEJ is important in the intracellular pool of bullous pemphigoid antigens, the interactions between fibronectin and keratinocytes and the epidermolysis bullosa acquisita antigen areas [91]. Therefore, knowledge of DEJ is important in determining BCC. To localize DEJ, the OCT image of skin is segmented. In healthy skin, the tissue is composed of three layers: the epidermis, dermis and hypodermis (subcutaneous tissue). The epidermis includes five main sub-layers: Stratum Corneum (SC), stratum lucidum (seen only in the skin of the sole of the feet and palmar surface of the hand), stratum granulosum, stratum spinosum, and stratum basale. Stratum basale is where the proliferation of epidermal cells occurs. DEJ locates the stratum basale which is the deepest layer of epidermis and represents the boundary between epidermis and dermis. SC is the outermost layer of the epidermis. Because of the forward back reflection from the SC, it appears as a bright layer. Because of back reflection from the SC, the hypodermis is seldom seen in OCT images [92]. Several groups have studied epidermal layer segmentation.

Neerken et al. [93] added columns of the image together to produce the average depth profile of the OCT signal and then used averaged intensity

profile to segment skin layers. Weissman et al. [94] proposed a novel shapelet-based image processing technique to detect SC and DEJ border and calculate the epidermal thickness. Hori et al. [95] used local minimum intensity to detect DEJ. Mcheik et al. used the characteristics of speckle distributions to segment the epidermis [96]. In another study, Wang et al. [97] utilized an averaged A-scan analysis to measure the mean value of the epidermal thickness. Li et. al., detected skin surface by solving a shortest path problem and using the local integral projection method [98]. Josse et. al. detected the epidermal boundaries with a three-phases algorithm: preprocessing, skin surface detection and epidermis/dermis interface detection [99]. In mentioned studies, the thickness of epidermis is measured and used as evaluation criteria for epidermis segmentation. However, the thickness of epidermis might vary based on the gender, age, body site [100]. Therefore, a standard database is essential for a correct comparison among the methods.

In this thesis, DEJ is localized with a new method to be used in skin abnormalities as well as in skin characterization where both epidermis and dermis features are investigated separately.

2.8 Summary

In order to assist specialists in their diagnostic decisions based on OCT images, image processing/analysis algorithms are used to post-process the OCT images to make the diagnostically relevant features more salient. In this chapter, the major artifacts in OCT images including speckle and image blurring are summarized. The aforementioned issues are described, along with the review of technologies and algorithms proposed in literature to solve these problems. Moreover, the dermatology application of OCT and its role in cancer diagnostic is elaborated.

Chapter 3

Intelligent speckle reduction algorithms

3.1 Introduction

Speckle pattern is highly correlated to the microstructural content (size and density) of the sample being imaged and it carries some morphological information. Since Rayleigh or Rician distributions approximate the probability density function (PDF) of the speckle [24], Artificial Neural Networks can offer an intelligent solution that reduces speckle while preserving the morphological information in the image. In this chapter an effective algorithm to reduce the speckle, based on an ensemble framework of several Multi-Layer Perceptron (MLP) neural networks is presented. The algorithm is tested on OCT images. Considerable improvements in terms of signal-to-noise ratio and contrast are demonstrated. Moreover, to address the multiplicity of the speckle reduction methods and challenges the adaptive choice of the most appropriate for a given set of OCT images, an intelligent, expandable despeckling framework is proposed. This framework decides which speckle reduction algorithm is most effective for a given image, based on either the execution time or the tissue features – morphological, textural, optical – extracted from the OCT image.

3.2 Artificial Neural Network

A Neural Network (ANN) is a processing paradigm mimicking the human biological nervous systems, i.e., brain, in information analysis. The major component of such paradigm is the structure through which the information processing is performed. This structure consists of a large number of neurons, i.e., highly interconnected processing components, that work constructively and coherently to solve specific problems. Similar to humans, ANNs learn by examples to perform a specific task such as pattern recognition or data classification. From a mathematical point of view, any ANN learns by adjusting the synaptic connections between the neurons. ANNs have the capability to analyze complex data; they can be used to derive patterns and to detect trends that are too complex to be analyzed by deterministic computer techniques. A trained ANN can be thought of as an "expert", in the given problem. This expert will then be able to predict a

solution/answer to new situations. Other advantages include, (a) adaptive learning: an ability to learn how to do tasks based on the data given for training or initial experience, (b) self-organization: an ANN can create its own organization or representation of the information it receives during learning time, (c) real time operation: ANN computations may be carried out in parallel, and special hardware devices are being designed and manufactured which take advantage of this capability, (d) fault tolerance via redundant information coding: partial destruction of a network leads to the corresponding degradation of performance. However, some network capabilities may be retained even with major network damage. Simple neuron can be thought of a device with several inputs and a single output. The neuron has usually two operational modes: the training mode and the testing mode. In the training mode, the neuron is trained to work/fire or not, for particular input patterns. In the running mode, the output is generated accordingly to the input /output list taught. However, if the input is not found in the input /output list taught, the firing rule is used to determine whether to fire or not.

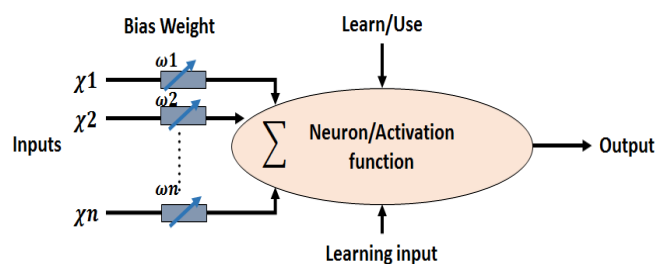


Figure 3.1 An McCulloch and Pitts neuron

With a more complex neuron, more complicated tasks can be performed that cannot be already done in computers (Figure 3.1). McCulloch and Pitts model (MCP) implements a complex neuron. In this model, the inputs are 'weighted', and each input has a decision-making power depending on the weight of the input. The weight is a constant value that is multiplied by the input. The weighted inputs are then added together and compared to a pre-set threshold value. The neuron fires only if its input overcomes the threshold.

Having neurons with weighted inputs and a threshold makes them a small sophisticated processing unit. In fact, by altering the weights and/or

thresholding the MCP neuron, the neuron has the ability to adapt itself to any problem.

Several algorithms exist that make the neuron to 'adapt', e.g., feedback networks (Figure.3.2) that are frequently used in a pattern recognition problem [101, 102].

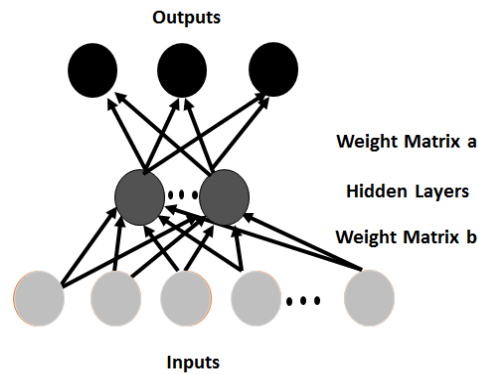


Figure 3.2 An example of a simple feed forward network

3.3 Intelligent Speckle reduction method

In the followings, the proposed speckle reduction method is presented. At first OCT speckle formulation using Rayleigh model is presented. Then the implementation of the method and the results are given.

3.3.1 OCT speckle formulation with Rayleigh statistics

Representation of the sample as a collection of point scatterers corresponds to the “random-phasor sum” mathematical formalism [103], and it has been previously applied to speckle and OCT [50, 104-106]. It explains that an OCT signal can be express as ξ and is given by equation (3.1):

$$\xi = |\xi| \exp(j\theta_s) = \sum_{i=1}^N \xi_i = \sum_{i=1}^N a_i \exp(j\varphi_i) \quad (3.1)$$

where ξ_i is the phasor of the i -th scatterer to the signal, $|\xi|$ is the speckle envelope, which formulates the basis for displaying image. If we consider that the a_i are identically disseminated with fixed mean and variance, the

φ_i are consistently distributed on $(-\pi, \pi]$, and all of the a_i and φ_i are independent [105]. Then the sum ξ is a complex Gaussian as $N \rightarrow \infty$; its real and imaginary parts are zero-mean independent Gaussian variables [23, 107] with variance σ^2 . If N is a random variable, ξ will maintain the same distribution. The envelope $|\xi|$ will be Rayleigh-distributed with parameter σ and its probability density function (PDF) will be derived by:

$$\Gamma(\xi) = \frac{\xi}{\sigma^2} \exp\left\{-\frac{\xi}{2\sigma^2}\right\} \quad (\xi > 0) \quad (3.2)$$

The intensity pattern of an OCT image is proportional to $|\xi|^2$. At any point, the signal follows an exponential distribution with standard deviation of $2\sigma^2$ and its PDF is given by equation (3.3).

$$\Gamma_{|\xi|^2}(\xi) = \frac{1}{\sigma^2} \exp\left\{-\frac{t}{2\sigma^2}\right\} \quad (3.3)$$

Finally Rayleigh distribution speckle model and is given by equation (3.4).

$$f(x_{i,j}) = \frac{x_{i,j} e^{-\frac{x_{i,j}^2}{2\sigma^2}}}{\sigma^2} \quad (3.4)$$

where $x_{i,j}$ is a pixel of the image and σ is the noise variance of the image (noise parameter). A cascade Forward ANN trained by back-propagation is then used to estimate a noise parameter for the image, followed by a numerical solution to the inverse Rayleigh distribution function [47].

3.3.2 Implementation of the proposed method

First the image is segmented into several sections. The noise parameter is then estimated by using the MLP neural networks for different segments. Using these steps and a numerical method, the segments, and consequently the image is de-noised. Further processing was performed to eliminate the blocking artifact. The algorithm essentially is composed of two phases. The first phase is the training phase. Using a Rayleigh noisy image generator in MATLAB, 10×10 pixels images are generated with sigma values (the single noise parameter employed in the Rayleigh function) ranging from 0 to 255 in steps of 0.05. For each sigma value, the procedure is repeated 100 times to generate numerous noisy images for training. Three features -

average, standard deviation, and median - are calculated from each segment and its wavelet sub-bands for training. Wavelet sub-band images we used to calculate the frequency domain statistical knowledge of the image. The neural network used is a combination of several MLP neural networks. The flow chart of the algorithm is given in Figure 3.3. Three MLP networks and a combiner, which is responsible for the averaging process, are the main components of this framework. Each of the MLP networks is composed of 15 neurons in its input layer, 10 neurons in its hidden layer and one output neuron to estimate the sigma parameter. The combiner is responsible for averaging the L neurons in the input layer, L neurons in hidden layer and one output neuron that can estimate the sigma parameter in an ensemble fashion (here, L = 3). To show the advantage of ensemble method over individual neural networks, let us consider a number of trained MLP neural networks L with outputs $y_i(\underline{x})$ (where \underline{x} is an input vector). The sigma values are estimate the using the i -th MLP neural network with an error of e_i with respect to the desired value of the sigma parameter, $h(\underline{x})$. In this situation, the following equation can be written as equation (3.5):

$$y_i(\underline{x}) = h(\underline{x}) + e_i \quad (3.5)$$

Thus, the sum of squared error for the network y_i can be calculated using (3.6):

$$E_i = \xi \left[\left(y_i(\underline{x}) - h(\underline{x}) \right)^2 \right] = \xi [e_i^2] \quad (3.6)$$

where $\xi[.]$ denotes the expectation (average or mean value). Thus, the average error for the MLP networks acting individually can be calculated by (3.7).

$$E_{AV} = \frac{1}{L} \sum_{i=1}^L E_i = \frac{1}{L} \sum_{i=1}^L \xi [e_i^2] \quad (3.7)$$

By averaging the outputs y_i , the committee prediction is obtained. This estimate will have an error equal to (8):

$$E_{COM} = (y_{COM}(\underline{x}) - h(\underline{x}))^2 = \left[\left(\frac{1}{L} \sum_{i=1}^L y_i(\underline{x}) - h(\underline{x}) \right)^2 \right] = \xi \left[\left(\frac{1}{L} \sum_{i=1}^L [e_i] \right)^2 \right] \quad (3.8)$$

Thus, using the Cauchy's inequality one can show that $E_{COM} \leq E_{AV}$ as given in equation (3.9).

$$E_{COM} = \xi \left[\left(\frac{1}{L} \sum_{i=1}^L [e_i] \right)^2 \right] \leq \frac{1}{L} \sum_{i=1}^L \xi [e_i^2] = E_{AV} \quad (3.9)$$

As shown in the despeckling flowchart in Figure 3.6, the OCT image is initially divided into several segments based on the homogeneity. Average, standard deviation and median are extracted from the image and from its wavelet components (totally of 12 inputs to the neural network). The neural network delivered the highest reliability in the estimation of the sigma value when a Daubechies 4 (db4) wavelet mother function was used for wavelet features in comparison with Haar. The transfer function, performance function, learning function, network size, and number of hidden layers, were chosen experimentally such that optimum network reliability is achieved. Such reliability is defined as the percentage ratio of the difference between the expected sigma value and the estimated sigma over the expected sigma value. The averaged reliability of the sigma estimator network measured over 20 runs was 99.3 percent that was greater than previous NN that had a reliability of 98.8 percent [50].

The second phase is the testing phase. Like in the training stage, the same pre-processing was applied to each image, and then the statistical features are extracted from each segment in the image and used as input for the neural network. The Rayleigh noise parameter was then estimated for each segment using the trained network [108]. The estimated sigma is then used along with a numerical method to solve the inverse Rayleigh function numerically for each segment. Putting together the noise model segments, one can generate a noise model image. The noise model image was deducted from the original image with a scale factor that was obtained experimentally. To remove the blocking artifact, following the method given in [109], some statistical features are extracted from the original image, based upon which of the despeckled segments are then stitched together.

3.3.3. OCT system

Figure 3.3 shows the schematic illustration of the multibeam, swept-source OCT (SS-OCT) system [17] (Vivosight, Michelson Diagnostic TM Inc., Kent, United Kingdom), used in this study. The lateral and axial resolutions

are 7.5 μm and 10 μm , respectively. The scan area of the OCT system is 6 mm width by 6 mm length by 2 mm depth. A tunable broadband laser source (Santec HSL-2000-11-MDL), with the central wavelength of 1305 \pm 15 nm successively sweeps through the optical spectrum and leads the light to four separate interferometers and forms four consecutive confocal gates [17].

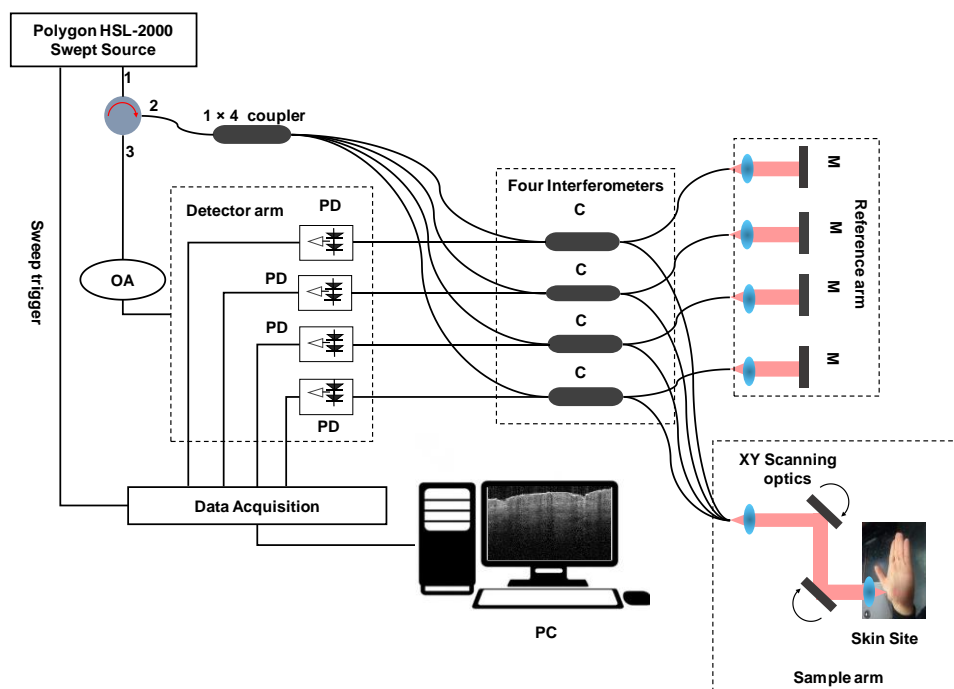


Figure 3.3 Schematic diagram of the vivo sight Michelson multi-beam swept-source OCT (SS-OCT); M: mirror, C: optical coupler, M: mirror, PD: photo detector, OA: Optical attenuator

The interference signals are received at various depths simultaneously. The 10 kHz sweep is the frequency of generating one reflectivity profile (A-Scan). Combining several adjacent A-Scans, for different transversal positions of the incident beam, a B-Scan is generated. The B-scan frame rate is 20 frame/s [110]. The interference signals are collected and analyzed by time resolved photodetectors [14, 111].

The data acquisition unit is a Spectrum M2i.4022 4-channel 20 MHz 1-bit with a hand-held scanning probe. This system is a multibeam system and

the formation of the signal and the final image procedure are given in Figure 3.4 and Figure 3.5.

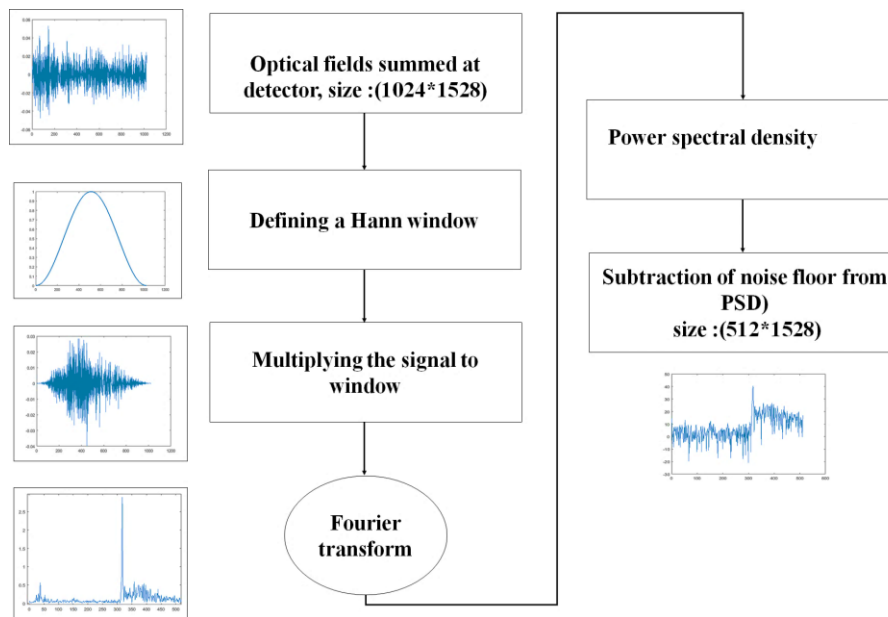


Figure 3.4 Schematic diagram of Multibeam SS-OCT A line formation for 1 channel

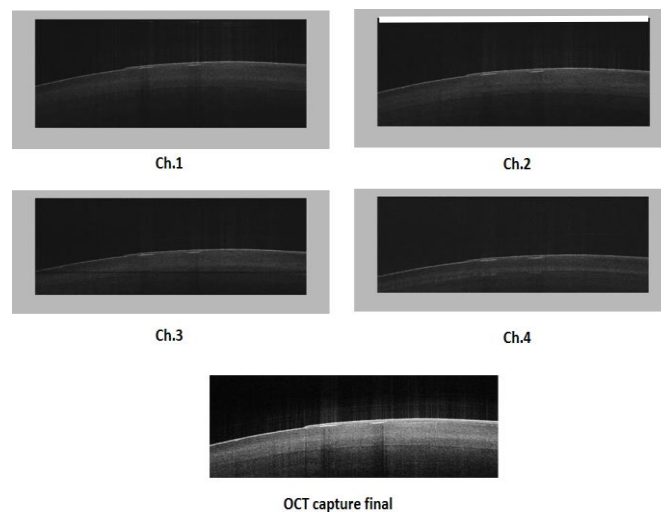


Figure 3.5 Acquired OCT images from four different channels and final blended and mosaiced OCT image, color bar is 6 mm

3.3.4 Experimental results and discussion

The number of segments in each image affects the despeckling efficiency. To improve edge sharpness and have more effective removal of the blocking artifact, images (that are all of the same dimension) are segmented into eight sub-images. The estimated sigma values for the segments within the images are given in Table 3.1 (a), (b), (c), corresponding to Figure 3.7.

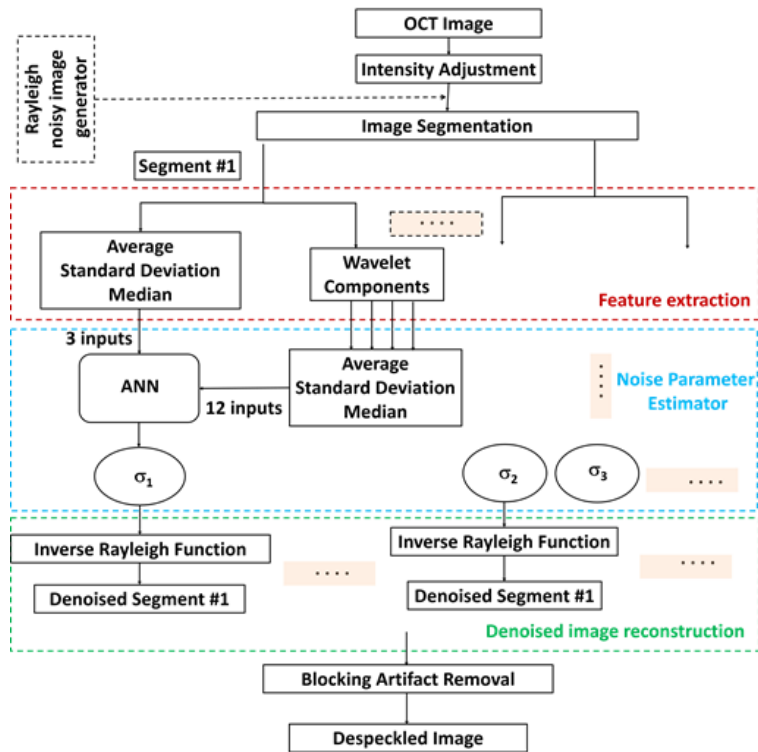


Figure 3.6 Schematic diagram of the despeckling algorithm.

Table 1. Estimated sigma values, number of segments are 8 (4 segments in each row).

Segment	Sigma for image (I1)	Sigma for image (I2)	Sigma for image (I3)
1	112	98	75
2	56	64	64
3	21	51	56
4	41	45	68
5	131	68	28
6	145	20	30
7	162	39	27
8	143	81	19

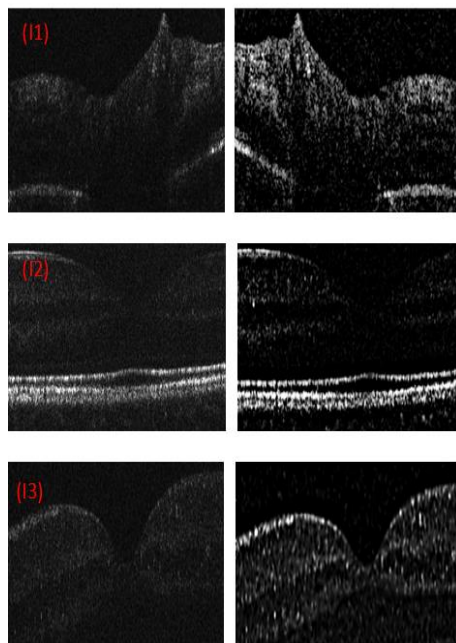


Figure 3. 7 Comparative presentation of (left): three original OCT test images (I1), (I2), (I3) and of the correspondent denoised images (right). Original OCT test images acquired from the retina (optic nerve region) of a volunteer (AP), white male, (a) Original B-scan image of optic nerve, lateral size ~ 1 -1.2 mm, the B-scan image after using the proposed method.

To evaluate the improvement of the images after despeckling, the Signal-to-Noise Ratio and the Contrast-to-Noise Ratio (CNR) are calculated as defined in equations (3. 10) and (3.11) respectively [49, 112].

$$SNR = 10 \log_{10} \left(\frac{(\max I)^2}{\sigma_b^2} \right) \quad (3.10)$$

$$CNR = \frac{1}{R} \left(\sum_{r=1}^R \frac{(\mu_r - \mu_b)^2}{\sigma_r^2 + \sigma_b^2} \right) \quad (3.11)$$

where $(\max I)^2$ represents the maximum of squared intensity pixel values in a homogeneous region of interest in the linear magnitude image, μ_b and σ_b^2 represent the mean, variance of the same background noise region, and μ_r and σ_r^2 represents the mean and variance of the R region of interest [49]. 5 regions (R=5) in the calculation of CNR are used. The results of these calculations on three test images are given in Table 3.2.

Table 3.2. Numerical assessment of the proposed denoising algorithm using SNR and CNR metrics.

	SNR		CNR	
	Original	Despeckled	Original	Despeckled
(I1)	9.2	26	2.5	4
(I2)	12.1	31	3	5.9
(I3)	11.5	24	1.9	3.2

The performance of the proposed method is compared with six despeckling methods. The quantitative assessments of the despeckled image demonstrated that the proposed method can provide an extra enhancement of around 8 dB and 0.6 in terms of SNR and CNR respectively compared to their counterparts in averaging and median filtering.

Moreover, the proposed method surpassed both Symmetric Nearest Neighborhood filter [113] and Wiener noise reduction filters by increments of around 3dB in terms of SNR. However, in case of CNR a difference of 0.2 is observed. Kuwahara [114] filtered image has a SNR=4dB and CNR of 0.1 less than the filtered image. It should be noted that this fast real-time effective algorithm could be enhanced by utilizing a more accurate estimation of sigma employing an improved version of ANN and using a more precise evaluation of the noise model. Moreover, a possible improvement can be achieved referring to image segments. A future study can be devise to cover those issues.

3.4 A Learnable Despeckling Framework

Addressing the speckle reduction methods and the challenges of selecting the most appropriate of them for a set of OCT images, in this section a Learnable Despeckling Framework (LDF) is proposed. LDF decides which speckle reduction algorithm is more effective on a given image by learning the figure of merit as a single quantitative image assessment measure. The architecture of LDF includes two main parts, i) an Autoencoder neural network, ii) a filter classifier. The Autoencoder learns the figure of merit based on the features extracted from the OCT image including SNR, CNR, Equivalent Number of Looks (ENL), Edge Preservation Index (EPI) and Mean Structural Similarity Index (MSSI). Subsequently, the filter classifier identifies the most efficient filter from the following categories: a) sliding window filters including median, mean, symmetric nearest neighborhood, b) adaptive statistical based filters including Wiener, homomorphic Lee, Kuwahara, and c) edge preserved patch or pixel correlation based filters including non-local mean, total variation, block matching 3D filtering.

3.4.1 Digital filtering method

Mathematical models used for speckle distribution depend on tissue characteristics and cellular specifications that can be represented by statistical or optical features extracted from OCT images. Three main classes of digital filters can be cited: sliding window, adaptive statistical based, and edge preserved patch or pixel correlation based. Among twenty five filters that have been explored in this work, filters from #1 to #4 are adaptive median filters with window sizes of 3, 5, 7, and 9 pixels respectively; filters from #5 to #8 are adaptive averaging filters with window sizes of 3, 5, 7, and 9 pixels respectively; filters from #9 to #12 are Symmetric Nearest Neighborhood (SNN) [113] with window sizes of 3, 5, 7, and 9 pixels respectively; filters from #13 to #14 are Kuwahara [115] with window sizes of 3 and 5 pixels; filters from #15 to #18 are adaptive Wiener filters with window sizes of 3, 5, 7, and 9 pixels respectively [35]; filters from #19 to #22 are LEE filters with window sizes of 3, 5, 7, and 9 pixels respectively; filter #23 is a pixel-wise NLM filter [116]; filter #24 is a Total Variation (TV) [113] filter; and filter #25 is a (please define the acronym) BM3D [117].

Sliding window filters: this class of filters including mean, median and SNN, is highly efficient to be used in real-time speckle reduction applications such as video-rate OCT imaging. Although these filters effectively reduce speckle noise in the OCT image, they smooth edges in the image and create blurriness. The mean filter is a linear low-pass filter. In this filter, a pixel value is replaced by the average of its neighboring pixel values. In the median filter a pixel value in a window, M by N pixels, is replaced by the value of the middle pixel in a vector of pixel values sorted in an ascending order [34]. This nonlinear filter is more robust than the mean filter, and preserves edges more effectively.

SNN is considered as an edge preserving sliding window speckle reduction method. In SNN, initially the opposite pairs of pixels in the support are compared and replaced with the pixel value that is closest to the central pixel value [113]. Each pixel value is then replaced by the average of processed pixel values in the window.

Adaptive statistical based filters: this class of despeckling filters, including Kuwahara filter [118] and homomorphic Wiener filter, uses statistical features e.g., mean and variance, extracted from the image or a part of the image. Kuwahara works by dividing the support into four sub-regions [115]. The central pixel is replaced with the average of the quadrants with the lowest variance. Wiener filter tailors itself to image local mean and local variance, i.e., the larger the variance, the less smoothing is applied [119]. LEE filter is an adaptive filter that determines each pixel value according to the weighted sum of the center pixel value based on local statistics (mean and variance) calculated in a square kernel surrounding the pixel with a minimum mean square error (MMSE) approach [120].

Patch or pixel correlation based filters: this class of despeckling filters, including NLM, TV and BM3D, are based on the high inter or intra correlations among nearby pixels or patch of pixels. In NLM method, the value of each pixel is replaced by taking a weighted average of all or some of the pixels in the image chosen on the basis of a similarity criterion. NLM filters are known to preserve the textures [116]. TV filters are based on edge preservation [44]. TV provides a close match to the ground truth image. TV efficiently suppresses the noise while preserving the image details. is a collaborative filtering method working on the locally sparse representation of the image in the transformed domain [117]. The procedure begins by

grouping similar image patches into three dimensional (3D) groups. Then a 3D linear transformation is applied on the image and then a shrinkage procedure performed. The ground truth image is then estimated by transforming the spectrum coefficients and combining the patches. Next, a Wiener filter is used to compute the optimum denoised image [121].

3.4.2 Feature extraction

To quantify the tissue properties, 63 features (different derivations of homogeneity, contrast, and regularity) [122, 123] and one optical property are extracted from OCT images. For each image, six basic statistical features including five histogram moments and the entropy are calculated from the intensity image. Twenty features are computed from the gray-level co-occurrence matrix (GLCM) [124], including five basic features in four different directions. The optical property calculated for the OCT image is the attenuation coefficient. I used Vermeer s' method to calculate the attenuation coefficient for each pixel in the OCT intensity image [125]. In order to reduce redundant features and decrease computational complexity, a subset of features is chosen using a feature selection algorithm. To decrease the computational complexity, the PCA algorithm is utilized to reduce the dimension of the features from 26 to 5.

3.4.3 Image quality assessment metrics

The performance of the filtering methods is assessed using well established objective assessment metrics, including SNR, CNR, ENL, SSIM index and EPI measures [32, 126, 127]. SNR compares the signal of an object in the OCT image to its background noise. CNR measures the activation fluctuations to the noise. The definition of SNR and CNR are given in (3.10) and (3.11), respectively [53]. ENL is a measure of smoothness in a homogeneous ROI, and can be derived by (12).

$$ENL = \frac{1}{H} \sum_h^H \mu_h^2 \sigma_h^2 \quad (12)$$

where, μ_h^2 , σ_h^2 are the mean and the variance of the homogeneous ROIs (H). The SSIM score quantifies image quality referring to its structural similarities and is based on local statistics calculations (3.13).

$$SSIM = \frac{1}{MN} \sum_{i=1}^M \sum_{j=1}^N \frac{(2\mu_{\hat{I}(i,j)}\mu_{I(i,j)} + C_1)(2\sigma_{\hat{I}(i,j)}\sigma_{I(i,j)} + C_2)}{(\mu_{\hat{I}(i,j)}^2 + \mu_{I(i,j)}^2 + C_1)(\sigma_{\hat{I}(i,j)}^2 + \sigma_{I(i,j)}^2 + C_2)} \quad (3.13)$$

where, M and N are the size of the image in transverse directions, I is the original image, and \hat{I} is the despeckled image. $\hat{I}_{(i,j)}$ and $\hat{I}_{(i,j)}$ are derived by convolving the original and despeckled images with a symmetric Gaussian kernel with window size of 11 in order to calculate their local variance and mean, i.e., $\sigma_{\hat{I}(i,j)}$, $\sigma_{I(i,j)}$, $\mu_{\hat{I}(i,j)}$ and $\mu_{I(i,j)}$. C_1 and C_2 are constant numbers which $C_1 = 6.5025$ and $C_2 = 58.5225$ [127].

EPI is a correlation-based method that shows how the edges in the image degrade and it is given in equation (3.14)

$$EPI = \frac{\sum_{i=1}^M \sum_{j=1}^N (\Delta I_{(i,j)} - \mu_{\Delta I(i,j)})(\Delta \hat{I}_{(i,j)} - \mu_{\hat{I}(i,j)})}{\sqrt{\sum_{i=1}^M \sum_{j=1}^N (\Delta I_{(i,j)} - \mu_{\Delta I(i,j)})(\Delta \hat{I}_{(i,j)} - \mu_{\hat{I}(i,j)})}} \quad (3.14)$$

where I indicates the original image, \hat{I} is the despeckled image, ΔI is an edge detected image with a Laplacian operator, μ is the mean of the image. A polarization compounding method generates the golden image. Speckle reduction can be obtained if the object alters the polarization state of the probing light enough to obtain uncorrelated speckle patterns. The light polarized along the fast and slow axis of the sample will experience a slight change in refractive index. The de-correlation can be due to local or accumulated birefringence (the change in polarization states varies with the direction of incident light) [128].

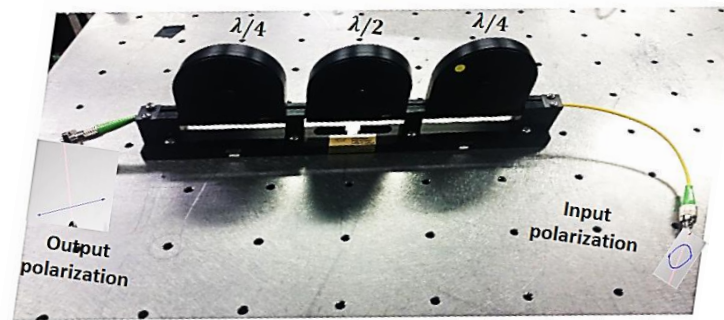


Figure 3. 8 Polarization compounding set-up main component : Manual Fiber Polarization Controller (FPC) in order to obtain denoised golden image for quality assessment measure calculations, FPC changes an arbitrary elliptical polarization to a linear polarization

The biochemical compositions of the biological tissues are polarization sensitive. A polarization controller can have the task of transforming an arbitrary polarization into another arbitrary one. Manual Fiber Polarization Controller (FPC) utilizes stress-induced birefringence to alter the polarization in single mode fiber that is looped around three independent spools to create three independent fractional wave plates (fiber retarders) [129].

To perform the polarization compounding, the FCP including the optical path three rotatable wave-plates to in cascade: a first quarter wave, which is oriented to transform the incident elliptical polarization into linear polarization, a half wave-plate, which transforms this linear polarization into another linear polarization, and a second quarter wave-plate, which transforms the other linear polarization into the desired elliptical output polarization controller [11]. Figure 3.8 shows the polarization compounding set-up component to obtain golden image.

3.4.4 Learnable despeckling framework

The architecture of the LDF includes two main parts, i) an autoencoder neural network, ii) a filter classifier. In the following, how FOM is learnt

by utilizing an autoencoder is explained. Then the training procedure of the classifier, based on FOM, to predict the more effective despeckling filter is elaborated. Prior to the training phase, according to the literature, the features are normalized one by one by subtracting the mean value and dividing by the standard deviation. A figure of merit is defined as a single representative measurement to assess the performance of each filter. In this study, the FOM is defined based on a set of five OCT quality measurements including SNR, CNR, ENL, EPI and MMSIM. The goal is to find a FOM that is the best representation of the mentioned set. Here, an autoencoder neural network with 3 layers is utilized for unsupervised learning of FOM. The structure of the autoencoder is illustrated in figure.3.9. As it is shown, in the layer 1, the inputs neurons to the network are driven by SNR, CNR, ENL, EPI, MMSIM, and a bias neuron. Layer 2 includes one neuron to estimate the FOM, and a biased neuron. Autoencoders work well if the initial weights are close to a good solution [130]. In this experiment, the initial weights are equal to 1, as in [40].

2.4.2 Filter Classifier

The FOM representatives is used to classify the filters. An Artificial Neural network (ANN) is utilised as the classifier is used. The classifier predicts the more effective filter (the winner filter) for the given input image. The designed ANN classifier includes three layers, the input layer, the hidden layer, and the output layer. The input layer includes 20 neurons corresponded to 20 features extracted from image (worth to mention that the number of extracted features is 23 initially, which is reduced to 5 by utilizing PCA feature extraction algorithm). The hidden layer includes 10 neurons. And finally, the output layer includes 26 neurons which is equal to the number of filters in the experiment. The value of each neuron in the output layer is a real number between 0 and 1 that represents the probability of the corresponding filter being the winner filter. At the end, the filter with the highest probability will be the selected as the winner. Before training, features are normalized.

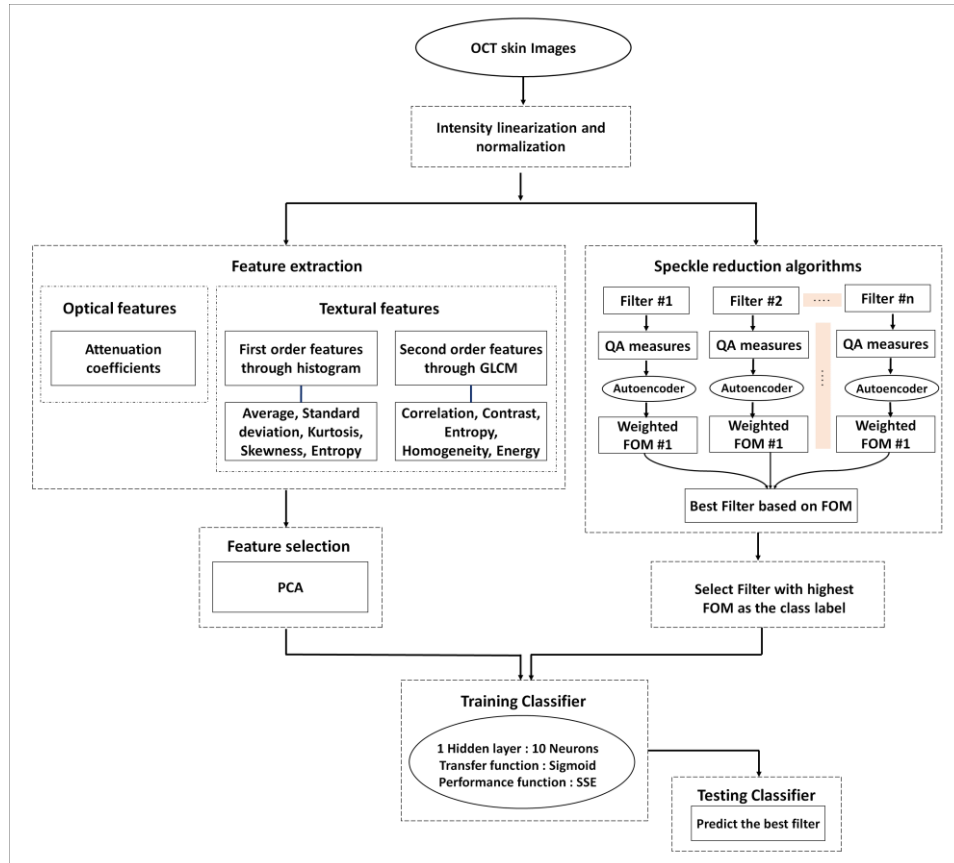


Figure 3. 9 (a) Block diagram of the LDF algorithm. OCT: optical coherence tomography, QA: quality assessment, FOM: figure of merit, ANN: artificial neural network, and GLCM: Gray Level Co-occurrence Matrix. QA measures include SNR, CNR, ENL, SSIM, and EPI.

The parameters of the ANN have been chosen according to the literature and to a trade-off between the complexity of the network and performance. The proposed framework is detailed in Figure 3. 9.

A figure of merit (FOM) inspired by the formula using the normalized weighted values (ω_i) of normalized (n) quality assessment measures given by designed neural network to assess the performance of each filter on image-set and the best filter is obtained.

3.4.5 Experimental Results and Discussions

From each image, twenty-five regions of interest are considered to compute image features and quality assessment measures. All the digital filters described here are implemented in MATLAB 8.5. The codes is implemented by a Dell desktop computer with an Intel Core i7, 3.10 GHz CPU and 8 GB of RAM. 12 healthy individuals ranged from 24 to 44 years participated in the study. OCT healthy images are acquired from individual's pre-auricular, neck, thumb pad, palm, back of hand, outer arm, inner arm, calf, back, cheek, nose, and sole that covers almost whole body skin types. Additionally, diseased cases including non-melanoma cancer, Psoriasis and Acne are imaged Based on a five-fold cross validation method, out of 285 OCT images, 80% (i.e. 228 images) are used for training the classifier and the remaining 20% (i.e. 57 images) used for testing. The histogram of winner filters in sliding window filters category, Adaptive statistical filters category, and Patch or pixel correlation filters category are illustrated in figure 3.10 figure 3.12, and figure 3.14 correspondingly [131]. Two methods to select the winner filter are used. In the first method, the winner filter is selected on the basis of a particular image attribute or a combination of some of them or the execution time. In the second method, the trained ANN determines the winner filter.

According to this graph , the Average filter with the window size 5 is the winner filter for despeckling if the overall intensity of the imaging target versus background noise is the feature in the image to be enhanced; Median filter with the window size 5 and the averaging filter with the size 9 used when image signal to nise ratio is the assessment criteria; averaging with the window size 9, and median filtering with the window size 7 chosen if

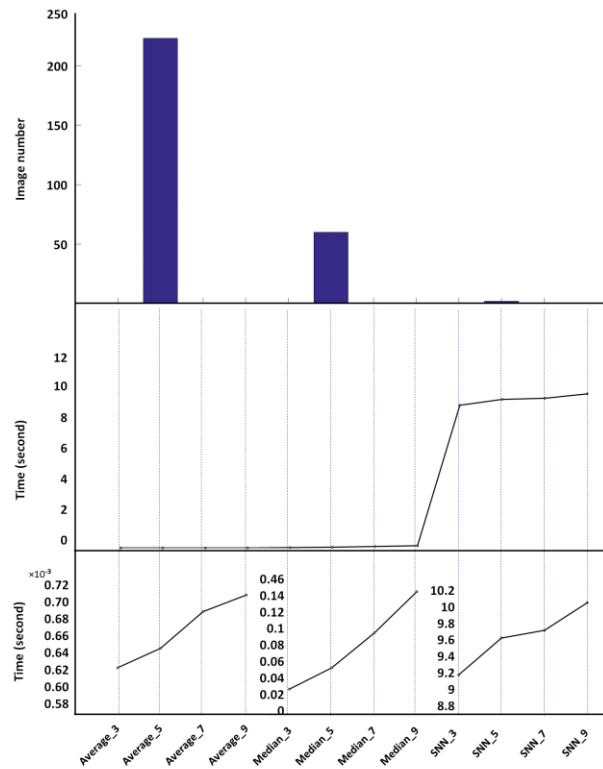


Figure 3. 10 Computed FOM for **285** filtered OCT images with their corresponding execution time. Sliding window filters are used here.

smoothness in homogeneous regions are to be enhanced; SNN with window size 7 is chosen in cases where structural similarities in the image or the quality of edges are the assessment criteria. In cases where the overall quality of the image is required, averaging, median, and SNN with window sizes 9, 7 and 7, respectively are chosen. From the execution time point of view, median filters are far less computationally expensive compared to other filters, i.e., SNN, in this category. The winner filter obtained from the classifier, in the sliding window category was the Average filter with a kernel size of 5 in most cases.

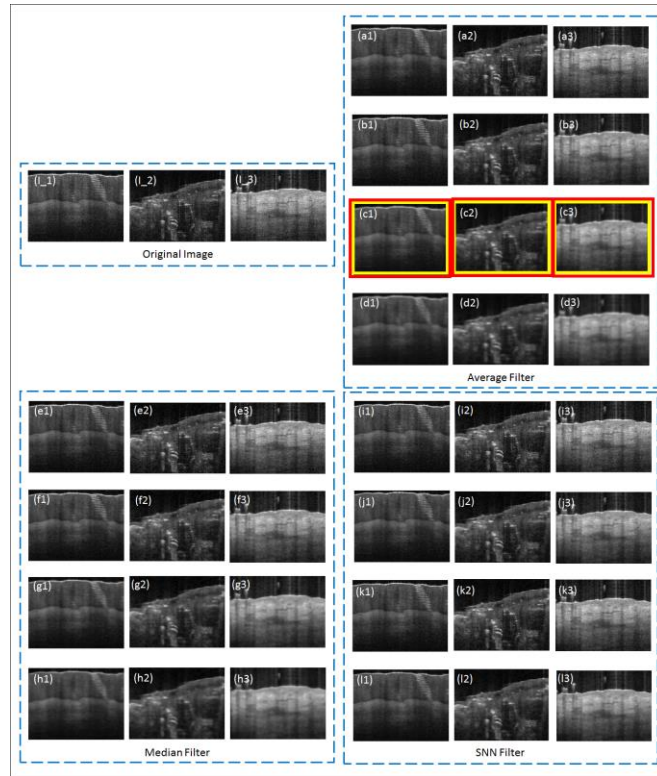


Figure 3.11 Results of despeckling using sliding window filters. Original OCT images taken from healthy thumb pad of a 24-years old male (I_1), diseased outer arm of a 56-years old female (I_2), back of a healthy 25-years old male (I_3), (a-d) Despeckled images using averaging with window sizes of 3, 5, 7, and 9, respectively, (e-h) despeckled images using median filtering with window sizes of 3, 5, 7, and 9, respectively, (i-l) despeckled images using SNN filters with window sizes of 3, 5, 7, and 9, respectively. The yellow boxes indicate winner filters based on the FOM measure and the red box indicates the winner filter chosen by classifier.

In figure.11, three original OCT images and despeckled ones using sliding window filters, are shown. The yellow boxes in the figure, indicate most-selected winner filters based on FOM criterion, i.e., median filter with window size of 9. The red box indicates the chosen filter by classifier. Figure 3.12 shows the histogram of winner filters in adaptive statistical filters category as well as their execution time. According to this graph, in almost all cases Lee filter with window size 5 is the winner filter for despeckling even when FOM is the quality assessment criterion.

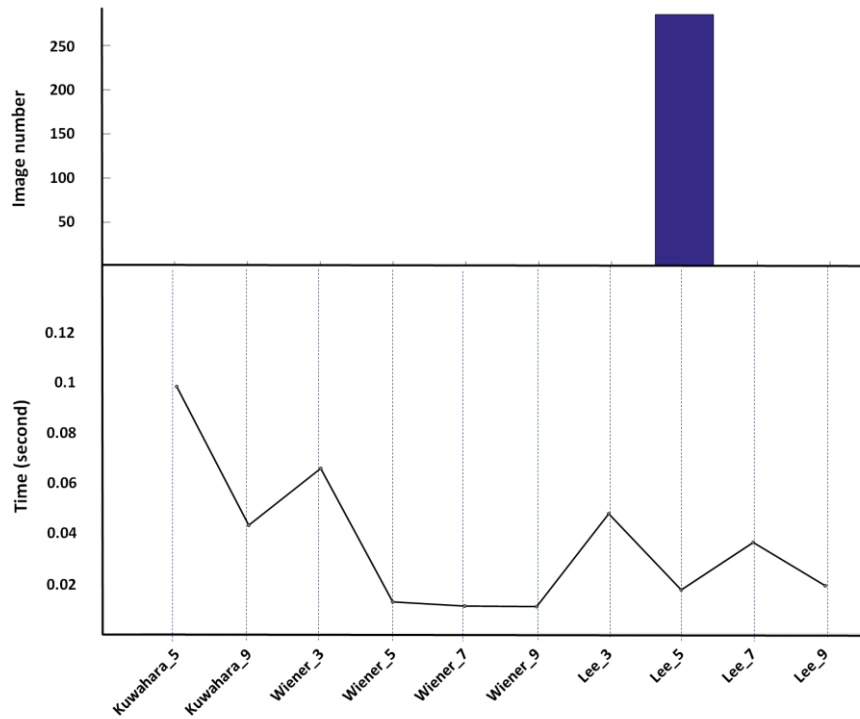


Figure 3.12 Quality assessment measures calculated for 285 filtered OCT images with their corresponding execution time. Adaptive statistical filters are used here.

In figure 3.12, original OCT images and despeckled ones using adaptive statistical filters, are shown. The yellow boxes in the figure, indicate most-selected winner filters based on FOM criterion, i.e., Kawahara with the window size of 9, wiener filter with the window size of 3, Lee filter with window sizes of 7, and 9. The red box indicates the chosen filter by classifier.

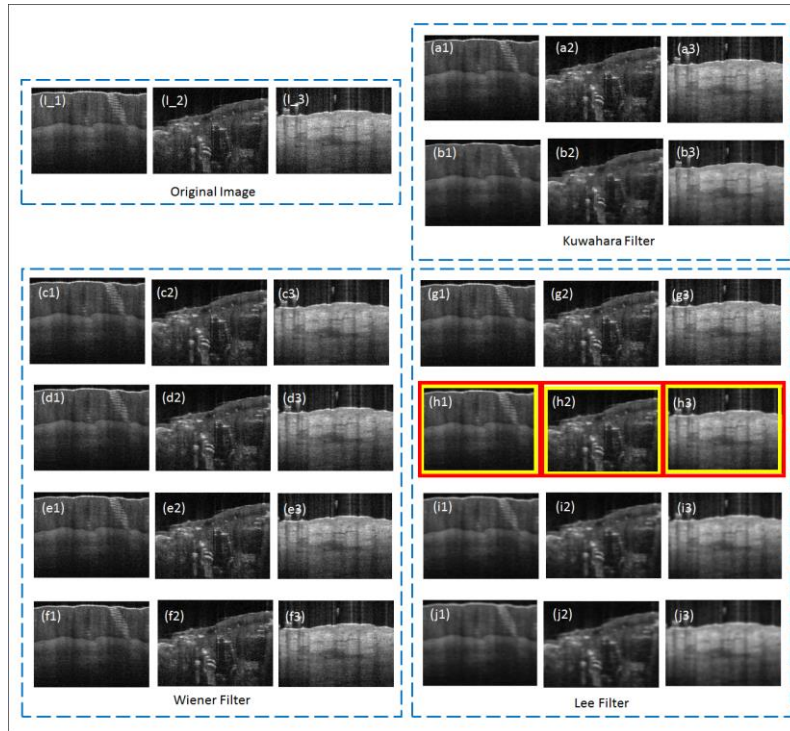


Figure 3.13 Results of despeckling using adaptive statistical filters on OCT images used in Figure 5. (a-b) Despeckled images using Kuwahara filter with window sizes of 5, and 9, respectively, (c-f) despeckled images using Wiener filter with window sizes of 3, 5, 7, and 9, respectively, (i-l) despeckled images using Lee filters with window sizes of 3, 5, 7, and 9, respectively. The yellow boxes indicate winner filters based on the FOM measure and the red box indicates the winner filter chosen by classifier.

Figure 3.14, shows the histogram of winner filters in patch or pixel correlation filters category as well as their execution time. According to this graph, in many cases BM3D filter, and in some cases TV is the winner filter for despeckling. When FOM is the quality assessment criterion, BM3D and TV are almost equality chosen. Classifier chose BM3D and TV most times.

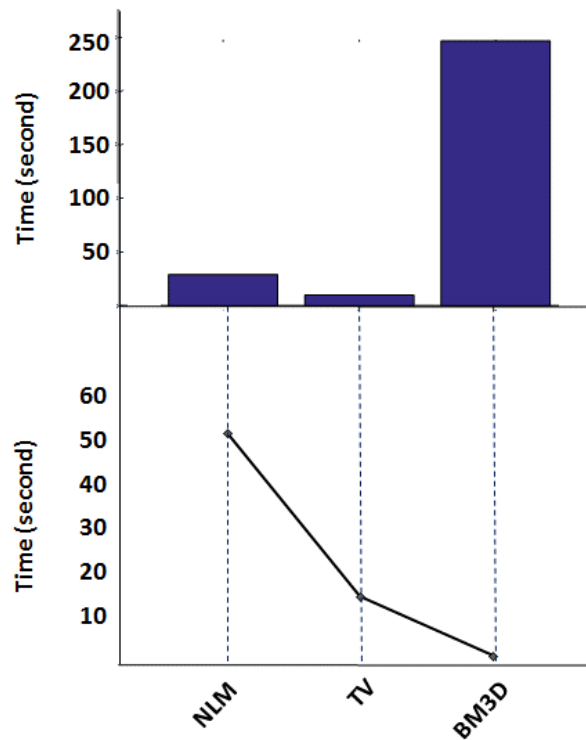


Figure 3. 14 Quality assessment measures calculated for 285 filtered OCT images with their corresponding execution time. Patch or pixel correlation filters are used here.

In figure 3.15, original OCT images and despeckled ones using patch or pixel correlation filters, are shown. The yellow boxes in the figure, indicate the winner filters selected based on FOM criterion, i.e., BM3D and TV. The red box indicates the chosen filter by classifier.

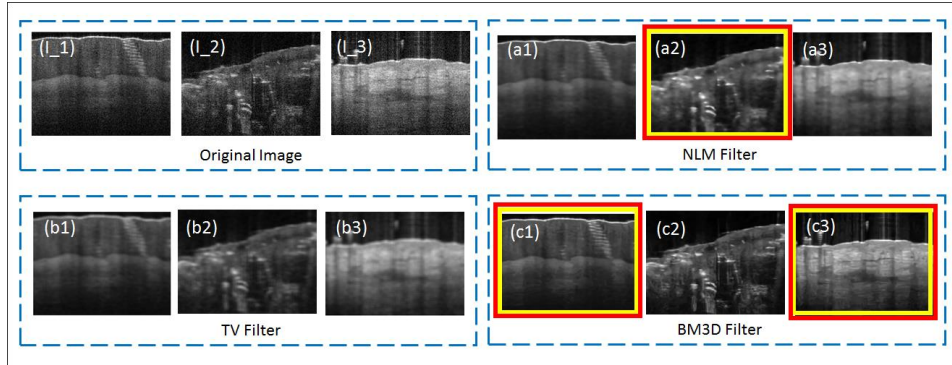


Figure 3.15 Results of despeckling using adaptive statistical filters on OCT images used in Figure 5. (a) Despeckled images using BM3D filter, (b) despeckled images using NLM filter, (b) despeckled images using TV filter. The yellow boxes indicate winner filters based on the FOM measure and the red box indicates the winner filter chosen by classifier.

Finally, we evaluated the performance of filters from all three categories. BM3D filter was the winner filter for most images considering individual quality assessment criterion, i.e., SNR, CNR, ENL, MSSIM, EPI, or even

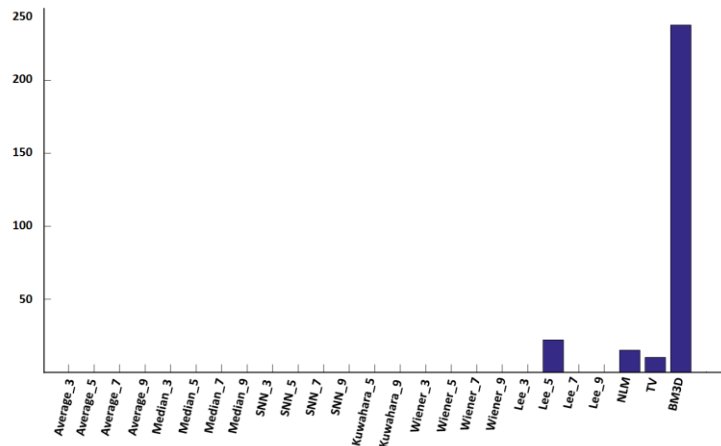


Figure 3.16 Quality assessment measures calculated for 285 filtered OCT images. All filters in three categories are used here.

FOM (see figure 3.16). Lee filter with kernel size 5 was selected from adaptive filter category for some images and the rest of winners are from 3rd

category. The winner filter obtained from the classifier selected from the 3rd category and in most images which are TV and BM3D. Figure 3.16 shows normalized FOM for all the 25 filters.

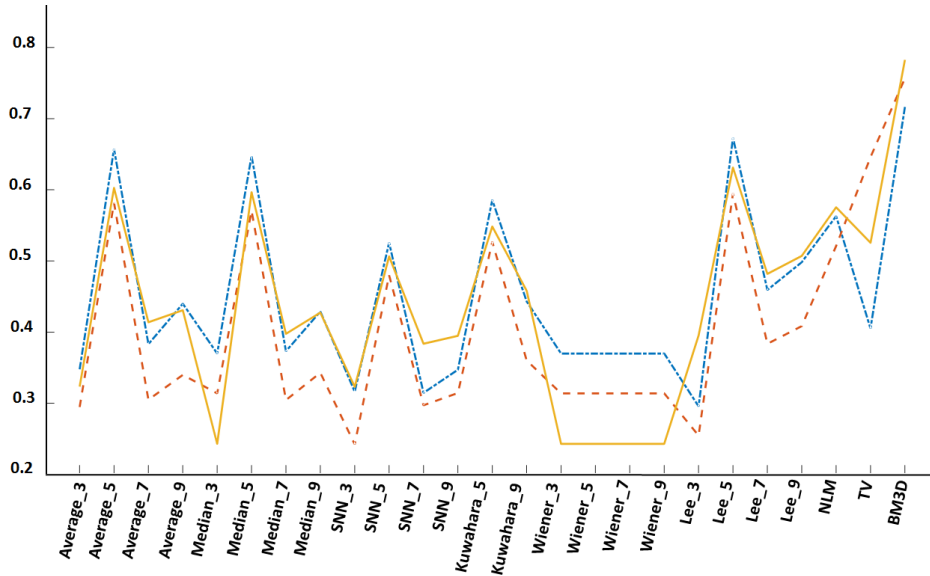


Figure 3. 17 Quality assessment measures calculated for 285 filtered OCT images. All filters in three categories are used here.

Figure 3.17 shows the comparison of all different filters' QA measures for three selected image showed in figure 3.15. Referring to the execution time, it is observed that even though the third category filters, most efficiently filtered images, their execution time is in the order of tens of seconds, while the execution time of first and second category filters are in millisecond range. Hence, the third category filters may not be suitable for real-time applications.

3.5 Conclusions and outlook

Substantially improvement of the quality of OCT images through speckle reduction methods draw a great deal of interest. In this chapter, among the software based method a speckle reduction algorithm is presented based on the approximation that speckle noise has a Rayleigh distribution with a noise parameter, sigma. In this study, neural network used to estimate the

noise parameter, sigma, for despeckling optical coherence tomography images of retina. The intelligence inherited in the method allows improving the image quality while preserving the edges. The sigma estimator kernel worked with more than 99.3% reliability on average. The proposed algorithm is also compared with some other bilateral digital filters and demonstrated a satisfying evaluation. In second section, an intelligent framework is introduced to select the best required speckle reduction algorithm for a certain image set of skin. Different despeckling methods are developed to mitigate the speckle phenomenon effect in OCT images both using software based and hardware based speckle reduction techniques. A comparative study of some of these speckle reduction methods for OCT images are given in [15]. However still there is room to expansively compare existing software-based despeckling methods. To address the challenge of finding an optimum speckle reduction filter for an image or set of image, a learnable despeckling framework, named LDF is proposed. LDF predicts which speckle reduction algorithm is more effective for a given image, based on tissue morphological, textural and optical features extracted from the image.

BM3D filter outperformed in most cases. Even though, the most time efficient filters are from the simpler algorithms, i.e. first and second categories. It should be noted that although FOM can decide about optimum filter, while the classifier predicts the efficient filter based on the textural features of images. To conclude an intelligent framework is introduced to select the best required speckle reduction algorithm for skin OCT images. This framework can be expanded to include any other despeckling filters by training the network based on results from the new filter. This framework can be expanded to use any other filters to despeckle an image. It only would need to train again with new filters

Chapter 4

A Cluster based Wiener Filtering method for OCT images

4.1 Introduction

In this chapter an optimized method for speckle reduction of OCT skin images is presented. Considering the architectural structure of skin layers, OCT skin images can be segmented into differentiable clusters. The image in each cluster is then filtered by a Wiener filter. The proposed method was tested on an optical solid phantom with predetermined optical properties and on healthy human skin images. The results show that the proposed cluster-based filtering method can effectively reduce the speckle and increase the signal-to-noise ratio and the contrast while preserving the edges in the image. To the best of my knowledge, most of the implemented methods have not considered the inherent characteristics of the tissue in the process of speckle noise reduction. Based on this information, the techniques known to date can be utilized as a general speckle removal method for images acquired by any low coherent imaging modality.

The structure of the chapter is as follows. Section 2 contains the methodology of the proposed algorithm including the pseudo-code of CWF and its detailed explanation. The results and the discussion about the obtained results are presented in sections 3 and 4. Finally, in section 5, the conclusion and some suggestions for future work are given.

4.2 Adaptive Wiener filtering

The Wiener filter minimizes the mean square error between an estimated random process and a desired process. It estimates the local mean and variance of a sliding window of size n pixel by m pixel, around each pixel located in the i^{th} row and j^{th} column of the image, and generates a new estimated pixel value of $\hat{I}_{(i,j)}$ [132]. The new $\hat{I}_{(i,j)}$ is calculated in (4.1).

$$\hat{I}_{(i,j)} = \mu + \frac{\sigma^2 - v^2}{\sigma^2} (I_{(i,j)} - \mu) \quad (4.1)$$

where μ is the mean, σ^2 is the variance and v^2 is the local variance of the sliding window of n by m pixels surrounding the pixel (i, j) . v^2 is calculated as (4.2)

$$v^2 = \frac{1}{mn} \left[\frac{I^2 * O_{mn}}{mn} - \left(\frac{I * O_{mn}}{mn} \right)^2 \right] \quad (4.2)$$

where O is a matrix of ones with the same dimension as the sliding window, i.e. n by m pixels and $*$ indicating a convolution operator.

4.3 Cluster-based Wiener Filtering (CWF)

The *CWF* algorithm begins with a hierarchical agglomerative clustering on each image. This type of clustering is considered as a bottom up approach where each observation starts to create its own cluster, then pairs of clusters are merged sequentially to form one single cluster. In order to decide which cluster pairs should be combined, a measure of unlikeness between sets of observations is required [133]. The measure that is used here is the Euclidean distance. The considered linkage criterion is a Ward's minimum variance method, where the objective function is the sum of squares' error [134]. The pseudo code of our *CWF* is given in Algorithm. 4.1.

The features that is used in the clustering technique are the intensity OCT image and the map of attenuation coefficient. Attenuation coefficients are obtained by fitting a model to the OCT signal from a region of interest (ROI). Due to the scattering and absorbing structures, light is attenuated when travels within a tissue [135]. Beer-Lambert law, which is governed by exponential decay, can help explain this attenuation using the single-scattering model of the skin. Measuring attenuation coefficient from OCT images has been used in characterization of the tissue [125, 136-138], which can consequently provide information about structural changes in the tissue. Recently, Vermeer et.al [125] developed a simple method to estimate the attenuation coefficients locally where every pixel in the OCT data set is converted into a corresponding Optical Absorption Coefficient (OAC) pixel. This produces accurate results for both homogeneous and heterogeneous tissue and does not require pre-segmenting or pre-averaging of data. The attenuation coefficient analysis method was evaluated as a diagnostic tool. The single scatter equation is determined as: $I(x) = I_0 \rho e^{-2\mu z}$, where I represent the value of the detected intensity, I_0 is the

intensity of incident light, ρ is the backreflection coefficient, μ is the attenuation coefficient, and z is the depth that the light is travelling through the tissue. Therefore, z is the depth of penetration and can be written as a function of pixel x co-ordinate, i.e. $z \propto i$. Factor of 2 comes from the fact that light travels round-trip within the tissue. The common way to calculate an attenuation coefficient is by fitting an exponential curve to the above equation (4.3), upon which the decay constant can be extracted. The resulted values are then averaged, smoothed, and fitted into a polynomial equation. The slope of the equation thus yields an attenuation coefficient of the region.

An explanation on the *CWF* algorithm is given in the following.

Initialization: In this step, a variable set is defined that is required to perform the *CWF* filtering method on the OCT image. The OCT image is a 2-dimensional matrix of size $R \times C$ that is given in terms of OCT signal intensity (I). Here, the desired number of clusters is set to $K = 4$. It should be mentioned that the hierarchical clustering method calculates all possible clustering results with different values of K . Here, the desired number of clusters is set to $K = 4$ (phantom with 4 layers have been designed, and consequently K is set be equal to 4 for phantom images). Similarly, as the skin images have 4 main layers (stratum corneum, epidermis, dermis, and hypodermis), in skin images, it is considered that K to be equal to 4 as well, and the size of neighborhood window is set to $N1 \times N2 = 5 \times 5$. The size of neighborhood window is set to $N1 \times N2 = 5 \times 5$. The size of window over which the algorithm estimates the local mean and variance is important, as the size needs to be at least 5×5 for a reasonable variance estimation, while it needs to be small enough to insure local signal stationarity following the analogy that is given in [40] and [139].

Calculating optical properties: The attenuation coefficient (μ_a) of each pixel is calculate at the position $[i, j]$ by using (4.3).

Hierarchical Clustering: A feature vector including the intensity value (I) and the corresponding attenuation coefficient (μ_a) of each pixel is assign at the position $[i, j]$ (4.4). Thereafter, the ‘Ward linkage hierarchical clustering’ technique is applied on the feature vector to generate a cluster set (4.5). The result of the clustering is a matrix CL of $R \times C$ size where each element at the position of $[i, j]$ in the matrix CL indicates the cluster number that the corresponding pixel belongs to. The elements of the matrix CL are discrete values in the range $[1, K]$, where K is the maximum number of clusters [140].

Filtering: After grouping the pixels into different clusters, each cluster is filtered using appropriate adaptive Wiener filter.

Algorithm 4.1: Cluster-based Wiener Filter (*CWF*)

Initialization

$I[i, j]$ intensity of a pixel at the row of i and the column of j in the OCT image

μ_a attenuation coefficient

Δ pixel size

R number of pixels in each row of the OCT image

C number of pixels in each column of the OCT image

N total number of pixels ($R \times C$)

F feature vector including $\{I, \mu_a\}$

CL clustering matrix

K desired number of clusters

$N1 \times N2$ size of neighborhood window

$N2$

1. Calculating optical properties

1.1. For each pixel at the position $[i, j]$, calculate [125]:

$$I[i] \propto e^{-2\mu_a z} \quad (4.3)$$

2. Applying Hierarchical Clustering

2.1. For each pixel at the position $[i, j]$, assign the feature vector of

$F[i, j]$:

$$F[i, j] = \{I[i, j], \mu_a[i, j]\} \quad (4.4)$$

2.2. Apply Ward linkage hierarchical clustering on all pixels with feature set of F

$$CL = \text{Hierarchical_Linkage}('Ward', F, K) \quad (4.5)$$

2.3. Apply max neighborhood filter on the clustering matrix CL in a window size $\eta = N1 \times N2$ around each pixel

$$CL = \text{Max_filter}(CL, \eta) \quad (4.6)$$

3. Applying Filtering

3.1. For each pixel at the position $[i, j]$ which belongs to the cluster $\#k$, calculate mean and variance in a window size $\eta = N1 \times N2$

$$\text{mean}_k[i, j] = \frac{1}{\#p} \sum_{l, m \in \eta \text{ \& pixel } [l, m] \text{ belongs to cluster } k} I[l, m] \quad (4.7)$$

$$v_k^2[i, j] = \frac{1}{\#p} \sum_{l, m \in \eta \text{ \& pixel } [l, m] \text{ belongs to cluster } k} (I^2[l, m] - \text{mean}_k^2[i, j]) \quad (4.8)$$

Where p is the normalization constant, which is equal to the number of pixels that belongs to the cluster $\#k$ in the window size η .

3.2. For each cluster $\#k$, calculate the noise variance within the cluster

$$\sigma_k^2 = \frac{1}{\#q} \sum_{\text{pixel } [l, m] \text{ belongs to cluster } k} v_k^2[l, m] \quad (4.9)$$

Where q is the normalization constant, which is equal to the number of pixels that belongs to the cluster $\#k$.

3.3. For each pixel at the position $[i, j]$ which belongs to the cluster $\#k$, update the intensity values

$$I'[i, j] = \text{mean}_k[i, j] + \frac{\sigma_k^2[i, j] - v_k^2}{\sigma_k^2[i, j]} (I[i, j] - \text{mean}_k[i, j]) \quad (4.10)$$

4.4 Optical phantom design

In order to evaluate the proposed *CWF* method, a manually segmented multilayer phantom with different optical properties has been designed [141]. The phantom is a virtual tissue with predefined optical properties, e.g., attenuation coefficient, scattering coefficient, and anisotropy factor. The phantom's different layers can be distinguished and labeled manually, in order to be utilized later in the evaluation of the clustering algorithm. To mimic the structure of skin, each phantom has multiple layers with different optical properties. To make the solid phantom, TiO_2 (Titanium Dioxide) is dissolved in polyurethane (WC-781, BJB Enterprise Co., US) [142]. Different concentration of TiO_2 is utilized to achieve various optical properties. TiO_2 is dissolved into two components of polyurethane at the ratio of 100 to 85 according to the datasheet. The additives are added by 5 min vortex, followed with a 15 min ultrasound bath at the room temperature. Phantom is solidified overnight.

The cubic phantom has the size of $2\text{ cm} \times 2\text{ cm} \times 1.5\text{ mm}$. In order to design each layer with the same thickness, the first and fourth layer is set to be 0.375 mm , where the second layer is 0.75 mm . For the third layer, a drop of $10\text{ }\mu\text{l}$ of material is added. The phantom is casted from bottom to the top by adding $150\text{ }\mu\text{l}$ of material on the fourth layer, $10\text{ }\mu\text{l}$ of material on the third layer, $280\text{ }\mu\text{l}$ of material on the second layer, and finally $75\text{ }\mu\text{l}$ for the first layer left (1L) and first layer right (1R), respectively. The schematic illustration of the phantom and the top view of the phantom are given in figure (4.1a) and figure (4.1b), respectively.

The Mie scattering coefficient is used to determine the reduced scattering coefficient (μ'_s) of the phantom layers [143]. μ'_s is calculated based on the concentration of TiO_2 sphere (C_{TiO_2}) in polyurethane, which is the sphere numbers per volume of polyurethane. In order to calculate the C_{TiO_2} , the volume of one sphere of TiO_2 ($V_{TiO_2}^s$), and the volume of TiO_2 (V_{TiO_2}) are calculated in equations (4.11) and (4.12), respectively:

$$V_{TiO_2}^s = \frac{4}{3} \pi r^3 = 1.77 \times 10 \mu m^3 \quad (4.11)$$

$$V_{TiO_2} = \frac{m}{\rho} = \frac{m}{4.23} cm^3 \quad (4.12)$$

where r is the radius of one TiO_2 sphere (diameter of TiO_2 is $0.15 \mu m$); m is the total mass of TiO_2 in polyurethane; ρ is the density of TiO_2 , which is $4.23 g/cm^3$. Hence, the number of TiO_2 spheres (N_{TiO_2}) is obtained by equation (4.13) as:

$$N_{TiO_2} = \frac{V_{TiO_2}^s}{V_{TiO_2}} \quad (4.13)$$

Thus, the concentration of TiO_2 (C_{TiO_2}), is as (4.14):

$$C_{TiO_2} = \frac{N_{TiO_2}}{V} \quad (4.14)$$

where V is the volume of polyurethane. Then C_{TiO_2} is plugged into the online Mie scattering calculator [144], where the scattering coefficient is obtained, μ_s . Finally, the reduced scattering coefficient, μ'_s , can be derived from μ_s , by using (4.15):

$$\mu'_s = \mu_s (1 - g) \quad (4.15)$$

where the value of g is given as 0.715 [145, 146]. Table 4.1 summarizes the reduced scattering coefficients of different layers of the phantom.

Table 4.1 Reduced scattering coefficient (μ'_s) of different layers of the phantom (w/v = weight/volume, $\lambda = 1300 nm$)

Phantom A					
	1L	1R	2	3	4
$TiO_2\%$ (w/v)	0.65%	0.52%	0.26%	0.91%	0.65%
$\mu'_s (cm^{-1})$	1.36	1.08	0.55	1.90	1.36

4.5 Results

In this section, the proposed *CWF* technique is evaluated. The organization of this section is as follows. First, the proposed clustering method is performed on the phantom to evaluate the clustering results. Then, the proposed filtering method is applied on *in-vivo* images of human skin, and assess the results qualitatively and quantitatively.

4.5.1 Evaluation of clustering method on phantom images

To evaluate the clustering method, the phantoms described in subsection 4.5. have been imaged by using OCT system. To evaluate the performance of the clustering method, a phantom with pre-defined optical properties is used.

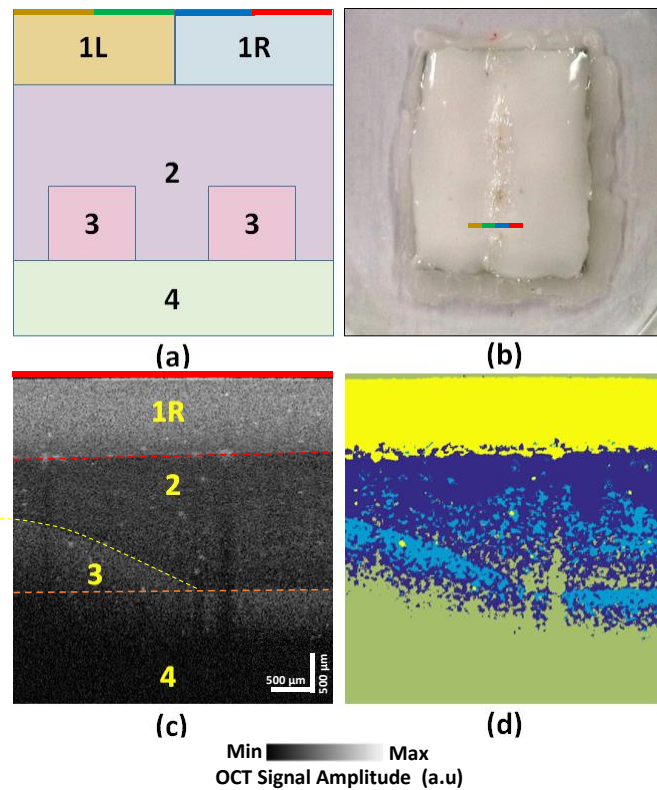


Figure 4. 1 Evaluation of clustering on OCT images of phantom. (a) Schematic illustration of a multilayer phantom, the cross-section view, (b) top view where the location of B-scan illustrated with a 4 colors line, brown, green, blue and red,

which is corresponded to the 4 colors in the cross-section view, (c) OCT B-scan image of the right side of the phantom and manual segmentation, (d) the corresponding clustered image of the OCT image.

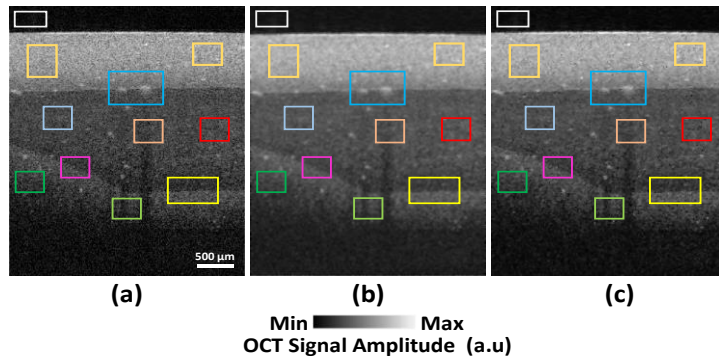


Figure 4. 2 (a) OCT phantom image, (b) Wiener filtered phantom image, and (c) *CWF* filtered phantom image. The ROIs for calculating quality assessment measures are depicted by colored rectangles. Homogeneous regions are used for SNR

The extracted values show the correctness of the clustering method to differentiate layers with similar properties. The method is extendible to complex tissues. The OCT images of the phantom present four distinguishable layers of phantom as it is given in Figure 4.1 (a, b).

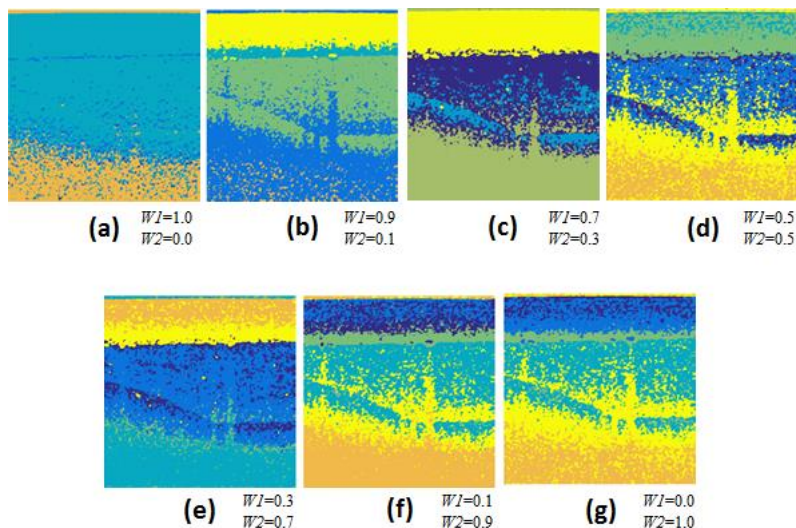


Figure 4. 3 Phantom clustering result using different combinations of features' weights, where $w1$ and $w2$ represent the weights of attenuation and intensity features, respectively.

The OCT images of the phantom includes four distinguishable designed layers is given in figure (4.1.a-b). The labels related to each different layers of phantom are illustrated in figure. (4.1.c).

The evaluation of clustering algorithm depicting identical regions with OCT image is given in figure (4.1.d), the identical regions present by color coded map of corresponding clusters. i.e. the layer 1R corresponds to the yellow cluster, the layers 2, 3 and 4 correspond to the dark blue, light blue and green clusters. The extracted values show the correctness of the clustering method to differentiate layers with similar properties which is extendible to the scenario when there is complex tissues. The result of filtered phantom images using Wiener filter and *CWF* filter is given in figure (4.2.b) and (4.2.c), respectively.

The clustering result have also been evaluated on the designed phantom using different set of weights. The results are illustrated in Figure 4.3, where $w1$ and $w2$ represent the weights of attenuation coefficient and intensity features, respectively. One can claim that when the optimum weights are used in the algorithm, the effect of shadowing due to slight impurities in the phantom is reduced dramatically. As it is illustrated, the desired result was obtained using $\{w1 = 0.7, w2 = 0.3\}$ for the attenuation coefficient and intensity features, respectively.

However, it is worthy to consider that due to the inhomogeneity of the TiO_2 particles, clustering does not differentiate the layers perfectly. In addition, clustering categorizes the areas with similar speckle properties, rather than segmenting the regions from their borders.

4.5.2 Application of CWF on skin images

OCT images are acquired from 8 healthy volunteers, 25 to 35 years old male's palm of hand and thumb.

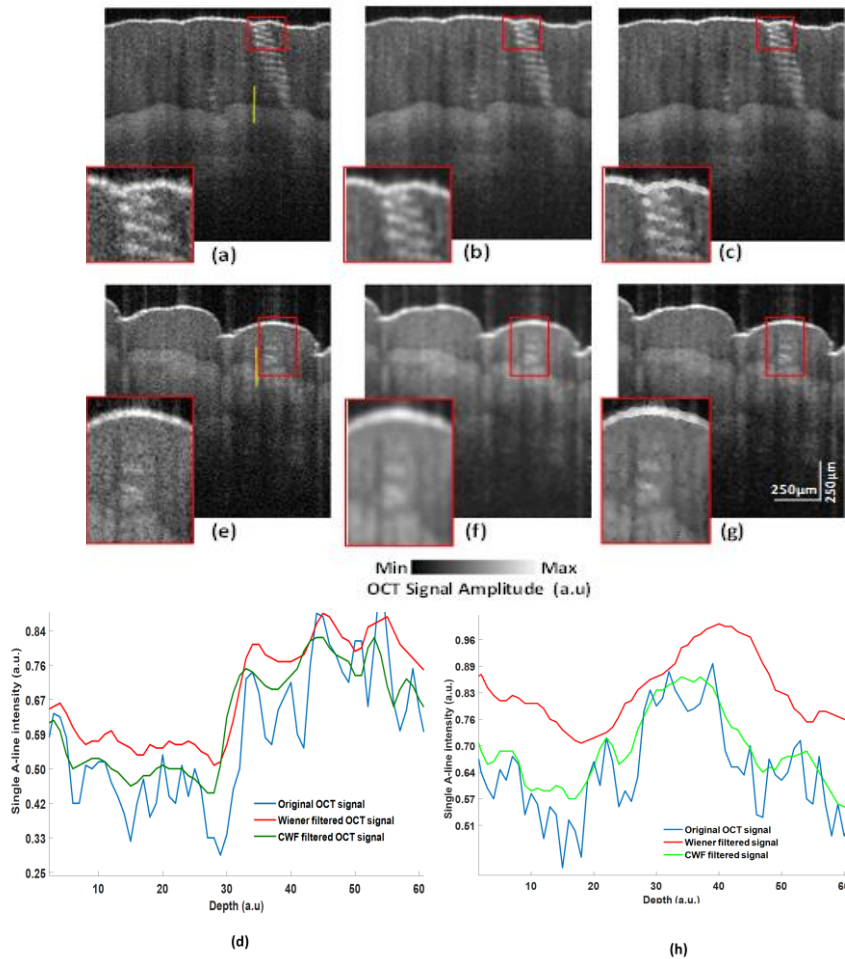


Figure 4. 4 OCT image de-speckling. (a, e) Original OCT images, (b, f) Wiener filtered OCT images, (c, g) filtered OCT images using the proposed method, (d, h) comparison of A-lines #200 profile of the original image, Wiener and the proposed filtered images. Vertical yellow line corresponds to A-Line #200.

The proposed de-speckling method was applied on 170 B-scans of 8 individuals (1360 B-scans). The results obtained from *CWF* were compared with those of conventional Wiener filtering [147] both quantitatively and qualitatively (see Figure 4.4). In Figure 4.4, the SNR, and CNR of de-speckled images using Wiener filtering are improved by 10.4 dB, and 8.45, respectively. The improvement using the proposed method was however significantly better, which are 11.95 dB, and 10.38, respectively. The EPI

was preserved better, 1.5 times, with the proposed method compared to Wiener filtering.

The quantitative results for 8 OCT skin images are listed in Figure 4.5. In comparison with conventional Wiener, the *CWF* is more effective in terms of CNR. The SNR of the filtered images by Wiener filter is slightly higher than those of the proposed method in some cases. The proposed filter has shown to preserve the edges better than conventional Wiener. The relations between the optical properties in the tissue and the performance of the proposed algorithm allow using the *CWF* algorithm more effectively.

The reduced scattering coefficient (μ'_s) of different layers of the phantom, and the corresponding SNR and CNR of the filtered phantom image are listed in Table 2. The *CWF* algorithm performs better in the layers with lower reduced scattering coefficient (μ'_s).

In comparison to Wavelet filtering, the *CWF* improvement of SNR, CNR, EPI, and SSIM are 2.4 (dB), 3.1, 1, and 0.08 respectively, for a given image

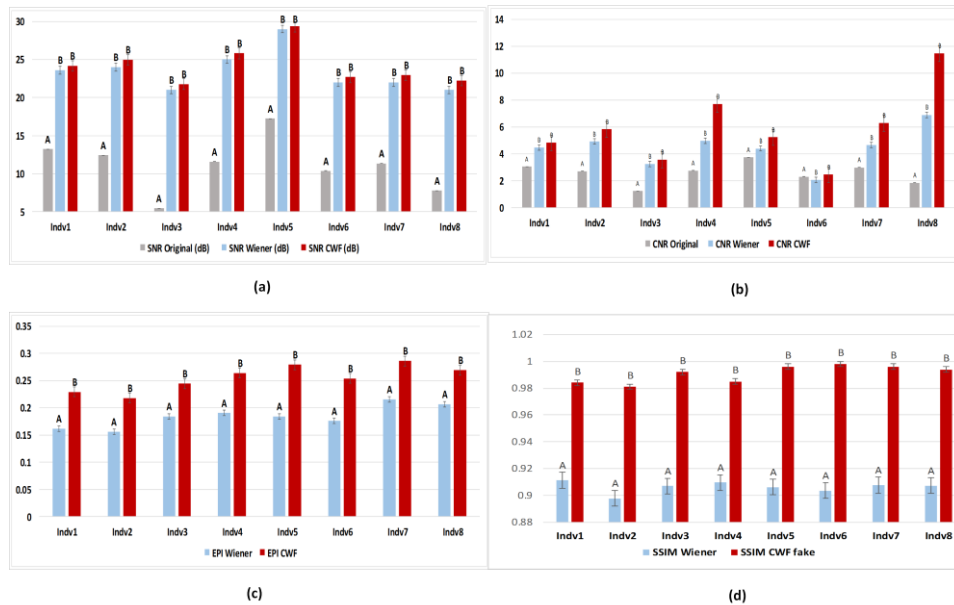


Figure 4. 5 Comparison of SNR, CNR, EPI, and SSIM of the original with Wiener filtered, and the proposed de-speckled images. . Bars represent standard deviation. Means with different letters (i.e. A and B) are significantly different at $p < 0.05$.

set; however, the results need more exploration since the parameters in the wavelet method need to be optimized.

Table 4.2 Reduced scattering coefficient (μ'_s) of different layers of the phantom, and the corresponding SNR and CNR of the *CWF* filtered phantom image

Phantom				
	1R	2	3	4
μ'_s (cm ⁻¹)	1.08	0.55	1.90	1.36
SNR (dB)	5.73	12.66	2.52	4.89
CNR	1.73	4.98	0.51	0.79

Theoretically, the *CWF* algorithm has a computational complexity of about $O((n \times m) \times \log(n \times m))$, where $n \times m$ is the size of the input image. For instance, for an input image with the size of 500×500 pixels, when a dual core processor and 4 GB memory, *CWF* filtering takes 70 seconds to perform in comparison with Wiener that takes 4 seconds.

4.6 Discussion

Even if speckle is considered as a noise in the OCT images, it carries submicron structural information of the tissue. Speckle decreases the quality, blurs the image and conceals the diagnostically relevant features. In this chapter a cluster-based adaptive Wiener filter has been presented that can enhance the quality by considering the characteristics of the tissue in the OCT image, i.e., optical properties and intensity information. The results show improvements with respect to standard approaches.

CWF makes a significant enhancement on the OCT images. Further statistical features of OCT images could be added to the feature vector to enhance the performance. Other optical properties such as the scattering coefficient, anisotropy factor and the geometrical properties can also be added. Worth to note that the proposed algorithm can be utilized as a framework for boosting any other adaptive filtering method as well. Here, the kernel filter of the proposed cluster-based algorithm is Wiener filter. By replacing the kernel (i.e. Wiener) with another adaptive filtering method, one can enhance the mentioned filter by adapting it to each individual cluster.

4.7 Conclusion

In this chapter a cluster-based speckle reduction algorithm is proposed to remove the speckle. The method successfully evaluated on the OCT images of tissue mimicking phantoms as well as the human skin *in-vivo*. As a future work, one can plan to replace the Wiener filter with other digital filtering methods in order to further improve the efficiency of the de-speckling method, e.g., total variation based noise reduction filter.

Chapter 5

Deconvolution methods for deblurring of OCT images

5.1 Introduction

An OCT setup cannot reach its theoretical resolution due to imperfections of its components, which blur the images. This blurring is different alongside regions of image; thus, they cannot be modeled by a unique point spread function (PSF).

OCT has favorable attributes for revealing microstructures within a tissue, offering 2-15 μm resolution axially and laterally and providing a penetration depth of several millimeters, depending on tissue opacity and instrument's used technology [148, 149]. Despite the fine resolution of OCT systems, there exists still the need to enhance the quality of images through improving the axial and lateral resolution. In previous efforts, researchers have implemented both hardware [150] and software solutions to enhance the resolution. Notwithstanding the fact that hardware solutions enable gathering high resolution images with desirable depth, they involve expensive and complicated optical assemblies. On the other hand, software approaches offer inexpensive mode of image resolution restoration by post-processing OCT images [151].

The deconvolution algorithm, initially introduced by Schmitt and Liang [152], is an effective software method for improving contrast and resolution of OCT images. Liu et al. [153] used space invariant point spread function (PSF) to implement a procedure based on two successive 1D deconvolution (laterally and axially) and a procedure based on a 2D deconvolution.. In another approach, Wooliams et al. [154] carried out PSF measurement of OCT setup by designing special phantoms and performed space variant deconvolution of many sub-images from their corresponding PSFs.

Previously an algorithm is developed by utilizing Lucy-Richardson deconvolution algorithm with PSFs exploited and modeled from their corresponding unprocessed ones [155].

Despite all the improvements presented in these papers, deficiencies in modeling and enhancing different degradation in various regions of image are still present. In this chapter, a new spatially variant deconvolution

method is proposed for OCT images based on Total Variation (TV). It is shown that this method can effectively reduce blurring of OCT images as well as mitigating the speckle noise.

5.2 Formalization of an iterative deblurring method based on Total Variation

Recalling interferometric based imaging, the OCT interference signal is given by (5.1).

$$I(\tau) = 2 \operatorname{Re}\{f(\tau) \otimes \Gamma(\tau)\} \quad (5.1)$$

where τ denotes the time, $f(\tau)$ is the impulse response function of the sample and $\Gamma(\tau)$ is the coherence function of the light source, that is the inverse Fourier transformation of the power spectral density (PSD) [6]. For a light source with a distribution of Gaussian shape, Gaussian beam equation for planar phase-fronts can be written as (5.2) [156].

$$G(x, y, z) = \frac{w_0}{w(z)} \exp\left(-\frac{x^2+y^2}{w^2(z)}\right) \exp\left(-j\left(k_0 + \frac{\omega-\omega_0}{v_g}\right)z\right) \quad (5.2)$$

where v_g is the group velocity, ω_0 is the frequency of the light, k_0 is center wavenumber, w_0 is the waist radius, and x, y are the transverse coordinates, and z is the axial coordinate where at the boundary of the confocal region. Solving the first order Born approximation (using Green function) and doing some math, the OCT signal can be reconstructed. The OCT corresponding coherence function, longitudinal PSF of the OCT, can be formulated as (5.3):

$$\Gamma(\tau) = \exp\left(-\frac{\pi \Delta \lambda \tau c}{2\sqrt{\ln 2} \lambda_0^2}\right)^2 \exp\left(-i \frac{2\pi \tau c}{\lambda_0}\right) \quad (5.3)$$

where c is the speed of light in free space and λ_0 and $\Delta \lambda$ are the central wavelength and the spectral width of the light source, respectively.

On the other hand, the transverse PSF of the OCT system is given by equation (5.4).

$$w_0 = \frac{2 \lambda_0 f}{\pi D} \quad (5.4)$$

The PSF of an OCT system can be approximated by imaging very small particles embedded in a very transparent solid phantom, with a diameter much smaller than the coherence length of the OCT system. The known Lucy-Richardson deconvolution algorithm is an iterative non-linear procedure based on calculating the maximum-likelihood solution, for recovering an undistorted image that has been blurred by a known PSF. The algorithm resolves the image via an iterative process that has been successfully used for OCT deblurring [61, 66, 157].

In practice, without loss of generality, with discrete arrays of pixels as images, the degradation process can be considered as the linear inverse problem as in (5.5)

$$g = Hf + n \quad (5.5)$$

Where g and f denote vectors of a true object and its observed image, H is the observation matrix corresponding to PSF, and n is a vector of zero mean sample of white Gaussian noise vector with covariance $\sigma^2 I$, where I is the identity matrix.

Generally, the determination of f is an ill-conditioned problem. With some a-priori information about the original image distribution a regularization method can solve the problem.

In this study a Total Variation (TV) regularization is used to handle the ill-posed nature of f given in (5.6).

$$\hat{f} = \underset{f}{\operatorname{argmin}} L(f) \quad (5.6)$$

Where $L(f)$ is given by (5.7).

$$L(f) = \|g - Hf\|^2 + \lambda TV(f) \quad (5.7)$$

A discrete version of TV regularization constraint is defined by (5.8)

$$TV(f) = \sqrt{\sum_{m \in \psi_i} (\Delta_i^h f)^2 + (\Delta_i^v f)^2} \quad (5.8)$$

Where Δ_i^h and Δ_i^v are linear operators that calculate local variation (horizontal and vertical gradients) of f at pixel i , and $\psi_i = \{(x_i + 1, y_i), (x_i, y_i + 1), (x_i - 1, y_i), (x_i, y_i - 1)\}$ is a local neighborhood around $X_i = (x_i, y_i)$.

An iterative scheme for minimizing the resulting cost function can be applied. In particular, for minimizing the objective function, a Majorization-Minimization (MM) approach [158] is used that replaces the difficult optimization problem with a sequence of simpler ones. By deriving a quadratic function for L and finding a majorizer for it, our optimization problem can be replaced with the following updated equation (5.9) and (5.10).

$$f^{(t+1)} = (H^T H + D^T W^{(t)} D)^{-1} H^T g \quad (5.9)$$

where $W^{(t)} \equiv \text{diag}(w^{(t)}, w^{(t)})$ in (8).

$$w^{(t)} = \left[\frac{\lambda/2}{\sqrt{(\Delta_i^h f^{(t)})^2 + (\Delta_i^v f^{(t)})^2}}, i = 1, 2, \dots \right] \quad (5.10)$$

Since obtaining $f^{(t+1)}$ via equation (8) is computationally expensive, this problem is handled by replacing the minimization part with conjugate gradient (CG) iteration [159]. The pseudo code of algorithm is given in algorithm 5.1.

Algorithm 5.1 Pseudo code of proposed deblurring algorithm

Initialization: $x_0 = y'$

For $t=0$ to StopRule do

$W^{(t)} = \text{diag}(w^{(t)}, w^{(t)})$

$x^{(t+1)} = x^{(t)}$

While $\|A^{(t)}x^{(t+1)} - y'\| \geq \varepsilon\|y'\|$ do

$x^{(t+1)} = \text{Next iteratin}$

End While

End For

5.3 Phantom construction for PSF extraction

To make the solid phantom for PSF estimation, TiO_2 is dissolved in castable polyurethane (WC-781, BJB Entprise Co., US). The final

concentration of TiO₂ is 20,000 particles / μ L. The mixture was then placed into an ultrasound bath to produce a homogeneous phantom. Details of Mie scattering parameter calculation are analogues to what is given in Chapter 3. At such concentration, the OCT image will have approximately 1 particle in the area of 30 by 30 pixels. Thus, the image acquired from each particle represents the PSF of the OCT system at the specific location. By averaging nearby reliable spots images from several layers, besides getting benefit from removing noise and possible distortions, one able to organize a PSF-map which shows variations of PSF at different locations. Figure 5.1 shows an example of how to extract a 4 \times 4 PSF-map.

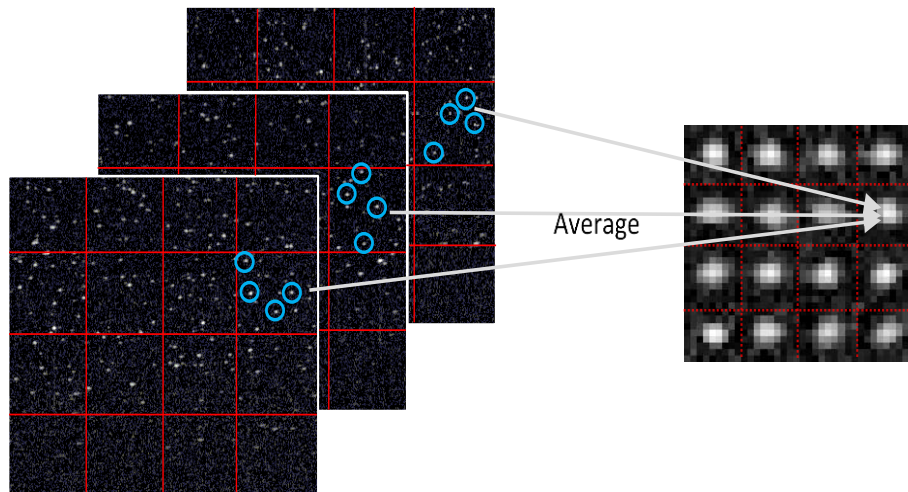


Figure 5. 1 raw images of phantoms and selection of reliable spots for construction of PSF-map

After constructing a PSF-map, the performance of two different deconvolution methods named Lucy-Richardson, and TV-based approach are evaluated in sharpening and enhancing the quality of OCT images. In order to use Lucy-Richardson algorithm with spatially-variant PSF, first the sum of intensities of PSFs are normalized for each region of PSF-map for the sake of avoiding blocking effect. Then the algorithm is utilized for each sub-region and aggregated the sub-images to assemble the full deconvolved image.

5.4 Results and discussion

In Figure 5.2 (a) the true synthetic test image (b) its blurred image with represented PSF-map, and results of (c) Lucy Ricardson and (d) proposed TV based deconvolution methods for enhancement has been depicted.

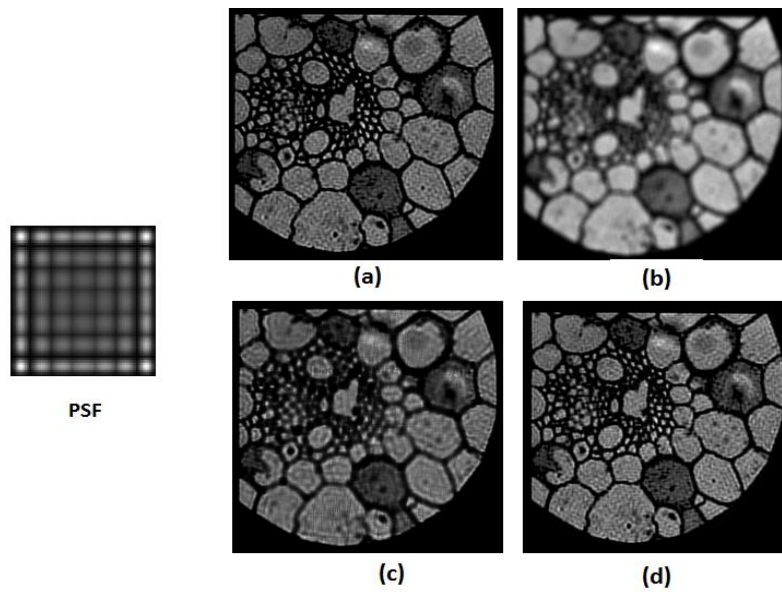


Figure 5. 2 (a) Test image (b) its blurred the with represented PSF-map, and (c) results of Lucy Ricardson (d) propped TV based deconvolution methods

Figure 5.3 illustrates the performance of these two methods on OCT optical phantom image. In Figure 5.4. the results (c) Lucy-Richardson method with 3 iteration (d) TV-based method with 1 iteration on OCT original image from back of a 24 year old male (a) is given.

In table 5.1, three computed parameters for assessment of deconvolved images is given. These parameters including SNR, CNR and ENL will justify the quality improvement of deconvolved images so far.

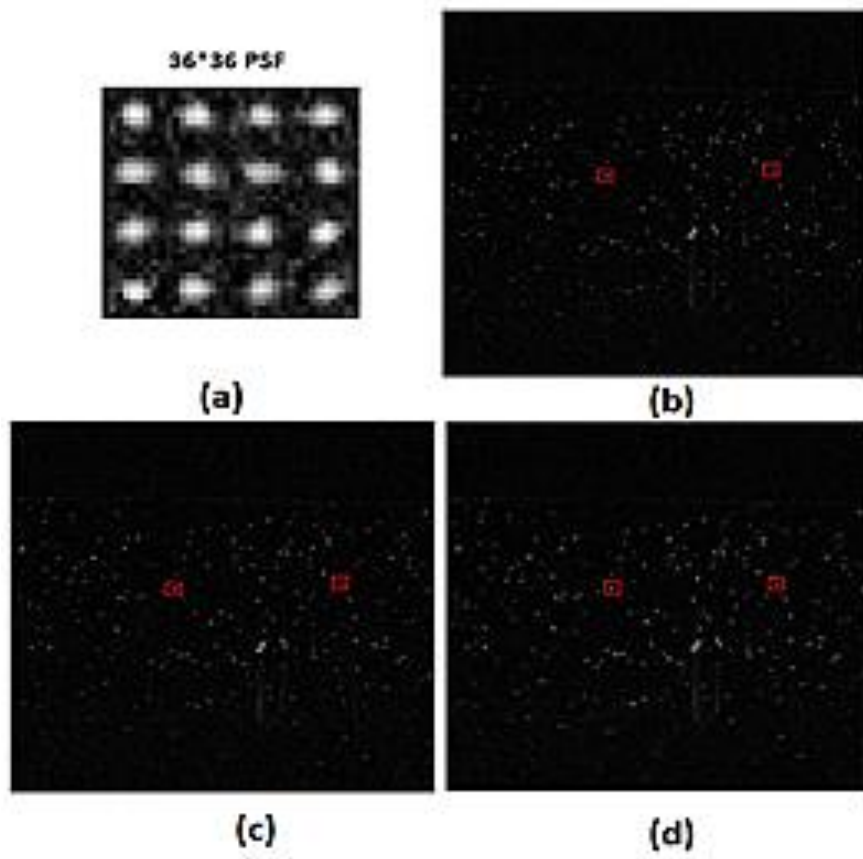


Figure 5. 3 (a) OCT phantom image (b)) results of Lucy Ricardson method (c) proposed TV based deconvolution method each with 5 iterations

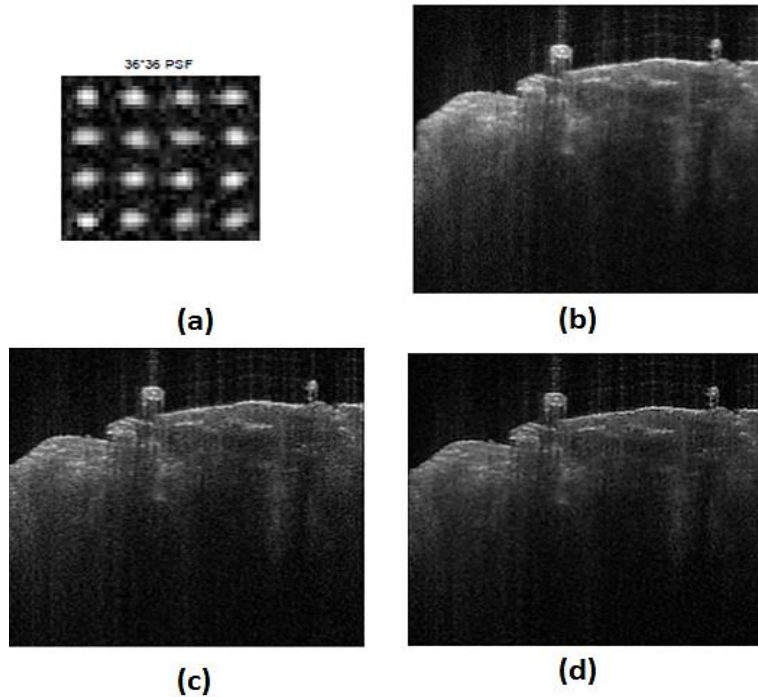


Figure 5.4 (a) Synthetic PSF-map (a) OCT original image from back of a 24 year old male , (c) Lucy-Richardson method with 3 iteration (d) TV-based method with 1 iteration

Table 5.1 calculated parameters for original image and three deconvolution methods

Method\parameter	SNR	CNR	ENL
Original image	18.55	0.98	174.2
Lucy-Richardson	20.78	1.254	226.79
TV based	21.82	2.07	717.4

The suggested TV-based method has this advantages that the spatially-variant blurring in H matrix can be modeled even with one-pixel resolution and it could mitigate noise unlike other deconvolution methods. However in terms of elapses time, Lucy Ricardson algorithm is more efficient. According to spatially-variant nature of PSF for OCT systems, the PSF-map with imaging proper phantoms is elicited. TV based approach yielded the best results qualitatively and quantitatively due to its supremacy in modeling PSF and its intrinsic smoothing property. Using one pixel resolution PSF instead of our sub-region-invariant PSF used in this work,

one can model the space-variance of PSF better, resulting in improvement of this outcome.

5.5 Conclusion

In this chapter, the use of solid phantoms to estimate the PSF of each sub-region of imaging system is investigated. Then Lucy-Richardson and total variation (TV) based iterative deconvolution methods are utilized for mitigating occurred spatially variant blur. It's shown that the TV based method is suppressed the so-called speckle noise of OCT images in addition to outperforming the two other approaches. The performance of proposed algorithm is tested on various samples, including several skin tissues besides the phantom itself, demonstrating qualitatively and quantitatively the advantage of TV based deconvolution method using spatially-variant PSF for enhancing image quality. In future works, one can improve the mathematical relations for TV approach in order to improve noise configuration model.

Chapter 6

Localization of Dermal Epidermal Junction in OCT images of skin

6.1 Introduction

The Dermal epidermal junction (DEJ) is the border between the dermis and epidermis, and thus is an important landmark dividing two areas of the skin that have different function and morphology. Knowledge of its location plays an important role in evaluating many dermatological diseases [86, 87], for example basal cell carcinoma (BCC), which is located in the deepest layer of the epidermis and invades the dermis [88-90]. Moreover, DEJ plays an important role in the intracellular pool of bullous pemphigoid antigen, the interactions between fibronectin and keratinocytes and the epidermolysis bullosa acquisita antigen areas [91]. On the other hand, knowledge of DEJ is important in determining whether a sub-surface lesion is BCC. To localize DEJ, the OCT image of skin is segmented. Here, a novel approach is proposed that uses attenuation map as a complementary feature compared to the previous methods that are mostly based on intensity information. The method is based on converting a border segmentation problem to a shortest path problem using graph theory. To smooth borders, a fuzzy algorithm is introduced, enabling a closer match to manual segmentation.

6.2 Methodology

The proposed algorithm, illustrated in Figure 6.1, is carried out by detecting skin surface and papillary-reticular dermis junction (PRJ). Three border boundaries are determined in this framework, and, for each of the boundaries, the same series of operation is considered. Figure 6.2 outlines the operations. According to Beer-Lambert law, the total attenuation of a signal in the OCT image is under the influence of absorption and scattering of light traveling within the skin [160, 161]. In the OCT imaging the effect of attenuation on intensity is linear (due to the logarithmic function used in the OCT image reconstruction algorithm) [162]. Therefore, a linear

function, $f(x) = cx + d$, can be fitted to each A-line to represent the attenuation

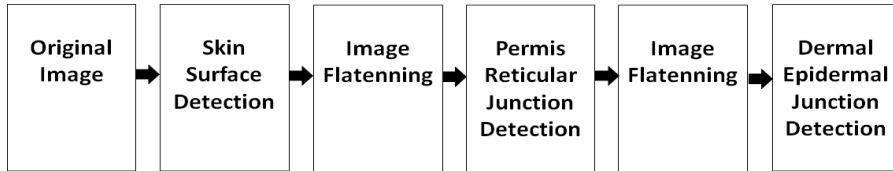


Figure 6. 1 DEJ localization algorithm

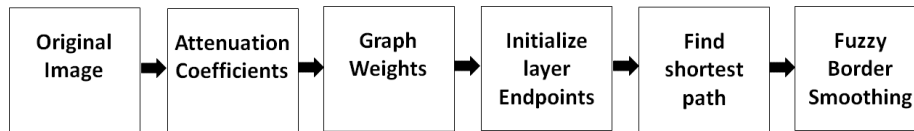


Figure 6. 2 Border boundary detection algorithm

by the gradient c . A linear least square curve fitting algorithm is used to extract an average c for each A-line [163]. the image is represented as an undirected graph $G(V, E)$ where each pixel is mapped into nodes (V), and links (E) that show the connections of the nodes so-called edges. Our goal is to transform an image into a graph in order to convert a segmentation problem to a find-the-shortest-path problem. After creation of the graphical representation of the attenuation map, a set of weights is computed for each link (E). The key to accurately finding the shortest path in a graph is to assign appropriate weights to the edges. The weights on links are used to represent the intensity difference of the graph nodes in the OCT image [164]. The weight, w , of edge (m, n) is defined as (6.1).

$$w_{(m,n)} = (1 - a_m) + (1 - a_n) + w_{min} \quad (6.1)$$

where a_m and a_n are coefficients of absorption in node m , and n , respectively, normalized between 0 and 1, and $w_{min}=10^{-5}$. Once appropriate weights are assigned to each link, the shortest path is calculated through Algorithm. 1. In an interactive framework, the user chooses two pixels on the OCT image as the starting point and end point. The user allowed to select some other points as arbitrary points in the short path problem.

Recalling from the previous section, the proposed segmentation problem is based on identifying the shortest path from the graphical representation of our image. In the shortest path problem, the length of a path defines the

sum of weights along the path. Therefore, the algorithm searches a path that passes through links with smallest weights. In this study, the Dijkstra algorithm is used to solve the shortest path problem. Dijkstra algorithm keeps two sets of vertices: S which is a set of vertices whose shortest paths from the start node (s) have already been determined, and $Q=V-S$ is the remaining vertices. The algorithm chooses the vertex $n \in Q$ with the shortest path estimate, adds n to S and eliminates it from Q . This process is repeated until the end point (e) belongs to S . At the end, S returns to the shortest path [98],19].

Algorithm.1 Pseudocode of finding the shortest path

Require Graph $G = (V, E)$, start point s and end point e
 Initialization:
 $S = s$ and $Q = V$
 $cost[V] = Infinity, cost[s] = 0$
 While $e \notin S$ do
 for each vertex $n \in Q$ adjacent to $m \in S$ do
 $cost[n] = minimum(cost[n], cost[m] + w(m, n))$
 End For
 Select the vertex n with the minimum $cost[n]$
 $S = S \cup n$
 $Q = V - S$
 End while
 Return the shortest path of S

In order to closely match the manual DEJ detection with the results of the proposed method, obtained borders were smoothed using a fuzzy system. In the design of a fuzzy system, (figure 6.3, parameters such as fuzzifier, rule base, inference engine, and defuzzifier should be determined. A singleton fuzzifier, weighted average defuzzifier and memdani fuzzy inference system is used. In our designed fuzzy system, the rules base is the coordinates of the detected border obtained from the implementation of Dijkstra algorithm. In each fuzzy rule, premise (if) is the column index in the image and the consequence (then) of rule is the estimated border location in each column. Thus, the number of fuzzy rules are equal to the number of image columns (image width (w)). I determined the following rules:

Rule1: if $x = 1$ then $f(x) = \text{border index } (1)$

Rule2: if $x = 2$ then $f(x) = \text{border index } (2)$

.

.

.

Rule w : if $x = w$ then $f(x) = \text{border index } (w)$.

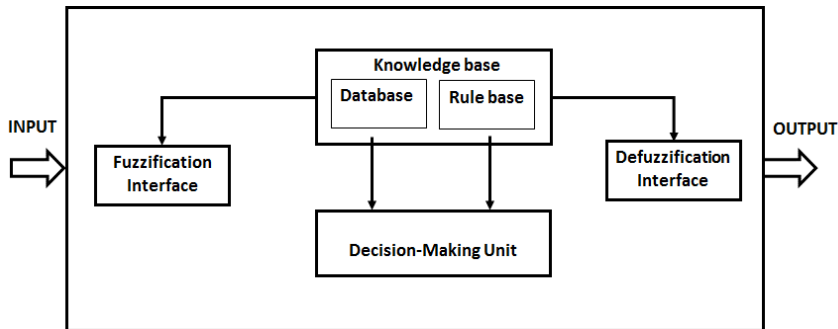


Figure 6. 3 Schematic of fuzzy system for border smoothing.

border index (i) is border in i^{th} column, w is image width and determines the number of rules in rule base. Finally, one can reach (6.2) and use it to smooth the resulting border.

$$f(x) = \frac{\sum_{i=1}^w y_i \exp\left(-\left(\frac{x-x_i}{\delta}\right)^2\right)}{\sum_{i=1}^w \exp\left(-\left(\frac{x-x_i}{\delta}\right)^2\right)} \quad (6.2)$$

where y_i is the calculated depth, corresponding to the index of i^{th} column, δ is the standard deviation of selected border pixels and $f(x)$ is the smoothed border index in x^{th} column. Figure 6.4 shows the result of the obtained DEJ by solving the shortest path problem and the effect of fuzzy system on DEJ border. The images are taken from the inner arm of a 25-year female individual.

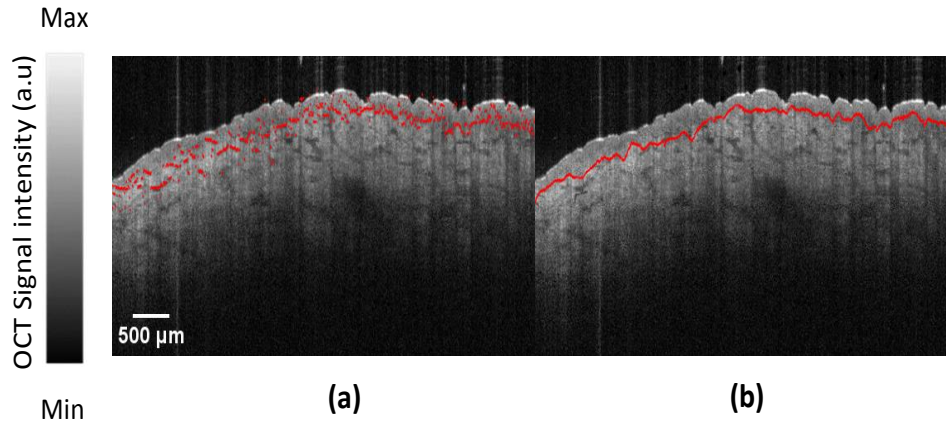


Figure 6. 4 Results of border smoothing using the proposed fuzzy system on inner arm. (a) DEJ before smoothing; (b) DEJ after smoothing.

In the DEJ localization algorithm, initially skin layers are detected. A proposed skin layer detection algorithm based on determining the lowest weighted path of a graph between arbitrary endpoints is used. The algorithm begins by calculating an attenuation map (Figure 6.5 (b)). Afterwards, the start, end and arbitrary points on the skin surface are selected by the user for each border, meaning that the user identifies points on the skin surface, PRJ and DEJ borders and then Dijkstra algorithm for skin surface detection is applied. Figure 6.5 (c) illustrates an example of skin surface detection. After the skin surface detection, the image would be flattened following equation (6.3):

$$I_f(x; y) = I(x; y) - sf(x) \quad (6.3)$$

where, $I(x; y)$ is the original image and $sf(x)$ is the skin surface. Once the skin surface is detected and the image is segmented, the PRJ can be detected. The result is shown in Figure 6.5 (d). PRJ is a junction that is located between papillary and the reticular dermis. To estimate PRJ, the proposed skin surface detection method, illustrated in Fig.3, is performed. Figure 6.5 (e) illustrates the attenuation map of the image shown in Figure 6.5 (d). Afterwards, a continuous line from light-to-dark region is obtained (Figure 6.5 (f)) based on the start and end points as well as the auxiliary points. The shortest distance problem is solved with the Dijkstra algorithm. Finally, the smoothing is done with a fuzzy system. Using $sf(x)$ as the upper

border and $prj(x)$ as the lower border, the bounded region between these borders is obtained by (6.4):

$$I_b(x; y) = prj(x) - sf(x) \quad (6.4)$$

where $prj(x)$ is the coordinate of the column of the papillary-reticular dermis junction. Using the PRJ information, the DEJ is detected on the flattened image (I_b) and depicted on F Figure 6.5 (g). The method described above is used three times to detect the skin surface, PRJ and DEJ. Figure 6.5 (i) illustrates the final results. In this result, DEJ overlaid on the original image is shown. The aim of the flattening procedure was to remove the region above the air-skin interface in PRJ estimation stage and also to remove the region underneath the

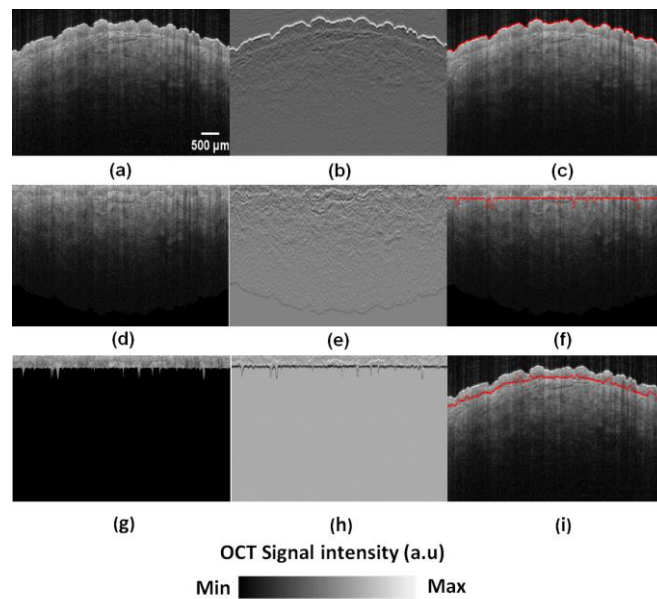


Figure 6. 5 Results of the proposed DEJ detection algorithm on inner arm OCT images. (a) Original OCT image; (b) attenuation map of the original image; (c) skin surface detected image; (d) flattened original image; (e) attenuation map of the image in (d); (f) PRJ overlaid on the flattened image; (g) area bounded by skin surface and PRJ; (h) attenuation map; (i) DEJ overlaid on the original image.

PRJ boarder in DEJ detection procedure. In this way, the shortest path problem becomes easier to solve and becomes more efficient since the

search region has been shrunk. In other words, when the skin surface is detected, we declare all nodes which belong to the abovementioned regions as invalid search regions while searching for the PRJ boarder.

6.3 Results and discussion

The DEJ algorithm has been applied on 115, B-Scan OCT skin images taken from different sites of body, including Inner arm, outer arm, periarticular, palm, neck, thumb, back, and outer leg of healthy individuals. Figure. 6.6 shows the results of the DEJ detection algorithm on some of the OCT images in comparison with the results of manual DEJ detection performed by experts. The experts were from dermatology from the dermatology Department of Dermatology at Wayne State University as well as from Oakwood hospital in Dearborn, MI.

The epidermal thickness (ET) is also calculated for the images mentioned above. The average distance between the DEJ and the upper skin surface boundary is considered the epidermal thickness. The averaged values as well as standard deviation (SD) of ET are reported in Table 1, and compared with the values given by experts.

The root-mean-square error (RMSE) is also calculated for the OCT images. RMSE is obtained by equation (6.5):

$$RMSE = \sqrt{\frac{\sum_{i=1}^n (S1[i]-S2[i])^2}{n}} \quad (6.5)$$

Where S_1 and S_2 are epidermal thickness obtained by expert and the proposed method, respectively and n is the number of OCT images. Small values of RMSE show the similarity between the epidermal thickness results obtained by experts and the proposed method for different sites of body. The Pearson correlation coefficient r , between the results produced by the algorithm and those given by the experts, is computed as 0.99, which indicates the high accuracy of the proposed method.

Table 6.1 ET calculated by the proposed algorithm and obtained from expert's opinion

Sites of body	Number of OCT images	Mean thickness by expert	Mean thickness by algorithm	RMSE (mm)

		(mm) mean \pm SD	(mm) mean \pm SD	
Prearicular	20	148 ± 6	141 ± 14	11
Inner arm	15	146 ± 5	139 ± 9	9
Outer arm	15	150 ± 7	158 ± 10	8
Neck	15	171 ± 8	177 ± 7	11
Back	5	142 ± 9	150 ± 12	10
palm	15	310 ± 8	314 ± 6	9
Thumb	15	733 ± 20	725 ± 20	14
Outer leg	15	151 ± 8	156 ± 7	8

Figure 6.9 shows Pearson correlation plot between the proposed method for ET measurement and manual DEJ detection results [97, 99][12,14]. To compare the proposed method and the manual segmentation results, the Bland-Altman [165] is plotted. The results show that all of the differences lie between -14 and +15.0.

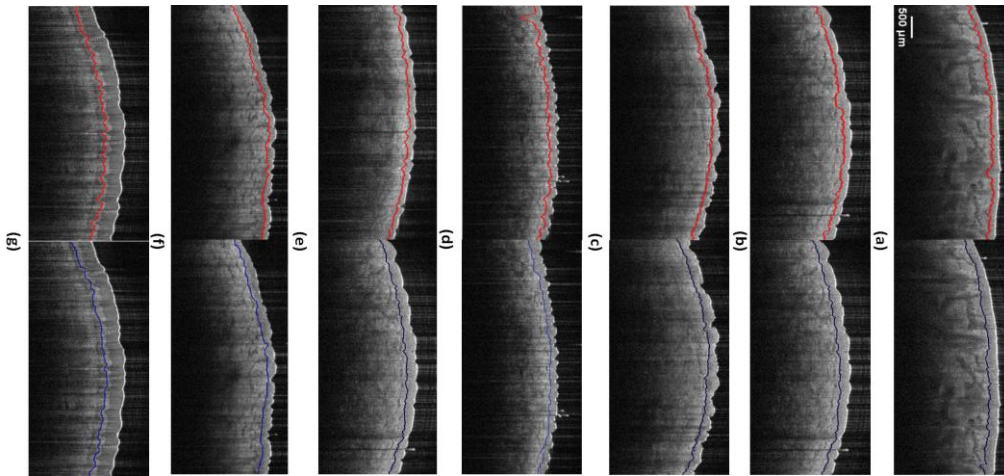


Figure 6. 6 Application of the proposed DEJ detection method on OCT images of (a) Prearicular; (b) outer arm; (c) inner arm; (d) back; (e) outer leg; and (f) neck. (g) Palm, the red color is DEJ obtained from the proposed DEJ algorithm. The blue color is DEJ drawn by an expert.

microns (See figure 6.10). This is logical compared to the resolution of our OCT that is 10 microns. In further analysis, we found out this error is desired for determination of epidermal thickness in evaluating BCC disease

when it is compared with the mean BCC tumor thickness ($0.65 \text{ mm} \pm 0.29 \text{ mm}$) measured in [166]. Considering the fact that our system of imaging and resolution of images is similar to mentioned work. More careful selection of end points and arbitrary points can help to have a more accurate DEJ results.

It also reduces the search time for the algorithm for the best DEJ found. If the OCT images have shadowing artifacts or experience low contrast [48, 66, 167], the algorithm will require more number of arbitrary points.

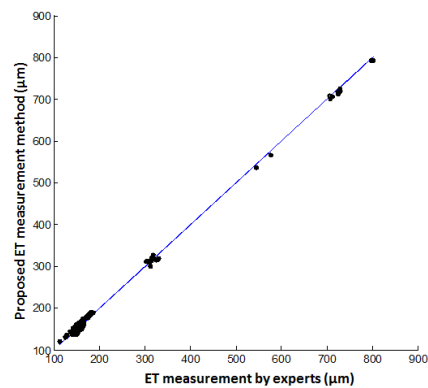


Figure 6. 7 Correlation between the proposed method and expert's opinion for ET measurement.

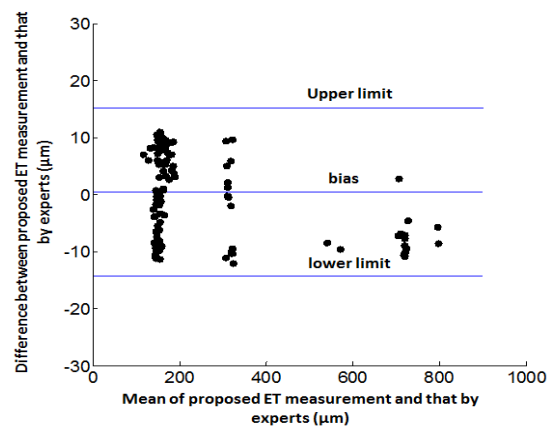


Figure 6. 8 Bland- Altman plot.

6.4 Conclusion

In this chapter, a novel approach for DEJ detection is proposed based on the graph theory. To the best of our knowledge, this algorithm is the only DEJ detection algorithm that performs with more than 99% success rate. The proposed algorithm is useful to assist diagnosis of skin diseases related to epidermal thickness change, e.g., BCC. The results of the algorithm are evaluated on different sites of body and compared them with those obtained from manual measurements. The results were closely matched. Our algorithm could be used on OCT images obtained from other OCT imaging systems, e.g., time domain OCT (TD-OCT) or high definition OCT (HD-OCT). The proposed algorithm might give an even more accurate result than the manual segmentation of the experts' manual detection, as it is automatic and doesn't have any subjectivisms. The algorithm can be used as add-on software to any OCT machine's operating system to give dermatologists more information about the skin.

Chapter 7

Universal in-vivo textural model for Human skin

7.1 Introduction

According to specific functional needs, skin architecture varies across different parts of body, and so does the textural and morphological characteristics in the OCT images. There is, therefore, a critical need to systematically analyze OCT images of different sites and identify their significant qualitative and quantitative differences. In this chapter, the aim is to create a comprehensive model of human skin in-vivo using OCT images and to use such a model to detect /diagnose common skin disorders. To this end, Optical, textural, and statistical properties extracted from OCT skin images are analyzed and used to create a perceptual and computational model of the normal skin at different anatomic sites. Moreover, using pattern recognition methods, skin tissues is characterized. It is demonstrated that such a dynamic model in conjunction with decision-theoretic approaches can assist in the diagnosis of different microstructural cutaneous abnormalities, and hence aid in the determination of treatment.

7.2 Materials and Methods

The study is designed to be completed in two phases. In the first phase, textural and optical features extracted from the OCT image of human skin at different sites of body in-vivo are used to make a dynamic computational model of the healthy skin. The model is verified by correlating skin microstructures identified in OCT images by expert dermatologists with features obtained from the images. In the second phase, the model is used to diagnose /monitor dermatological conditions. The features in the model are modified and weighted appropriately according to the characteristics of a particular skin condition (see figure 7.1).

OCT images of healthy skin is taken from ten volunteers, aged between 25 to 56 years old, none of whom had any skin conditions. For each subject, sites including the nose, preauricular, volar forearm, neck, palm, back, thumb, dorsal forearm, sole, calf is imaged and analyzed for the first phase of study. The diseased images are taken from 11 patients whose disease was confirmed by histopathology. All imaging procedures is carried out according to the guidelines of the US National Institutes of Health, and institutional review board (IRB) approval committee of the Wayne State University. Histology images for the skin conditions are collected in the Wayne State University Physician Group Dermatology Clinic, Dearborn, MI.

7.2.1 Data Analysis

Healthy human skin OCT images are initially segmented into two skin main layers' epidermis and dermis using the semi-automatic segmentation elaborated in chapter 6. Following the algorithm given in figure 7.1, optical, statistical and textural features are extracted from the OCT images. To suppress the speckle noise [40], the speckle reduction method in chapter 4 is used. The feature vectors are constructed extracting following features. *Optical*: 25 A-scans in each ROI are averaged. The global attenuation of the sample was evaluated using the slope of the fitted curve. Levenberg Marquardt algorithm is used for curve-fitting. *Statistical texture (First order statistical)*: Statistics including mean, variance, standard deviation, skewness, median, entropy and kurtosis as First Order Statistics (FOS) are calculated for each ROI. FOS refers to location, spread, symmetry, and peakedness of a histogram. Entropy (randomness) and median are also extracted. *Textural features (second order)*: Second order statistics, i.e., Grey Level Co-occurrence Matrix (GLCM) [122, 168] is based on the probability function of inter-pixel correlations at a certain distance in the image. The second order texture offers information about image spatial distribution of pixel values in a given angular direction. Homogeneity, contrast, energy, entropy and correlation are second order statistics. *Textural features (Higher order)*: Higher order statistical features, i.e., grey level run length matrix (GLRLM) [122, 168], is based on gray level run of various lengths, where a gray level run is the number of gray levels in a consecutive and collinear pixel points having the same gray value.

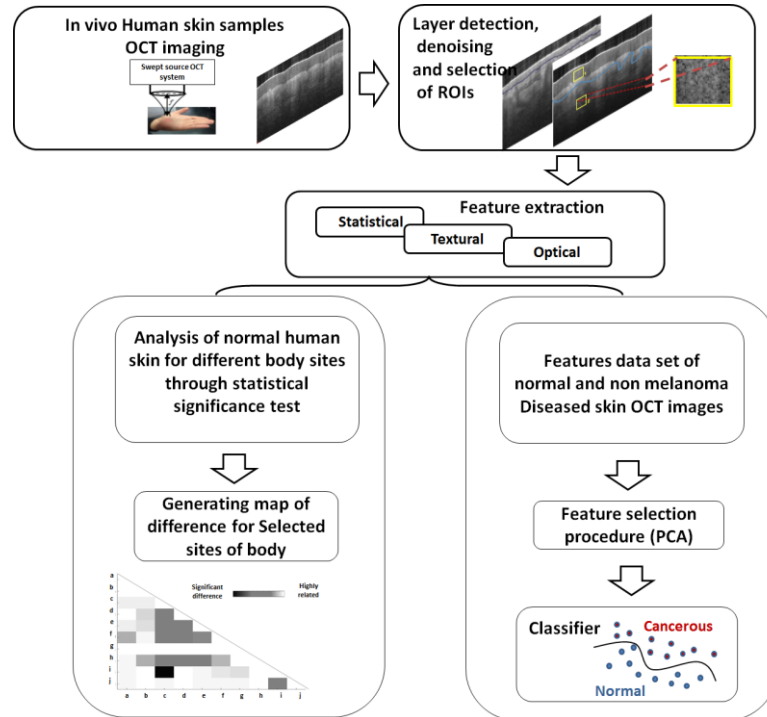


Figure 7. 1 Schematic diagram of the proposed method, a-j are; a: Neck, b: Preauricular, c: Tip of Nose, d: Back, e: volar forearm f: dorsal forearm, g: Palm of hand, h: calf, i: Thumb, j: sole

A feature vector is constructed comprised of FOS textures (variance, mean, skewness, kurtosis, entropy), Haralick GLCM textures (homogeneity, entropy, energy, contrast and correlation), and GLRLM features in four angular directions, i.e., 0° , 45° , 90° and 135° . The mean of the obtained features for dermis and epidermis and their corresponding 95% confidence intervals (CI) across different skin sites are estimated. The differences in image features between sites are compared using T-test. The Minitab Statistical Software (version 17.0, Minitab Inc., Pennsylvania, USA) is used for statistical analyses.

7.2.3 Classification

Prior to the classification, features are normalized, then feature selection algorithm is performed to obtain the most discriminative features. Principal

component analysis (PCA) as our feature selection method. The PCA finds a linear map from the data in a high dimensional space to a desired low dimensional space trying to preserve the data variance. A modified PCA following the work in [169], performed to obtain the principal components. Then features which provided the greatest contribution to the first four principal components are kept. After feature selection was performed, the images are determined to fill the learning database are classified using machine learning classifiers, i.e., SVM [170] with two different kernels such of Linear and 2nd degree polynomial kernel, Logistic Regression (LR), K-Nearest Neighbor classifiers, Linear Discriminant Analysis (LDA) and Artificial Neural Networks (ANN). Although the main SVM is designed to solve linear classification tasks, by using some kernel tricks it is used for nonlinear classification tasks and it is very well suited for binary (two class) problems [171]. In LR classification, the probability that a binary target is true is modeled as a logistic function of a linear combination of features[172]. For K-Nearest Neighbor (KNN) [173], the rule classifies each unlabeled sample by the majority label among its K-nearest neighbors in the training set. LDA, searches for a linear combination of variables that best separates binary targets[173]. An ANN [174] classifier consists of many neurons, i.e., highly interconnected processing components, that work constructively and coherently to solve specific problems.

Classifiers are validated using 10×10 -fold cross-validation method. In 10-fold cross-validation, the data is randomly split into 10 equal folds. The classification procedure is implemented in an iterative manner. For each run nine folds are used for training and one fold is used for testing. The process is repeated ten times and the final accuracy is the average of all the fold accuracies. The approaches described in this study have been implemented in Matlab® 2016, and the experiments are carried out on a standard computer workstation (3.10 GHz Intel Core i7, 32 GB RAM). I used developed custom routines and Matlab's built-in functions.

7.2.4 Other imaging modalities

The other imaging modalities used in this study, in addition to the SS-OCT, are as follows: an HD OCT, a clinical ultrasound, a high frequency (HF) ultrasound (48MHz), and an ultra-high frequency (UHF) ultrasound (70 MHz). The HD-OCT is a time domain high definition (HD) Skintell OCT (AGFA HealthCare Inc., Mortsels, Belgium). The field of view of this OCT system is 1.8 mm (length) by 1.5 mm (width) by 1 mm (depth). The axial

and lateral resolutions of this machine are $\sim 3\mu\text{m}$. The clinical (Low frequency) Ultrasound machine has 92 elements linear array (S9 Sonoscope, UMS Solutions, Sonoscope.Inc., USA) with the central frequency of 15 MHz. The High and Ultra-High frequency Ultrasound probes are Vevo MD (FUJIFILM VisualSonics, Inc., Canada). The probes are linear array with 128 elements and a central frequency of 48 MHz and 70 MHz, respectively.

7.3 Results

7.3.1 Healthy skin in OCT images

The basic structure of the skin includes the epidermis, dermis, and subcutaneous fat. The epidermis is four to five layers of stratified epithelia with no blood vessels, the most superficial being the stratum corneum. The epidermis connects to the dermis by a layer known as the dermo-epidermal junction (DEJ). Cutaneous appendages, including nerves, glands, and hair follicles, reside in the dermis. Skin adapts its color, thickness, and texture in different parts of the body according to specific functional needs. Based on the thickness of epidermal layers, human skin can be divided into two main types, thick skin and thin skin [175, 176]. Another skin type, mucocutaneous skin, is where mucosa transitions to stratified squamous epithelium, e.g., lips. In this study, I have looked at nose, pre-auricular, neck, upper extremities and lower extremities, palms, soles and back as representative of the variety of skin architectures and epidermal thicknesses across the body [177]. The most notable features of palm, thumb and sole, i.e., thick skin, are their thick stratum corneum, presence of a stratum lucidum, an abundance of eccrine sweat glands, and lack of hair follicles, sebaceous glands and apocrine glands. In OCT images of thick skin, the stratum corneum is the first visualized layer of the epidermis, appearing as a homogenous layer of cells with scattered eccrine sweat ducts [178] (Figure 1.7 (e), (g) and (i)). The eccrine sweat ducts of thick skin have a recognizable spiral lumen when observed with high intensity of reflected light, a result of the large refractive index mismatch between sweat and the keratinocytes of the epidermis [179]. The stratum lucidum, a clear thin layer of dead cells visualized only in the thick skin, is just beneath the stratum corneum [180]. The prominent morphological features of nose, preauricular, volar forearm, neck, back, dorsal forearm, and calf, i.e., thin skin, are: thinner epidermis, no stratum lucidum, hair and sebaceous

glands. The stratum corneum of thick skin is about 300 μm , in contrast to an average of 14 μm in thin skin, where it is too thin to be visualized in detail by OCT [13, 181]. The epidermis of thin skin sites fluctuates 70 μm to 120 μm where the full thickness of the epidermis plus the dermis varies between 1000 μm to 2000 μm . The OCT B-scan images of nose, preauricular, volar forearm, neck, palm, back, thumb, dorsal forearm, sole, calf shown in figure 1.7, are taken from volunteers aged between 25 and 59 years old, none of whom had any skin conditions. The images are acquired from the same area of ten healthy individuals. A specialized holder is used for the OCT probe for this purpose.

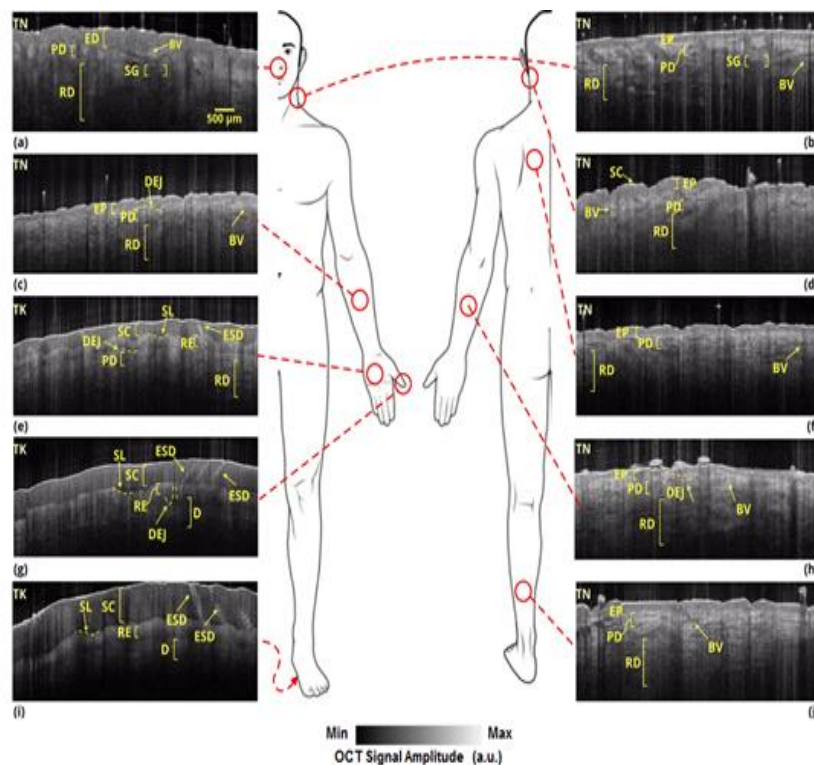


Figure 7. 2 OCT images of different sites of body (a) nose, (b) preauricular, (c) volar forearm, (d) neck, (e) palm, (f) back, (g) thumb, (h) dorsal forearm, (i) sole, (j) calf (e). SC: Stratum Corneum, SL: Stratum Lucidum, ESD: Eccrine Sweat Ducts, RE: Remainder of Epidermis (stratum granulosum, stratum spinosum, stratum basale), RD: Reticular Dermis, DEJ: Dermal-epidermal junction showing pronounced dermal papillae, PD: Papillary Dermis, D: Dermis,

EP: Epidermis, SG: Sebaceous Glands, BV: Blood Vessels, TK: thick skin, and
TN: thin skin.

7.3.2 Diseased skin in OCT images

The cellular characteristics of the diseased skin, hence the corresponding features in the OCT image, are altered compared to those of healthy skin. The diseased images in this study are taken from 11 patients whose disease was confirmed by histopathology. All imaging procedures are carried out according to the guidelines of the US National Institutes of Health, and institutional review board (IRB) approval committee of the Wayne State University.

Several skin diseases have been studied in the literature using OCT including nonmelanoma skin cancer, melanoma and benign pigmented tumors. I studied epithelial skin tumors, i.e., BCC, SCC for this study. The features of BCC in OCT have been well described. The main change is the disruption of the normal layering of the epidermal and dermal layers. The tumor lobules are represented by hyporeflective rounded structures surrounded by a halo of hyper-reflection [182, 183]. Typically, the tumor is accompanied by dilated blood vessels [184-188]. In the superficial subtype of BCC, tumor nests extend from the epidermis, while tumors in nodular BCC may be completely in the dermis. In both the OCT and histology images of BCC, the central portion of the epidermis is ulcerated and covered with a crust (green arrow). On either side of the ulceration, there are tumor nodules (red arrows) and nodulocystic tumor masses (black arrow). On the histology images, there are artefactual fractures within the tumor masses. In squamous cell carcinoma (SCC), the infiltration of tumor cells into the dermis leads to a loss of the dark line representing the dermo-epidermal junction. In figure 7.3, and 7.4 the OCT image and its corresponding histology image for an BCC and SCC sample are shown. Respectively. Keratinous pearls within SCC are shown with yellow arrows in both OCT and corresponding histology image. In the histology image of SCC sample, the green arrow labels a keratinous pearl lost during tissue processing. There is a proliferation of keratinocytes in the epidermis pushing into the dermis (red arrow). Keratinocytes in the epidermis show atypia (purple arrow) with large nuclei.

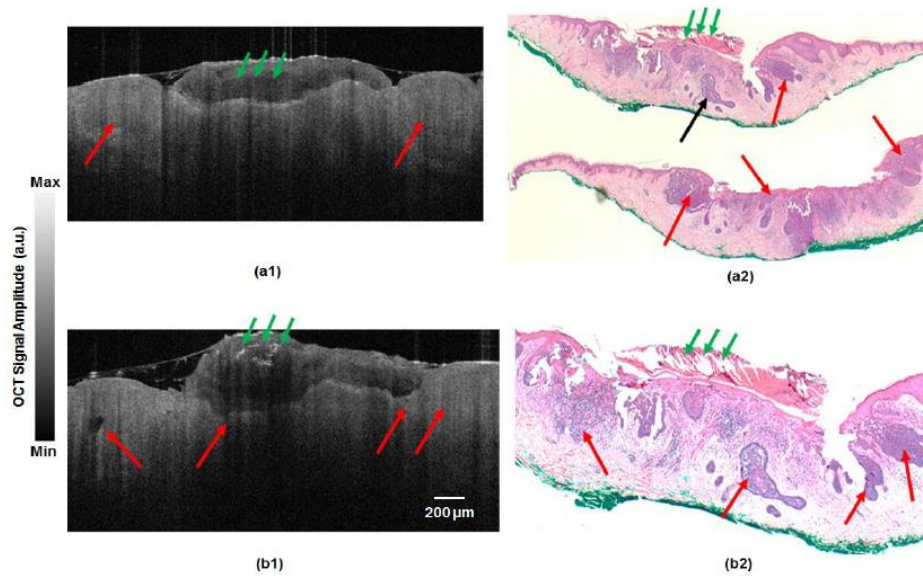


Figure 7. 3 (a1-a2) Image of OCT B-scan and (b1-b2) its corresponding histological image of a BCC sample of a 62 year old female

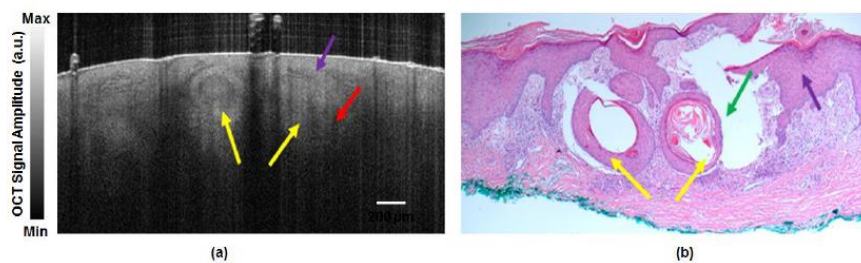


Figure 7. 4 Image of OCT B-scan (a) and its corresponding histological image (b) of an SCC sample of a 51 years old female.

7.3.3. Healthy skin analysis

17000 OCT healthy skin images taken from 100 body sites are used for computational modelling. Optical, statistical, and textural features are extracted from both layers of epidermis and dermis. The value of these features varies between skin of different sites due to the composition and arrangement of cells and organelles. A T-test and a PCA method is used to

measure the inter-correlation of such features. Regarding Optical features, attenuation coefficient is determined based on the OCT intensity decay. Attenuation coefficient has been computed for the skin of different sites using the single scattering algorithm [189].

In Figure 7.5(a) and figure 7.5(b), the attenuation coefficients of dermis and epidermis, respectively are calculated for pre-auricular, thumb, neck, outer arm, outer leg, nose, palm of hand, back, inner arm, and sole of ten healthy individuals whose age are between 25 to 56. The attenuation coefficient is significantly different between the group of sole, palm and thumb compared to the other sites of body (p -value < 0.05) in both dermis and epidermis.

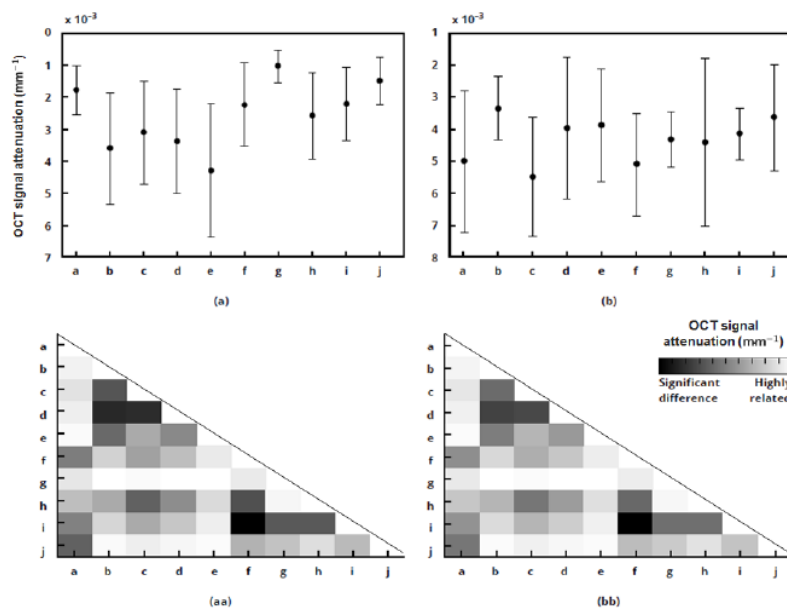


Figure 7. 5 Signal attenuation rate calculated for (a) epidermis, and (b) dermis, of ten body sites; Calculated p values (p -value < 0.05 considered as significant difference) for OCT signal attenuation of (aa) epidermis and (bb) dermis. The letters from a-j demonstrate the following; a: Neck, b: Preauricular, c: Tip of Nose, d: Back, e: volar forearm, f: Dorsal forearm, g: Palm of hand, h: Calf, i: Thumb pad, j: Sole

Moreover, it is observed that the palm and thumb are closely correlated in terms of attenuation coefficient and some of textural features, i.e., homogeneity. A considerable variance is also observed between preauricular and other sites observed for both dermis and epidermis. For the dermal layer, differences are detected between the sole and nose as well

as between the sole and arm. Figure 7.4 (aa) and (bb) respectively show the map of p -values for epidermis and dermis of different body sites.

First order statistical features (FOS) extracted from OCT images are mean, standard deviation, variance, skewness, kurtosis, median and entropy. A moderate difference between the FOS features extracted from epidermis and dermis layers is observed in all skin sites.

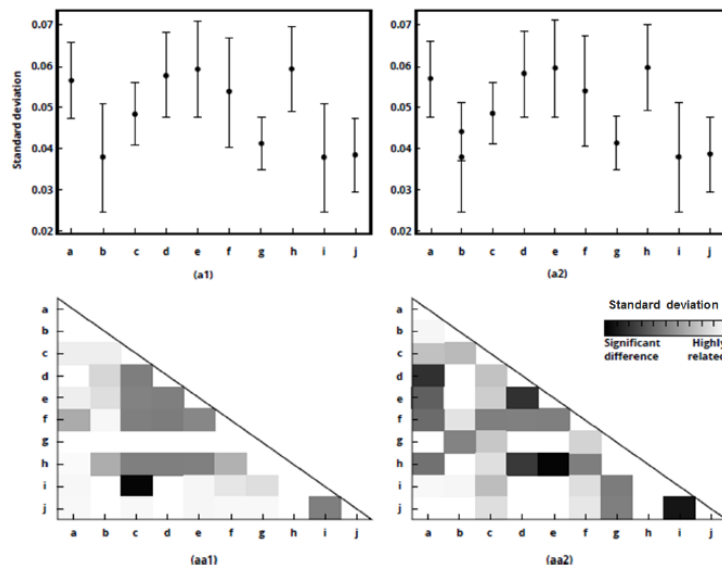


Figure 7. 6 First order statistical analysis, standard deviation, results and comparison for both epidermis and dermis Standard deviation for epidermis (a1), and for dermis (a2), of ten body sites; Calculated p values (p -value < 0.05 considered as significant difference), for the standard deviation of epidermis (aa1), and dermis (aa2). The letters from a-j demonstrate the following; a: Neck, b: Prearcular, c: Tip of Nose, d: Back, e: volar forearm, f: Dorsal forearm, g: Palm of hand, h: Calf, i: Thumb pad, j: Sole

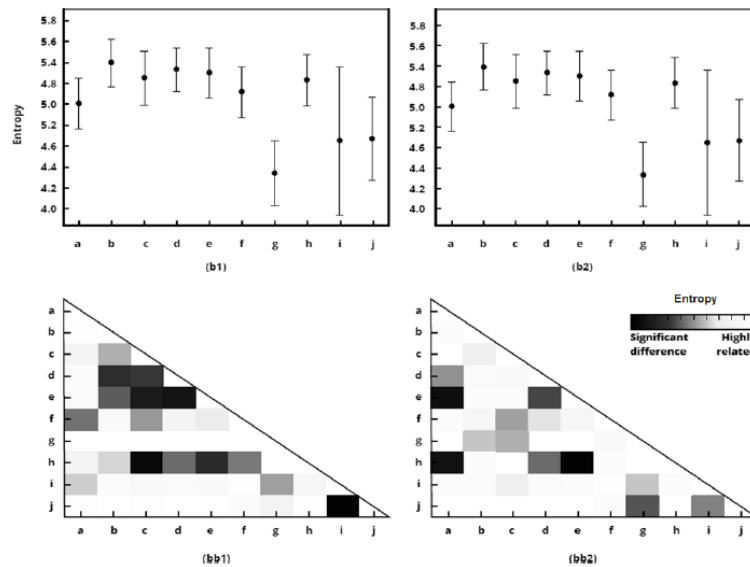


Figure 7. 7 First order statistical analysis, entropy, results and comparison of entropy for epidermis (b1), and dermis (b2), at ten body sites. Calculated P values (P -values < 0.05 considered as significant difference), for the standard deviation of epidermis (bb1), and dermis (bb2). The letters from a-j demonstrate the following; a: Neck, b: Prearicular, c: Tip of Nose, d: Back, e: volar forearm, f: Dorsal forearm, g: Palm of hand, h: Calf, i: Thumb pad, j: Sole

Figure 7.5 (a1) and 7.6 (b1) show the graphical chart of standard deviation and entropy values calculated for epidermis. The variation of FOS values for dermis is given in Figure 7.5 (a2) and 7.6 (b2). Maps of difference between each pair of skin sites, p -values, are given in figures 7.5 (aa1) and (aa2), figure 7.6 (bb1), and (bb2). The results show that FOS features have the same trend as the signal decay but also provides a more significant differentiation for both epidermis and dermis. It was also noted that nose and prearicular skins have very similar texture in epidermis layer. Textural features, i.e., contrast, energy, correlation, homogeneity and entropy in four directions, GLCM textures, are computed in all skin sites. The GLCM values of contrast and only entropy at 45 degree for epidermis are illustrated in figure 7.7 (c1) and figure 7.8 (d1), respectively, and that for dermis shown in figure 7.7 (c2) and figure 7.8 (d2). The p -values computed for the features are given in figure 7.8 (cc1) and figure 7.9 (dd1) for epidermis and 7.7 (cc1) and figure 7.8 (dd1) for dermis respectively. Our findings showed that there is a significant difference ($p < 0.05$) between the textural features

of different body sites taken from thick and thin skins in majority of cases, not in all cases, e.g., GLCM correlation (0 degree). The p -values computed for GRLM features in both epidermis and dermis, have a moderate difference between different sites.

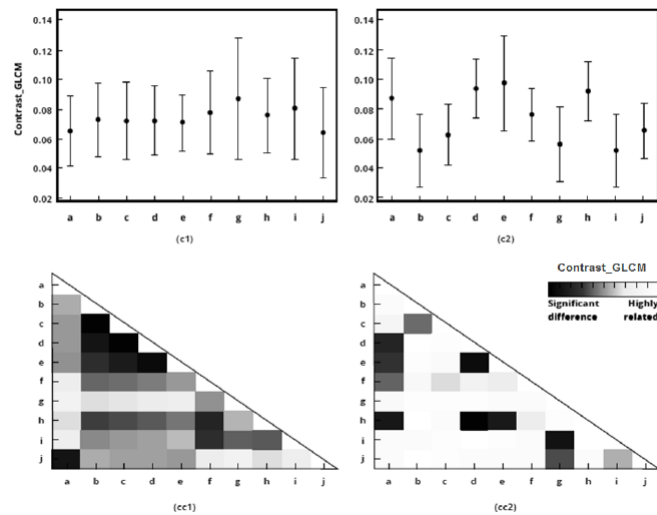


Figure 7. 8 GLCM texture analysis results and comparison of Contrast for epidermis (c1), and dermis (c2), at ten body sites of; Calculated P values (P-values < 0.05 considered as significant difference), for the standard deviation of epidermis (cc1), and dermis (cc2). The letters from a-j demonstrate the following; a: Neck, b: Preauricular, c: Tip of Nose, d: Back, e: volar forearm, f: Dorsal forearm, g: Palm of hand, h: Calf, i: Thumb pad, j: Sole

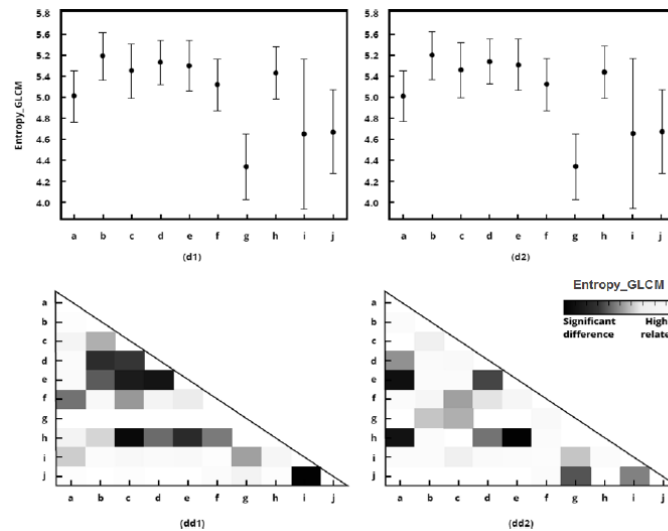


Figure 7.9 GLCM texture analysis, entropy at 45o, results and comparison. Entropy at 45o for epidermis (d1), and dermis (d2), of ten body sites; Calculated P values (P-values < 0.05 considered as significant difference), for the standard deviation of epidermis (dd1), and dermis (dd2). The letters from a-j demonstrate the following; a: Neck, b: Prearicular, c: Tip of Nose, d: Back, e: volar forearm, f: Dorsal forearm, g: Palm of hand, h: Calf, i: Thumb pad, j: Sole

7.3.4 Diseased skin; classification results

Several machine learning classifiers including SVM with two different kernels: Linear and 2nd polynomial (Quadratic), Logistic Regression, K-Nearest Neighbor classifiers, Linear discriminant analysis (LDA) and Artificial Neural Network (ANN) are tested for solving the classification problem using 10-fold cross validation. Quadratic SVM yielded the optimum result with an accuracy rate of $80.5 \pm 0.5\%$ for BCC classification and 87.2% for SCC classifications. Linear SVM in some cases also provided satisfying results, e.g., 80.9% for BCC classification. Figure 7.10 (a) depicts the dependency between each two pair of features in the 63-feature pool. A noticeable correlation is observed among the features from the same category, i.e., statistical, GLCM, and GRLM. In Figure 7.10 (c), the receiver operating characteristic (ROC) curve for several subsets of features with Quadratic SVM as classifier are shown. The most consistent results are obtained when entropy from FOS, entropy and correlation 0 degree, correlation and Homogeneity at 135 degree from GLCM and one

optical feature are used. These features are almost orthogonal. Figure 5d shows the cross-validation classification error percentage of five selected classifiers when different subsets of features are used. The results show that the lowest error is obtained when quadrature SVM with the six features is used. The results pertaining to differentiating BCC from healthy skin as well as SCC from healthy skin and BCC from SCC are shown in figure 7.10 and 7.11, respectively.

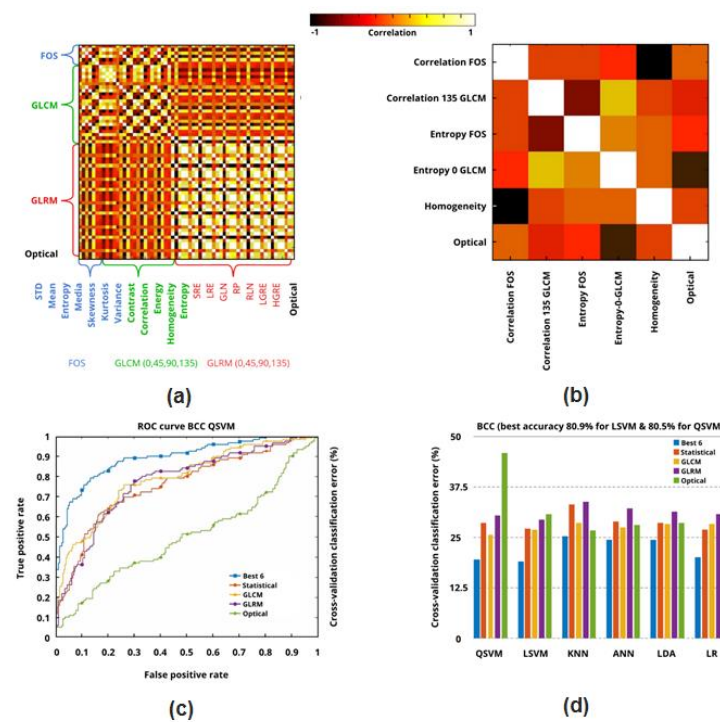


Figure 7. 10 Classification results. (a) Correlation map of 63 features used for differentiating healthy versus BCC samples, (b) correlation map of the six selected features, (c) ROC curve for different subsets of features with quadratic SVM classifier, (d) cross-validation classification error of different classifiers when different subsets of features were use

For BCC vs healthy, figure 7.10 (a) depicts the correlation between the 63 features. Brighter colors show more correlation. A noticeable correlation is observed among the features from the same category. Figure 7.10 (b) illustrates the reduction of the correlation among the six selected features. As it can be seen, there is less or no correlation between the features finally selected for the classification task. Figure 7.10 (c) shows the ROC curve

for different subset of features with quadratic SVM as classifier. Figure 7.10 (d) shows the cross-validation classification error percentage of different classifiers using different subsets of features. The results show that the least error is obtained using quadrature SVM with the 6 selected features. Figure 7.11 shows all of those parameters for SCC samples vs healthy.

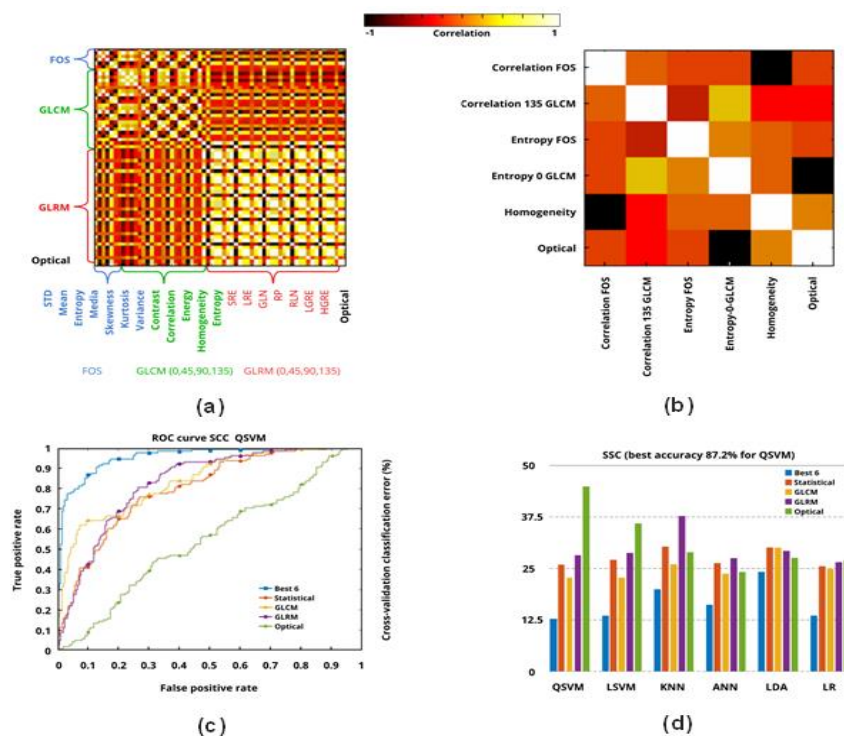


Figure 7. 11 Classification results. (a) Correlation map of 63 features used for differentiating healthy versus SCC samples, (b) correlation map of the six selected features, (c) ROC curve for different subset of features with quadratic SVM classifier, (d) cross-validation classification error of different classifiers when different subsets of features were used.

Correlation exists between the features finally selected for the final classification task. Figure 7.10 (c1) shows the ROC curve for different subset of features with Quadratic SVM as classifier. As it can be inferred the best result is obtained using the 6 best features. Figure 7.10 (d1) shows the cross-validation classification error percentage of different classifiers

using different subsets of features. The results show that the least error is obtained using Quadrature SVM with 6 selected features.

7.3.3 Imaging with other modalities

The principle of “the longer wave length offers deeper penetration, but always correlates with a lower resolution” is almost always true [30]. OCT has emerged as a modality that fills the gap between some other established imaging techniques in dermatology, i.e., dermoscopy, ultrasound, and confocal laser scanning microscopy. Dermoscopy offers an image of the skin surface with a large magnification, where diagnosis is based on specific patterns, depending on colors, differential structures, and asymmetry of the lesion [190] and it is widely used for the differentiation of melanocytic tumors in the clinic. High-frequency ultrasound is mainly used for the estimation of tumor thickness in melanoma to plan one-step excisions with guideline conform safety margins and helps to decide whether sentinel node excision should be performed at the same time [191]. Its penetration depth lies around 8 mm for the 20 MHz with a lower resolution than OCT. The confocal laser scanning microscopy offers the highest resolution comparable with histopathology (almost 1 μm), but at the expense of a limited penetration depth of only about 250 μm , allowing the evaluation of structures within the epidermis and down to the papillary dermis in great detail [180]. Currently high frequency ultrasound is widely used (most published work) in cutaneous imaging. Theoretically, some of high frequency ultrasound systems have a resolution close to that of OCT or even better. However, a more distinct structure in OCT images is observed. In the skin of the same body sites are imaged with other imaging modalities, i.e., different types of OCT and ultrasound imaging systems. These images are shown in figures 7.10 to 7.13, and their histology images given in Supplementary figure 7.14. The speckle size in OCT and ultrasound images of a fabricated tissue-mimicking phantom are compared and listed in Table 7.1 for comparison. The modalities used are as follows: SSOCT, clinical ultrasound, high frequency (HF) ultrasound (48MHz), ultra-high frequency (UHF) ultrasound (70 MHz) and HD OCT. The phantom is composed of TiO₂ and polyurethane. Average speckle size is estimated by using the full width at half maximum (FWHM) of the auto-covariance function of the speckle pattern [192]. In Table 1, I also compared the resolution, field of view and penetration depth of these imaging modalities. Comparing the results given in Table 1, OCT surpasses

other modalities in terms of speckle size. SS-OCT is the most favorable due to its moderate penetration depth, resolution, field of view, and speckle size.

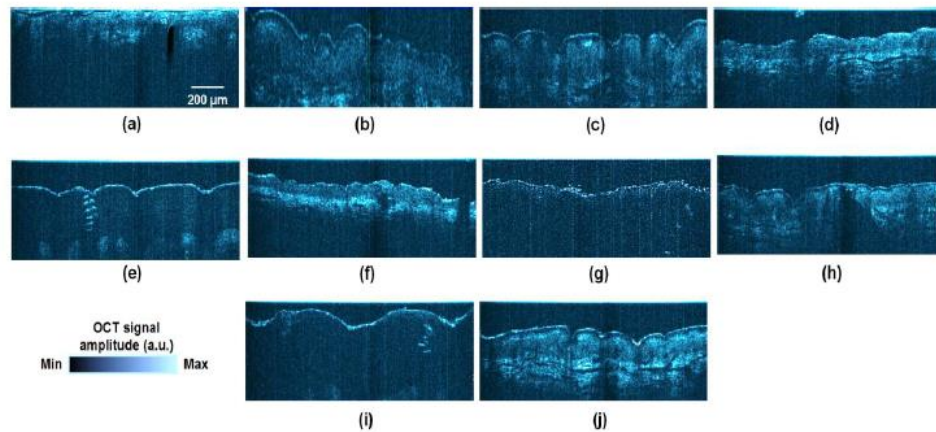


Figure 7. 12 HD OCT images of different sites of body including (a) Tip of nose, (b) preauricular, (c) volar forearm, (d) neck, (e) palm, (f) back, (g) thumb, (h) dorsal forearm, (i) sole, (j) calf

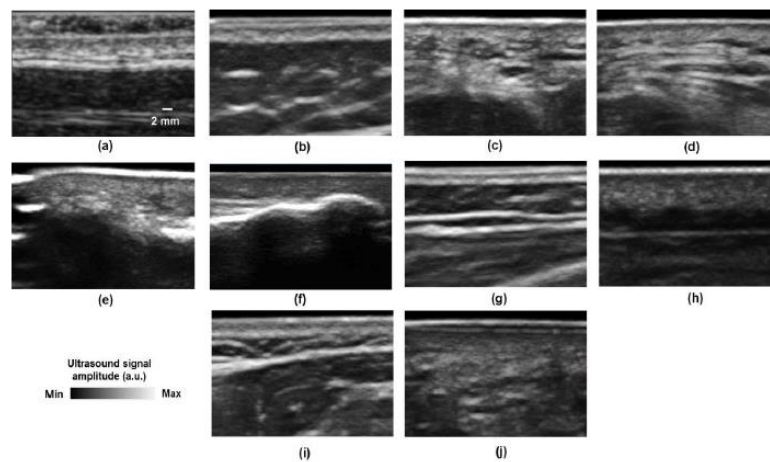


Figure 7. 13 Images obtained from a 15 MHz clinical ultrasound machine from different sites of body including (a) Tip of nose, (b) preauricular, (c) volar forearm, (d) neck, (e) palm, (f) back, (g) thumb, (h) dorsal forearm, (i) sole, (j) calf

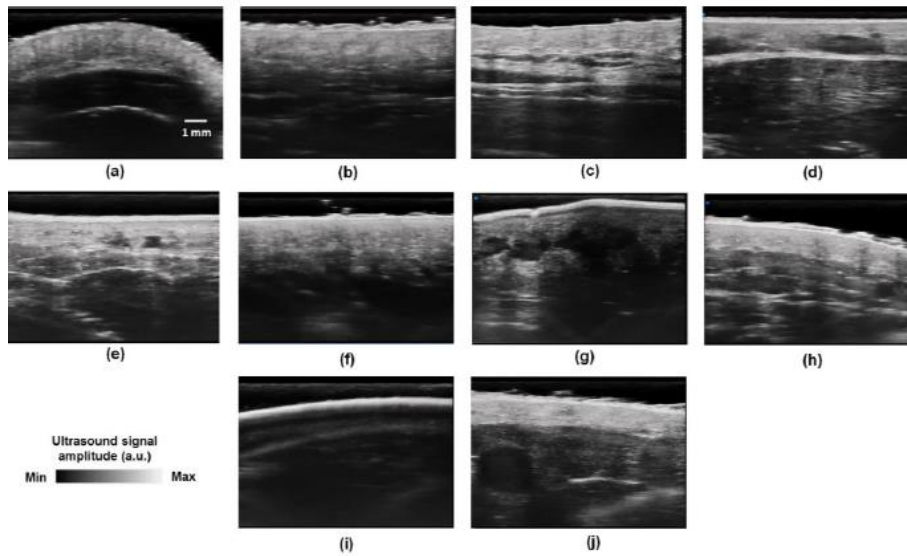


Figure 7. 14 Images obtained from a high frequency (VevoMD, 48 MHz) clinical ultrasound machine from different sites of body including (a) Tip of nose, (b) preauricular, (c) volar forearm, (d) neck, (e) palm, (f) back, (g) thumb, (h) dorsal forearm, (i) sole, (j) calf

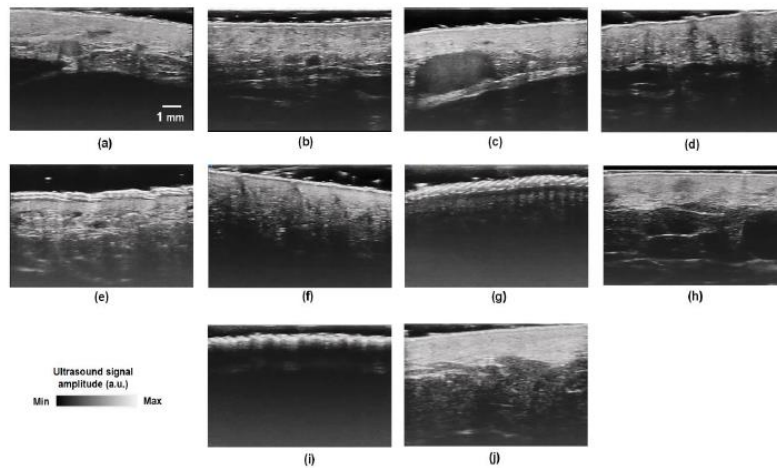


Figure 7. 15 Images obtained from a high frequency (VevoMD, 70 MHz) clinical ultrasound machine from different sites of body including (a) Tip of nose, (b) preauricular, (c) volar forearm, (d) neck, (e) palm, (f) back, (g) thumb, (h) dorsal forearm, (i) sole, (j) calf

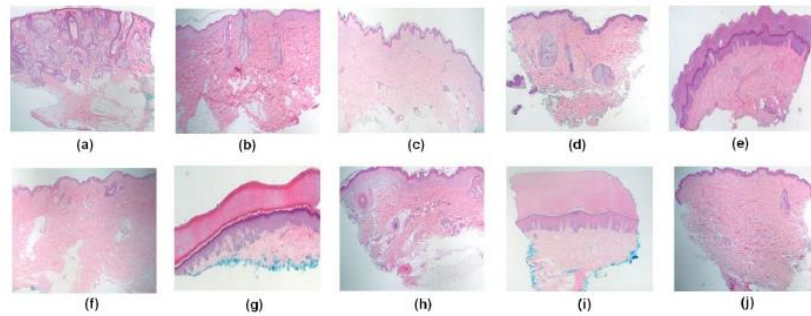


Figure 7.16 Healthy histology images of different sites of skin, (a) inner arm (b) palm of hand, (c) thumb pad (d) outer arm (e) neck (f) pre-auricular, (g) leg (h) Sole (i) Back (j) nose

Table 7.1 Specification of the imaging modalities used in this paper.

Imaging modality	Model	Axial resolution	Lateral resolution	Image size	Averaged speckle size for a phantom
SS-OCT	<u>Vivosight</u>	<u>7.5μm</u>	<u>10μm</u>	<u>6 mm \times 2 mm</u>	<u>22 μm</u>
HD OCT	Agfa skintell	3 μ m	3 μ m	1.8 mm \times 1.5 mm	15 μ m
Clinical US	Sonoscape S9	0.1 mm	0.2mm	---	400 μ m
US_UHL	48UHF Vevo MD BW: 20-46 MHz	50 μ m	110 μ m	15.4 mm \times 23.5 mm	225 μ m
US_UHR	70UHF Vevo MD BW: 29-71 MHz	30 μ m	65 μ m	9.7 mm \times 10.0 mm	114 μ m

7.4 Discussion

OCT is an effective technology capable of diagnosing skin conditions including inflammatory diseases and non-melanoma skin cancer. This pilot study presents the incorporation of clinical and detailed quantitative assessment of OCT images to first generate a comprehensive morphological and computational atlas of normal human skin *in-vivo*. The reference system of *in-vivo* healthy human skin OCT images can then be used to assess a wide variety of skin disorders with the aim of potentially improving diagnosis and treatment. A generated a small-scale OCT atlas of human skin from sites which covers most variations of skin tissues throughout the body. Healthy skin from a variety of body sites and from different individuals are imaged. Nose, preauricular, neck, upper and lower extremities, palms, soles and back cover the variety of epidermal thicknesses across the body, according to the dermatology literature. Acquired OCT B-scan images are despeckled in a software developed in Matlab for better visualization. Speckle is generated whenever coherent radiation is scattered from a surface or subject, whose roughness or size is comparable to the wavelength of the radiation. The mechanism of speckle is due to the heterogeneity of cell structures. Interference between the scattered wavefronts generates random speckle patterns. Many factors affect speckle, including the optical properties of the tissue, and the size and temporal coherence of the light source [11]. Features including attenuation coefficients, textural, and statistical features are extracted from ten evenly distributed ROIs on the skin sites both in the epidermis and dermis. The average values and their corresponding 95% Confidence Interval (CI) across different skin sites are calculated. The findings of this study show that the derived parameters are measurably different for both the dermis and epidermis in healthy skin of different sites. These features are then used for the classification between healthy and abnormal skins such as BCC and SCC.

The epidermis and dermis vary in different anatomic areas. The epidermis is a thin layer consisting of epithelial cells with no vasculature. The dermis is thicker (a combination of reticular and papillary layers) and behaves as a turbid optical medium. Papillary dermis is comprised of blood vessels, nerve fibers, thin collagen and elastic fibers and other cells. The reticular dermis has thicker collagen fibers and elastic fibers. The epidermis of thin skin sites varies between 0.07 mm to 0.12 mm while the full thickness of dermis varies between 1 to 4 mm. The optical differences between

epidermis and sublayers of dermis due to the difference in cell structure and size allow differentiation of these layers in the OCT image. From the optical perspective, back- and forward- scattering and absorption are used to explain the information provided by OCT images [9]. Optical properties and hence the corresponding features in OCT images vary based on sizes, shapes, concentration and orientations of tissue microstructure, e.g., cell membranes and blood vessel walls act as reflectors and refractors. Melanin, which is predominately located in the basal cell layer of the epidermis, and hemoglobin located within capillaries and larger vessels are the main sources of absorption in skin. In texture analysis, the GLCM matrix attribute 'contrast' (spatial frequency), is a measure for texture analysis, showing the difference between the highest and lowest intensity values of a set of pixels. This parameter is significantly different between the values calculated from palm/sole and nose. The GLCM matrix attribute 'energy' is a measure of uniformity of pixel pair recurrences and identifies disorders in textures. High-energy values occur when gray level distribution has a constant or periodic form. Significant variations of energy are measured in sole samples as compared to all other sites for both the epidermis and dermis. In the case of the GLCM matrix attribute 'entropy', an identifier of disorder or complexity of an image, it is large when the image is not texturally uniform. Sole, palm and thumb showed a significant difference in entropy when compared to that in other sites in both epidermis and dermis. The GLCM matrix attribute 'inverse difference moment' or 'homogeneity', in spite of having dissimilarity did not offer a significant distinction among different sites. With the OCT intensity-based information I extracted from B-scans, a classification technique is successfully developed that can differentiate between healthy and microstructural dermal abnormalities. Among the classifiers that examined, QSVM offers the best accuracy to differentiate between normal and abnormal tissue samples. This objectively determined information allows clinicians to diagnose, develop treatment plans, and determine individual prognoses more accurately.

7.5 Conclusion

To sum up, the optical, textural, and statistical properties are extracted from OCT skin images for dynamic modeling to create a perceptual atlas of the normal skin at different anatomic sites. I observed that skin cellular

architecture varies across the body, and so do the textural and morphological characteristics in the OCT images. There is, therefore, a critical need to systematically analyze OCT images of different sites and identify their significant qualitative and quantitative differences. Future directions for research could include continued analysis of the qualitative and quantitative differences on OCT images from even more sites. It is demonstrated that the dynamic model in conjunction with decision-theoretic approaches can assist in diagnosis of different microstructural dermal abnormalities, i.e., BCC vs. healthy, SCC vs. healthy, BCC vs. SCC, and hence aid in the determination of treatment. The result of this study can be extended as an interactive machine learning kernel interface addable to OCT devices. All of the described parameters can be used to create a more comprehensive analysis, with the aim of providing a more complete, objective, framework to categorize tissue properties for clinical use.

Section II

Chapter 8

Diagnostic applications of electromagnetic Scattering

8.1 Electromagnetic Wire-grid modelling of objects as a computational effective means

8.1.1 Introduction

This work focuses on the electromagnetic wire-grid modelling of cylindrical objects in a host medium. In this view, the sought targets often are long and thin: in these cases, two-dimensional methods can be employed to model the scenario and solve the electromagnetic scattering problem. Wire-grid modelling of conducting objects was introduced by Richmond in 1966 [193] and, since then, the method has been extensively used over the years to simulate arbitrarily-shaped objects and compute radiation patterns of antennas, as well as the electromagnetic field scattered by targets. For any wire-grid model, a better accuracy can be achieved with a larger number of wires; moreover, a fundamental question is the choice of the optimum wire radius and grid spacing. The most widely used criterion to fix the wire size is the so-called equal-area rule (EAR) [194]: the total surface area of the wires has to be equal to the surface area of the object being modelled. This rule comes from empirical observation and few authors have investigated its reliability for 2D objects through the years. Ludwig [194] studied the reliability of the rule by examining the canonical radiation problem of a transverse magnetic field by a circular cylinder in a vacuum, fed with a uniform surface current and compared with a wire-grid model; he concluded that the EAR is optimum and that too thin wires are just as bad as too thick ones. Paknys [195] investigated the accuracy of the rule for the modelling of a circular cylinder in a vacuum with a uniform current on it, continuing the study initiated in [194] or illuminated by a transverse magnetic monochromatic plane wave; he confirmed that the EAR is optimum and observed that the field inside the cylinder is most sensitive to the wire radius than the field outside the object. In [196], a circular cylinder was considered, embedded in a dielectric half-space and illuminated by a transverse magnetic monochromatic plane wave; the

scattered near field was calculated by using the Cylindrical-Wave Approach (CWA) [197] and numerical results, obtained for different wire-grid models in the spectral domain, are compared with the exact solution; it was shown that more accurate results can be obtained with a wire radius shorter than what is suggested by the rule. More recently, both the acoustic and electromagnetic scattering problems by a periodic configuration of N wires distributed on a ring, modelling a circular cage, are studied [198]; it was demonstrated that, as N goes to ∞ , the solution of the limiting problem is approached very slowly, as $N-1 \log N$.

Details concerning the implementation of the models and their simulation are provided in next sections, whereas numerical results are presented in Section 3. In particular, the reliability of the EAR is checked and guidelines for wire-grid sizing are extracted: this works analysis is in agreement with [196] despite a different scattering method is used here, a more realistic illumination is considered, and different shapes of the modelled object are simulated. This works also deals with the wire-grid modelling of objects partially embedded in a multilayered medium or structure; this is not an easy task, whereas being of great interest.

8.1.2 Finite Difference Time Domain Modelling of cylindrical objects

Several methods can be employed, to solve electromagnetic forward-scattering problems. One of the most versatile approaches is the well-known FDTD technique [199], based on a spatial and temporal discretization of Maxwell's curl equations in differential form, commonly within a rectilinear Cartesian grid as originally proposed by Yee [200] in 1966. YEE cell algorithm based FDTD numerical method employs the following parameters and procedures to perform the simulation:

Algorithm 8.1 FDTD

- General parameters of the simulation;
 - X-Y matrices based on the grid points of the computational domain $\Delta_x \geq \lambda/10$
 - Courant criteria for minimum time-step
 - Scaling factor ; Courant number $S_c = c\Delta_t/\Delta_x$
 - Dielectric property of the media
- Definition of the YEE-Grid based on E and H are shifted in space by half of the Δ_x
- Interpolation of the electrical properties profile onto the Yee grid

- Boundary conditions initialization (PML)
- Numerical partial derivate of E and H and updating loop

$$E_x^{n+\frac{1}{2}}(k) = E_x^{n-\frac{1}{2}}(k) + \frac{1}{\sqrt{\mu_0 \epsilon_0}} \frac{\Delta t}{\Delta z} \left(H_y^n \left(k - \frac{1}{2} \right) - H_y^n \left(k + \frac{1}{2} \right) \right) \quad (8.1)$$

$$H_y^{n+1}(k + 1/2) = H_y^n(k + 1/2) + \frac{1}{\sqrt{\mu_0 \epsilon_0}} \frac{\Delta t}{\Delta z} \left(E_x^{n+1/2}(k) - E_x^{n+1/2}(k + 1) \right) \quad (8.2)$$

- Source Excitation
- Visualization of the calculated field values after choosing time step

In the simulations, the physical structure of the transmitter and receiver is not included in the model: the source is represented through a line of current, as a consequence of the assumption of the invariance of the problem in one direction, and the electric field impinging on the receiver is calculated. A first derivative of Gaussian pulse is emitted by the source, with 1 GHz center frequency. All the involved media are assumed to be linear and isotropic, possibly lossy, and their constitutive parameters do not vary with frequency; metallic objects are assumed to be perfectly-conducting. In order to keep the errors associated with numerical-induced dispersion at a minimum, the spatial discretization step is always at least ten times smaller than the smallest wavelength of the propagating electromagnetic fields; the highest frequency to be taken into account in the simulations is estimated as three times the center frequency of the pulse. To limit the effects of staircase approximation of continuous objects, circular cylinders are modeled by discretizing their radius through at least twenty cells. Another crucial point in the FDTD approach is the approximation to be made in order to limit the computational space: to guarantee reliable results, I adopt Perfectly-Matched Layer boundaries as Absorbing Boundary Conditions, which are very effectively implemented in here; ten layers is used and put source and targets at least fifteen cells away from the most internal layer.

8.1.3 Accurate wire-grid modelling of objects in a host medium

A perfectly-conducting circular cylinder is considered, embedded in a dielectric half-space representing a soil, as sketched in figure 8.1(a). The source is positioned at the air-medium interface and the emitted electric field is parallel to the target axis. The relative permittivity of the medium is $\epsilon_r = 4$. The radius of the cylinder is $R = 50$ mm, its axis is in $x = 250$ mm,

$y = 100$ mm. A wire-grid model of the object is shown in figure 8.1(b): it consists of $N = 16$ circular-section cylinders with radius r , arranged in a uniformly-spaced circular array. The best position for the wires is with axes lying on the surface of the cylinder to be modeled [196]; with a larger N , the behavior of the array gets closer to that of the modelled object [197]

Our aim is to investigate the validity of the EAR. In our case, the rule imposes the condition $r = R/N = 3.125$ mm has to be satisfied. The good reliability of this criterion is apparent by the results shown in Figs. 1(c)-1(f). In particular, in Figures 8.1(c) and 8.1(d), the B-scans obtained for the circular cylinder and its wire-grid model are presented, respectively. In Figs. 8.1(e) and 8.1(f), electric-field maps calculated in $t = 2.2$ ns are shown, for the circular cylinder and its wire-grid model (being $t = 0$ the time instant in which the source starts to emit the pulse). Here and in the following, according to a nomenclature widely accepted by the GPR community, the term ‘A-scan’ refers to an array of electric-field values calculated in a fixed spatial point and in T consecutive instants; the term ‘B-scan’ corresponds to a matrix of electric-field values, calculated in T time instants and M different spatial points, meaning M A-scans (this is equivalent to assuming that a radar ‘stops’ in M positions, for example along a line parallel to the air-soil interface, gathering data in each of them; the B-scan is the comprehensive set of radar traces). The B-scans presented in figs. 8.1(c) and 8.1(d) are obtained by shifting the source in $M = 80$ positions equally-spaced along the air-soil interface; the electric field is calculated on the interface at a distance $d = 50$ mm from the source. Small differences can be appreciated, between the results relevant to the circular-section cylinder and its wire-grid model: mainly, the array of wires causes the presence of a higher number of minor reflections. The electric-field maps in Figs. 8.1(e) and 8.1(f) are calculated by putting the source is in $x = 240$ mm, $y = 250$ mm. They reveal that the internal field is much more sensitive to the modelling configuration than the external one, in good agreement with [6]. In fact, the field inside the array of wires is not vanishing in figure 8.1(f); this suggests that more wires should be employed, when shielding effects are concerned.

Despite the well-known rule of thumb yields good results, it can be verified that is far from being the optimum. In figure 8.2(a), results are shown for the same configuration as in Figure.8. 1(b), for various lengths of the wire radius, equal to, shorter, and longer than R / N . In particular, the absolute error on A-scans is plotted, defined as the magnitude of the difference between the exact A-scan (calculated in the presence of the circular

cylinder) and the A-scan obtained for the wire-grid model. The source is in $x = 240$ mm, $y = 250$ mm and the field is computed in $x = 250$ mm, $y = 250$ mm. With a wire radius, longer than the value suggested by the EAR, worse results are obtained.

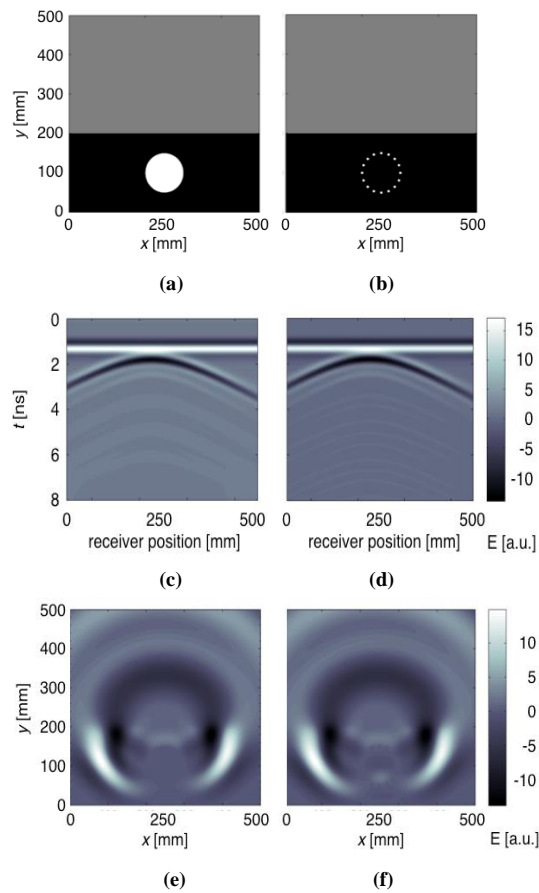


Figure 8. 1 (a-b) Geometry of the problem; (c-d) B-Scans and (e-f) electric-field maps for the circular section cylinder and its wire-grid model.

The lowest error is achieved when $r = 0.9R / N$. A refinement of this analysis is presented in figure 8.2(b): it can be noted that a shortening of about 12%, with respect to the well-known rule of thumb, gives the best results (the error is reduced of about one order of magnitude).

In figure 8. 3, the same as in figure 8.2 is reported, when $N = 32$. The error is slightly lower than when $N = 16$, as expected. The highest accuracy is achieved by shortening the radius of about 13%. Changing the radius of the

modelled object and keeping fixed the size of the wires, or varying the object burial depth, analogous results are obtained.

Moreover, I now investigate whether similar results are obtained for a buried object with a different shape. To this aim, I consider a perfectly-conducting square-section cylinder, embedded in a dielectric half-space, as sketched in figure 8.4(a). The relative permittivity of the soil is again $\epsilon_r = 4$. The side-length of the square is $L = 100 \text{ mm}$, the axis is in $x = 250 \text{ mm}$, $y = 100 \text{ mm}$. A wire-grid model of the object is shown in figure 8.4(b): it consists of an array of $N = 16$ circular-section cylinders, with a spacing equal to $0.25L$. To respect the EAR, the condition $r = 2L / N\pi \approx 3.979 \text{ mm}$ has to be satisfied.

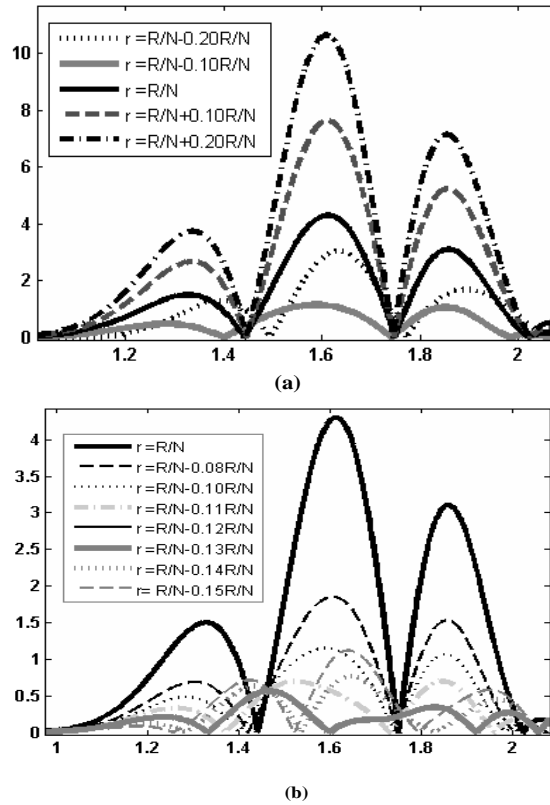


Figure 8. 2 (a) Absolute error on A-scans, with $N = 16$ and for various lengths of the wire radius; (b) refinement of the analysis presented in (a).

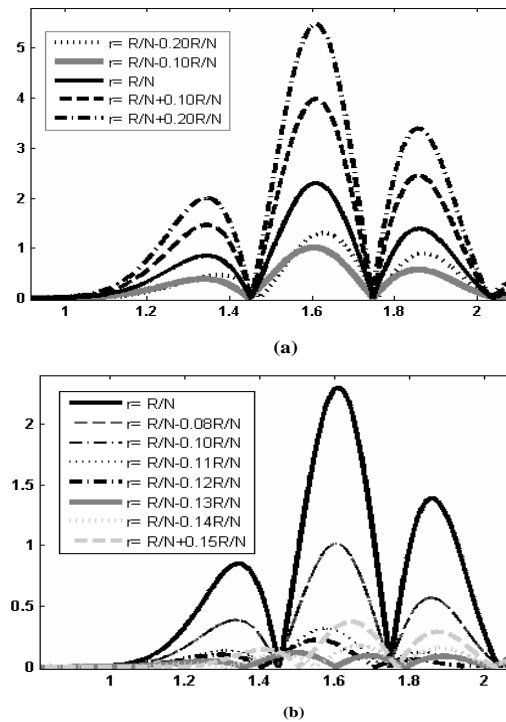


Figure 8.3 (a) Absolute error on A-scans, with $N = 32$ and for various lengths of the wire radius; (b) refinement of the analysis presented in (a).

In figures. 8.4(c) and 8.4(d), B-scans obtained for the square-section cylinder and its wire-grid model are presented, respectively. In Figs. 8.4(e) and (f), electric-field maps calculated in $t = 2.2$ ns are shown, for both the circular cylinder and its wire-grid model, when the source is in $x = 240$ mm, $y = 250$ mm. These results are in agreement with figure 8.1; similar comments apply. In figure 8.5, the absolute error on A-scans is shown. The source is in $x = 240$ mm, $y = 250$ mm, the field is computed in $x = 250$ mm, $y = 250$ mm. With a wire radius, longer than what was suggested by the EAR, worse results are obtained. A shortening of about 13-15%, instead, gives the best results.

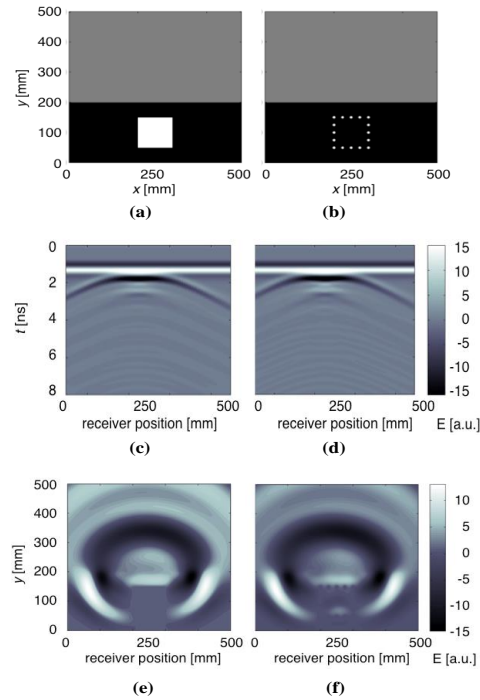


Figure. 8.4. (a-b) Geometry of the problem; (c-d) B-Scans; (e-f) electric-field maps for the square-section cylinder and its wire-grid model.

A general guideline for wire-sizing can be extracted, suggesting that the same-area criterion is affordable, but a higher accuracy can be achieved with wires smaller than what suggested by the rule. A shortening of about 12-15 % is recommended.

8.1.2 Objects partially hosted in different media

This sub-section deals with the simulation of objects partially buried in different media of a multilayered soil or structure. The considered scenario is depicted in figure 8.6(a): the upper half-space is a vacuum, the intermediate slab has a relative permittivity $\epsilon_{r1} = 4$ and is 300 mm thick, the lower half-space has a relative permittivity $\epsilon_{r2} = 15$. A perfectly-conducting circular cylinder is partially embedded in both the upper half-space and finite-thickness slab; the radius is $R_1 = 50$ mm and the axis

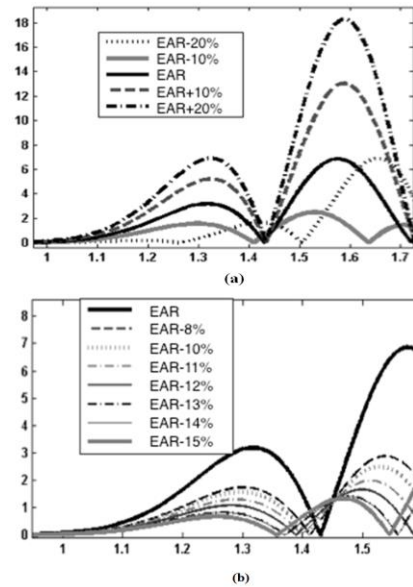


Figure 8.4 (a) Absolute error on A-scans, with $N = 16$ and for various lengths of the wire radius; (b) refinement of the analysis presented in (a).

is in $x = 250$ mm, $y = 780$ mm. A larger cylinder is embedded in both the slab and lower half-space; the radius is $R_2 = 100$ mm and the axis is in $x = 600$ mm, $y = 500$ mm. Both the cylinders are modeled by means of their equivalent wire-grid models, with $N = 16$; the wire radius is shortened of 13% with respect to the value suggested by the EAR. The B-scan presented

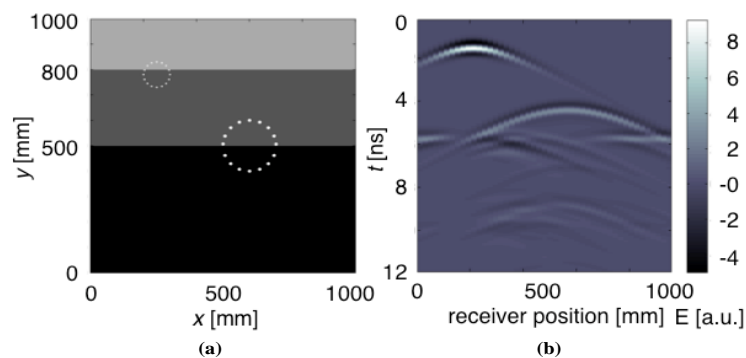


Figure 8.5 (a) Geometry of the scattering problem for two partially buried cylinders, modelled with the wire-grid approach; (b) B-Scan.

in figure 8.6 (c) is obtained by shifting the source in $M = 50$ positions along a line parallel to the vacuum- slab interfacin $y = 90$ mm; the electric field is calculated on the same line at a distance $d = 10$ mm from the source. The aim of this example is just to remind and underline an interesting application of the wire-grid modelling: it allows to simulate partially-buried objects by using methods that cannot deal with geometries involving overlapping sub-domains, as the CWA.

8.1.5 Arbitrary shaped objects

This sub-section deals with wire-grid modelling of slotted objects. In Figure 8.7(a), the geometry of a perfectly-conducting slotted cylinder is shown: its radius is $R = 50$ mm, the axis is in $x = 250$ mm, $y = 250$ mm, the slot-length is $\pi R/4$, and the object is 2 mm thick. Figures. 8.7 (b) shows a wire-grid model of the object. The relative permittivity of the hosting half-space is $\epsilon_r = 4$. In Figure 8.8, A-scans calculated in $x = 250$ mm, $y = 450$ mm are presented, for different values of N ; the exact curve is reported as reference. It can be noticed that the wire-grid models follow

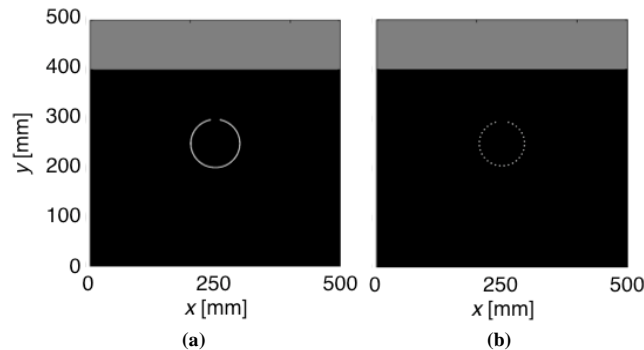


Figure 8. 6 (a) Geometry of the scattering problem for a slotted cylinder; (b) wire-grid model of (a), with 32 wires.

the exact curve quite well for the first two reflections. However, the wire-grid reflections are delayed with respect to the exact ones, as if the slot was larger. The delay slightly reduces a larger N , for example the first reflection is delayed of 85, 75 and 70 ps when $N = 16, 32$ and 64 , respectively.

We noticed that wire-grid results are much closer to exact results when the slot is longer. Moreover, we observed that in the presence of a short slot, as in figure 8.7, the results are not much affected from the thickness of the

object; for longer slots, instead, the thickness of the object has a stronger influence on the results and – in the wire-grid approach - more accurate results can be obtained by using two concentric arrays, simulating both the inner and outer circle arcs of the object section.

This is an interesting topic that needs to be studied more in depth, in order to evaluate to what extent, the wire-grid approach can be used for the modelling of slotted objects, and to extract simulation guidelines for this kind of geometries.

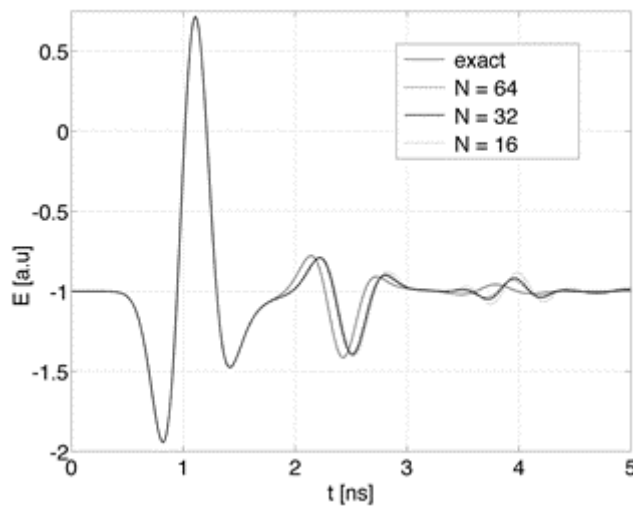


Figure 8. 7 A-scan for the slotted cylinder and its wire-grid model.

8.2 Spectral representation of EM scattering from the objects in host medium

A two-dimensional scattering problem of a line source by a set of PEC and dielectric cylinders buried in a semi-infinite medium by means of Cylindrical-Wave Approach (CWA) is solved in [201]. In this section, a Finite Difference Time Domain (FDTD) based algorithm is developed for cylindrical objects in a host medium and its results are compared with CWA approach.

8.2.1 Methods

The 2 dimensional FDTD modeling scheme is used to model the buried target and simulate the backscattered wave response scattered. The stability method considered and a ten cell thick perfectly matched layer (PML) is used for neglecting boundary reflections concerns. One widely known used excitation field antenna in multi-layer analysis is the dipole antenna. Modeling field with a point or a line source is a convincing hypothesis for such an antenna. The used excitation is a time varying Ricker wavelet source with 1 GHz center frequency which could be expressed as (8.3).

$$f_r(t) = (1 - 2\{\pi f_p[t - d_r]\}^2)e^{-\{\pi f_p[t-d_r]\}^2} \quad (8.3)$$

Which f_p is the peak frequency and d_r is temporal delay. The Fourier transform of (8.3) is given in (8.4).

$$F_r(\omega) = \frac{2}{f_p\sqrt{\pi}} \left(\frac{\omega}{2\pi f_p}\right)^2 e^{-\left\{jd_r\omega + \left(\frac{\omega}{2\pi f_p}\right)^2\right\}^2} \quad (8.4)$$

It appears delay only influences the phase of function. The form $f_r(t)$ and frequency spectrum $F_r(\omega)$ are of the wavelet are illustrated in figure 8.8. The plane-wave solution for construction of traveling Ricker wavelet could be given by $f_r(t \pm x/c)$ where c is speed of propagation and will be given by.

$$f_r[m, q] = \left(1 - 2\pi^2 \left[\frac{S_c q \pm m}{N_p} - M_d\right]^2\right) e^{-\pi^2 \left[\frac{S_c q \pm m}{N_p} - M_d\right]^2} \quad (8.5)$$

where S_c is $c \frac{\Delta_t}{\Delta_x}$, q and m are the temporal and spatial indices respectively.

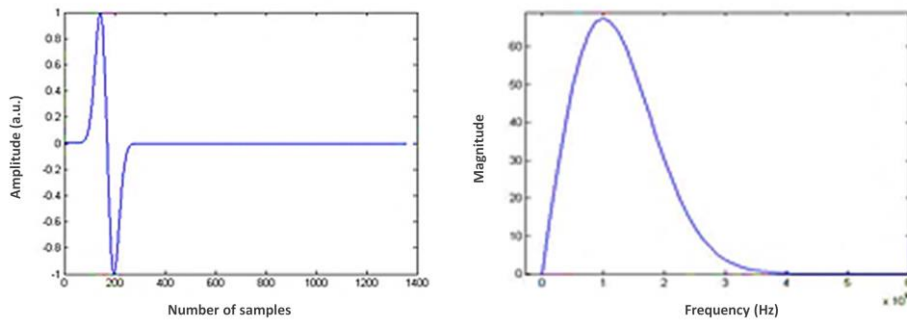


Figure 8. 8 Excitation Ricker wavelet source and its frequency spectrum

In order to generate scattered transmitted field, the scheme is utilized to calculate EM wave propagation and recorded for each receiver position. The time-dependent numerical scattered electric field is recorded. This is then transformed into the frequency domain and the values for the selected working frequency are picked for use in spectral representation. Importance should be given to transformed indices and their exact frequency set. According to the Nyquist theorem, the maximum frequency is the inverse of two times the time sampling period. Involving the total number of samples or number of steps in the FDTD simulation named N_T , the spectral resolution is given by

$$\Delta f = \frac{f_{max}}{N_T/2} = \frac{1}{N_T \Delta t} \quad (8.6)$$

The Radargrams illustrate the scattered field. It should be noted that to remove the air /ground wave, a background removal procedure is performed. The resulting scattered field is transformed into the frequency domain and the scattered field in spectral domain is produced.

8.2.2 Results

a. A cylindrical object in lossless medium:

Initially, the simulation and processing was done for a buried metallic cylinder with radius of $a = 47.7$ cm, centered in $x = 1.0$ m and $y = 37.74$ cm. The refractive index of the second medium is $n_1 = 2$. The line source transmitter is placed at $x = 1$ m and $y = 52.38$ cm height from interface and receiver measures the field in an accumulative manner in 95.4 cm from the interface. The selected frequency for source is 1GHz.

b. A cylindrical void in a lossless medium:

The simulation and processing was done for a free space void cylinder with $n_c = 1$, radius of $a = 4.77$ cm, centered in $x = 1$ m and $y = 37.74$ cm. The refractive index of the second medium is $n_1 = 2$. The line source transmitter is placed at $x = 0.5$ m and $y = 2.38$ cm height from interface and receiver measures the field in an accumulative manner with two different distance scenarios of 9.54 cm from the interface. The selected frequency for source is 1GHz.

c. Two metallic cylindrical cables in a dispersive lossy medium:

The simulation and processing was conducted for two PEC cylinders, radius of $a = b = 4$ cm, buried 10 cm deep, the refractive index of the second medium is $n_1 = 2$. The line source transmitter is placed at the $x = 1.5$ m 1.59 m height compared to previous scenarios relative to interface. Cylinders are spaced about 28 cm apart. In this case Ricker wavelet, central frequency is 600MHz. The used dispersion model for dispersive lossy media is Debye model based on the work of Frezza. et. al. [201] (see figure 8.8).

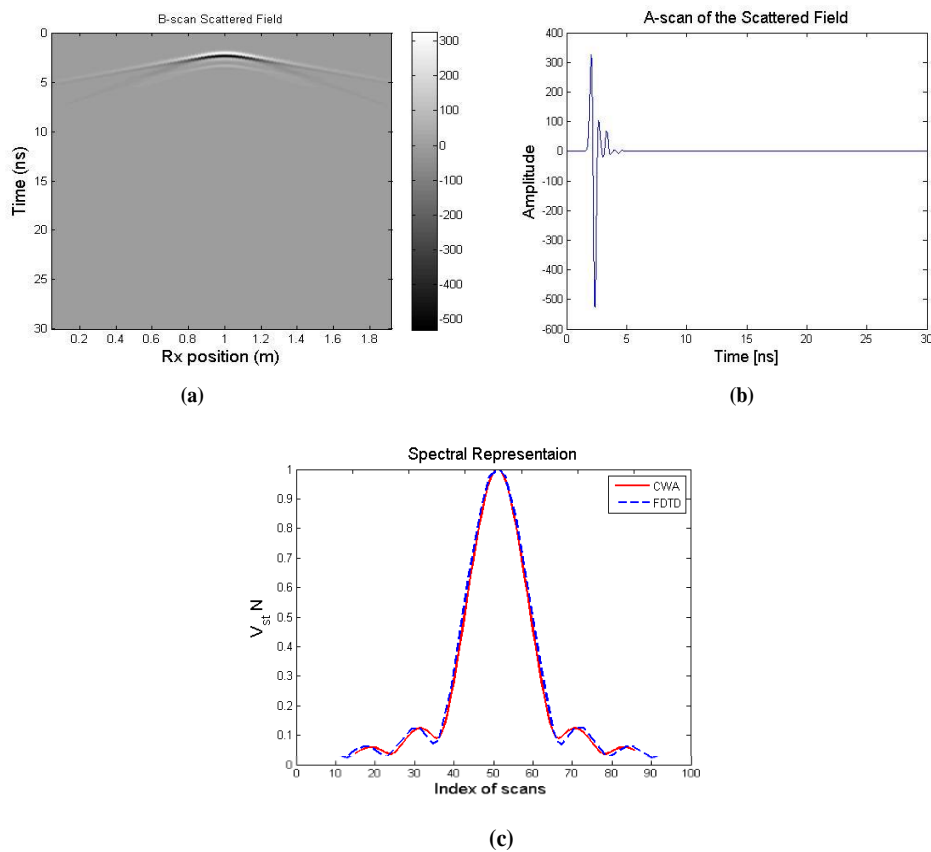


Figure 8. 9 Metallic (a) B-scan, (b) A-scan and field diagram (c) calculated near field for blue line proposed method and redline for CWA's work in [201].

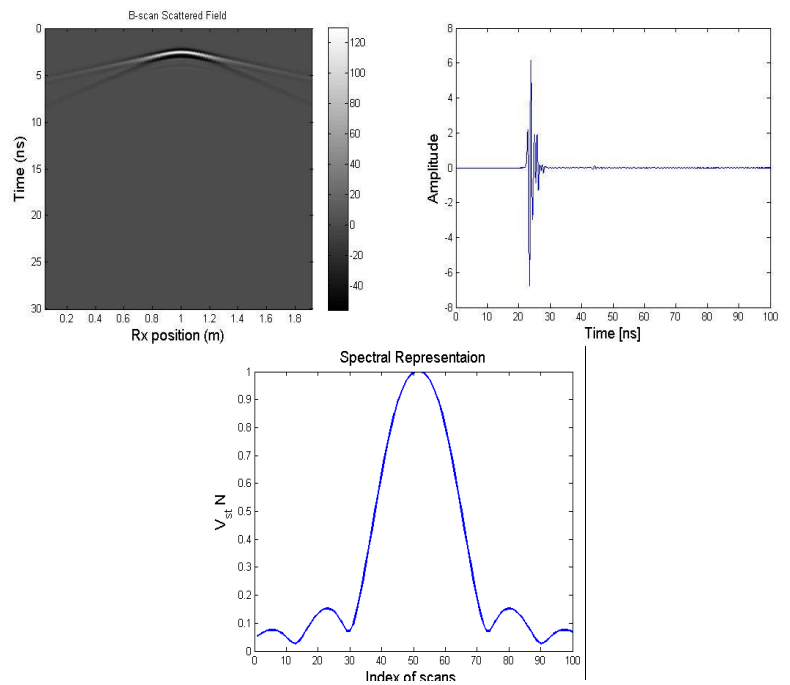


Figure 8. 10 Void (a) B-scan, (b)A-scan and field diagram (c) calculated field for blue line proposed method and redline for CWA Ponti.et al [203].

d. More complex scenario:

This implementation is performed for more complex scenarios referring to [203] with given geometry and materials and its scattered near field in figure 8.11.

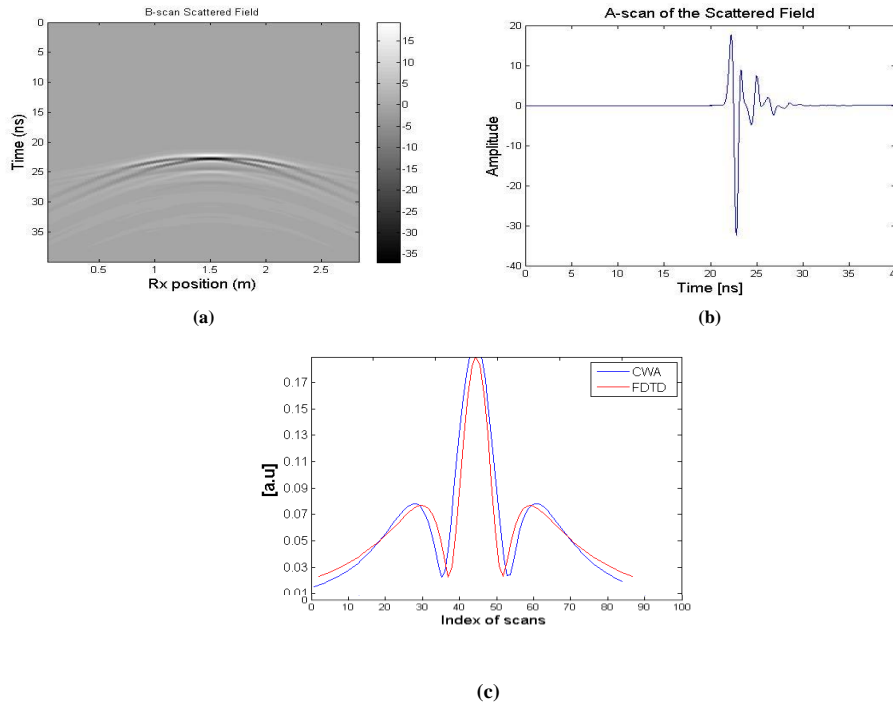
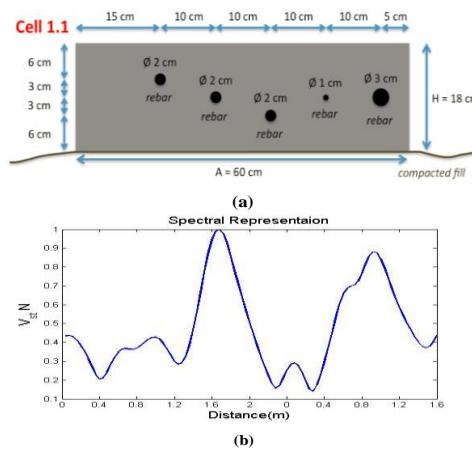


Figure 8. 11 Two metallic cables scattered near field (a) B-scan, (b)A-scan and field diagram (c) calculated field for blue line proposed method and redline for CWA Frezza. et.al [197].



(a) Geometry of problem,(b) its calculated FDTD based near filed

8.5 Conclusion

This chapter focused on the wire-grid modelling of buried cylindrical objects. Numerical results were obtained by using GprMax [201], a versatile tool implementing the Finite-Difference Time-Domain technique. The reliability of the well-known equal-area rule is investigated, showing that it yields affordable results but is quite far from being the optimum: higher accuracy can be achieved by using a wire radius 12-15% smaller than what is suggested by the rule. I considered circular- and square-section scatterers embedded in a half-space, in the presence of a line of current emitting an ultra-wide band pulse. The results are in good agreement with literature where wire-grid modelling of a circular-section cylinder illuminated by a monochromatic plane wave was studied and preliminary spectral-domain results were presented, calculated by using the Cylindrical-Wave Approach.

Subsequently, I considered the wire-grid modelling of objects partially buried in different layers of soil or structure. The aim of the reported example was to highlight that the wire-grid approach can significantly enhance the versatility variety of methods that can deal with scatterers embedded in a homogeneous material. Finally, I investigated the wire-grid modelling of circular-section slotted objects and presented preliminary results. For small slots, the wire-grid results follow quite well the main reflections of the exact results, but with some delay. More accurate results are obtained in the case of larger slots. To model thick objects with large slots, it is recommended to use two concentric arrays of wires, simulating both the inner and outer circle arcs of the scatterer section.

This analysis is of particular interest for the electromagnetic simulation of Ground Penetrating Radar scenarios. Future work can be modelling dielectric object to be used in electromagnetic simulation of biomedical scenarios. The second part of this chapter dealt with the spectral representation relevant to scattering from some utilities known objects in different media has been implemented. Comparisons with both results in the literature and simulations for them have been performed, obtaining a good agreement.

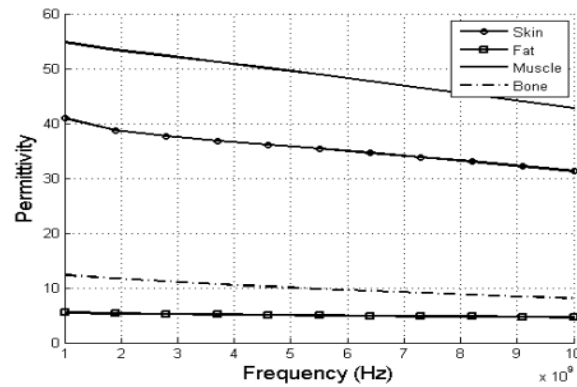
Chapter 9

Electromagnetic thickness formulation for human arm layers toward soft tissue assessment

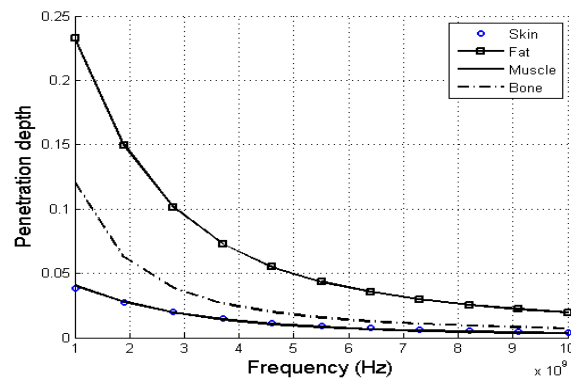
9.1 Introduction

Tracking upper limbs kinematics offers a beneficial description for assessment of daily activities. Techniques to monitor human activity system are classified into: (a) invasive bone-based motion recording techniques, and (b) non-invasive skin-based method [202]. One of the most challenging issues in such a recordings is soft tissue artifact (STA) [203]. STA is produced due to the displacement of skin-mounted markers on the soft tissue with respect to the underlying bones. The STA error needs to be effectively assessed and mitigated [203-205]. More recently, Non-invasive medical imaging modalities such as dynamic MRI [206] and ultrasound [207] in accordance of three dimensional Motion Capture data [202] are employed to quantify the dislocation of markers and to assess the STA. However, the viability of using an electromagnetic (EM) backscattered signal to evaluate the STA has not been reported in the literature. That encouraged me to explore bone localization using this technique toward STA correction in this study. The primary focus of using microwave radar-based techniques is in medical imaging for breast cancer detection [208, 209] and it is utilizing the contrast of electrical properties among under investigation tissues. The most recent advancement in Microwave Imaging of the musculoskeletal system is reported in [210] where the first clinical example of microwave images for the calcaneus was presented. They showed that microwave response monitoring could be a promising method for bone imaging. The key factor to modeling such systems are the electrical properties of biological tissues, that is comprehensively studied in [211, 212]. Gabreil's et.al showed human tissue's electrical properties are highly depends on water content. This means low water content tissues such as bone and fat tend to present low permittivity, whilst high water content tissues, such as muscle and blood have higher permittivity. The penetration depth for human tissues varies with operating frequency and is illustrated in figure 9.1. It should be noted that the backscattered signal

from stratified media depends on the variation in electrical properties of the consecutive materials [213].



(a)



(b)

Figure 9. 1 Permittivity and penetration depth of different tissue types at high frequencies (a) Permittivity and (b) Penetration depth

Relying on the Ground Penetrating Radar concept, an electromagnetic method based on the recording and analysis of the dielectric discontinuities in subsurface structures, the feasibility of using EM backscattered signal for bone localization is investigated theoretically and verified by simulation.

9.2 Electromagnetic response of the structure

In this study, an efficient, simple procedure to estimate the thickness of tissues are presented. To this end, the electromagnetic scattering field from a simplified, parameterized human arm tissue layer model is obtained analytically based on the microwave transmission line matrix method [214]. Then, it is verified through numerical Finite Difference Time Domain (FDTD) based simulation []. Moreover, time domain response of the structure is used to detect the reflection from each layer, retrieving the permittivity and estimation of tissues thicknesses.

9.2.1 Analytical model of human arm as a layered media

Considering a one-dimensional, flat multilayer structure of biological tissues consisting of skin, fat, muscle and bone with specified thicknesses and permittivity, a simplified human's upper arm is visualized. Geometry of the problem is given in figure 9.2. A Transverse Electromagnetic (TEM) plane-wave source is considered in the proximity and on top of human arm skin where electric and magnetic vectors are perpendicular to the direction of propagation. According to electromagnetic theory, if an EM wave meets an alternate medium, part of the wave is reflected from and the other part is transmitted through based on the constitutive parameters of the involved media. A schematic illustration of backscattering from the boundaries of TEM traveling [215] waves for the layered structure is shown in figure 9.2. The direction of travel is the z-axis and on the x- and y-axes each layer has the infinite extension.

Assuming the material is not magnetic, the intrinsic impedance and the propagation constant of each layer are given by (9.1) and (9.2)

$$\eta_i = \sqrt{\frac{1}{\epsilon_{ir}}} \quad (9.1)$$

$$\beta_i = j \frac{2\pi n_i l_i}{\lambda} = \frac{\omega}{c} \sqrt{\epsilon_{ir}} \quad (9.2)$$

Where $j^2 = -1$, ϵ_{ir} is the relative permittivity of each layer, λ is the operating wavelength in the free space, $n_i = \sqrt{\epsilon_{ir}}$ is the refractive index of each medium and l_i is the thickness of arm's layers. The Fresnel

reflection coefficient between two subsequent layers, Γ_i , is related to characteristic impedance of each layer η_i by (9.3)

$$\Gamma_i = \frac{\eta_i - \eta_{i-1}}{\eta_i + \eta_{i-1}} \quad (9.3)$$

$$\tau_{i,i-1} = \frac{2\eta_i}{\eta_i + \eta_{i-1}} \quad (9.4)$$

It should be noted that $\eta_0 = \sqrt{\frac{\mu_0}{\epsilon_0}}$ is the characteristic impedance of free space and it is equal to 377Ω . E_{i+} is the incident wave impinging each layer and E_{i-} is define as superposition of reflected and transmitted wave in each media which is given by (9.5)

$$E_{i-} = \Gamma_i E_{i+} + \tau_{i,i-1} E_{i+1-} \quad (9.5)$$

To relate the transmission and reflection coefficient to incident and reflected wave, the ABCD wave matrices [216] of the structure can be arranged and cascaded to (9.6).

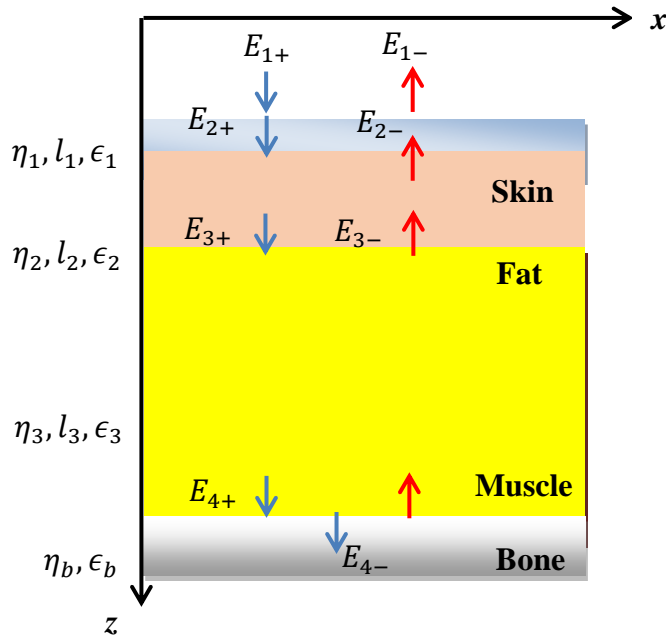


Figure 9. 2 A simplified one-dimensional geometric model of human arm

$$\begin{bmatrix} E_{1+} \\ E_{1-} \end{bmatrix} = \prod_{i=1}^4 \frac{1}{\tau_i} \begin{bmatrix} e^{\beta_i} & \Gamma_i e^{-\beta_i} \\ \Gamma_i e^{-\beta_i} & e^{-\beta_i} \end{bmatrix} \begin{bmatrix} E_{i+1+} \\ E_{i+1-} \end{bmatrix} \quad (9.6)$$

For the last infinite thickness layer, the backward travelling wave is zero. The total transmission coefficient and overall reflection response of this structure is given by (9.7) and (9.8) respectively.

$$\tau_T = E_{1_{i+1}}/E_{1+} \quad (9.7)$$

$$\Gamma_T = E_{1-}/E_{1+} \quad (9.8)$$

The reflection coefficient is frequency dependent. It is clear that the electric fields, and transmission and reflection coefficients are closely related to the thickness and electrical properties of the material.

9.3 Numerical verification

In this section, a comparison is performed among the introduced analytical model, the Finite Difference-based full-wave simulator, and CST microwave studio to verify the model. To make interpretation easier at this stage of the problem, the mentioned tissues are considered lossless, non-dispersive layers. The simplified human arm phantom consisting of skin with thickness of $l_1 = 2$ mm and relative permittivity of $\epsilon_{r1} = 36.78$, fat; $l_2 = 6$ mm, $\epsilon_{r2} = 5.12$, muscle; $l_3 = 35$ mm, $\epsilon_{r3} = 50.45$, and bone. The scattering response of the simulated model arm and its agreement with analytical model is given in figure 9.3.

9.4 Thickness estimation

9.4.1 Depth calculation formulation

To formulate the depth measurements of the structure, we use the time domain scattered signal technique inspired by [217, 218]work reported in where the signal amplitude and time delay information are used to calculate geometrical and physical properties of tissues. It assumes the time domain

signal is comprised of a superposition of scaled and lagged replicas of the incident pulse. Considering a non-magnetic structure, the thickness of each layer is given by (9.9) in an abstract form.

$$d_n = \frac{1}{2} v_p t_n = \frac{c t_n}{2\sqrt{\epsilon_{rn}}} \quad (9.9)$$

where v_p is the velocity of propagation in each layer, t_n is two-way travel time, c is the velocity of light, and ϵ_{rn} is relative permittivity of each layer. Therefore, to obtain the depth, the amplitude of reflection from each interface, and related time delays and permittivity of each layer should be calculated. Referring to the backscattered time signal that can be considered as a combination of received waveform from n layers, the permittivity for first layer is obtained by (9.10).

$$\epsilon_{r1} = \left(\frac{\eta_0}{\eta_1} \right)^2 \bigg|_{\eta_1 = \frac{\eta_0}{\frac{A_p - A_0}{A_p + A_0}}} = \left(\frac{A_p - A_0}{A_p + A_0} \right)^2 \quad (9.10)$$

where A_0 and A_p are the reflected amplitude from the top of surface layer and amplitude from a known reference layer, respectively. Similarly, for the next layers, the permittivity can be derived recursively whereas here the transmission between layers should be taken in to account. A generalized formula to obtain *in situ* permittivity of succeeding layers in a n -layer stratified structure based on what reported in [217] can be derived from (9.11).

$$\sqrt{\epsilon_{r,i}} = \sqrt{\epsilon_{r,i-1}} \frac{1 - \left(\frac{A_0}{A_m} \right)^2 + \sum_{i=0}^{n-1} r_i \frac{A_i}{A_m} + \left(\frac{A_{n-1}}{A_m} \right)}{1 - \left(\frac{A_0}{A_m} \right)^2 + \sum_{i=0}^{n-1} r_i \frac{A_i}{A_m} + \left(\frac{A_{n-1}}{A_m} \right)} \quad (9.11)$$

$$\text{Where } r_i = \frac{\sqrt{\epsilon_{ri}} - \sqrt{\epsilon_{ri-1}}}{\sqrt{\epsilon_{ri}} + \sqrt{\epsilon_{ri-1}}}.$$

A convenient method for this recursive calculation is defining a reference signal reserved from a single Perfect Electrical Conductor with certain thickness. The following algorithm uses for thickness estimation of soft tissues:

 Algorithm 9.1 thickness estimation

- (a) Obtain the synthesized time domain electromagnetic scattered signal from the modeled upper arm named $x_r(t)$ and its assigned time vector dt
- (b) Use an adaptive Hilbert envelope detector to detect local maxima of $x_r(t)$ and their related time delays reserved in t_i ; This step is interfaces detection
- (c) Acquire reference signal (PEC) and it related amplitude and time
- (d) Calculate the permittivity of each layer by (9.11)
- (e) Estimate the depth of each layer by (9.9)

9.5 Numerical results and algorithm assessment

Recalling, the mentioned procedure in algorithm 9.1 to calculate depth, figure 9.4 shows the transmitted (red) and time domain response of the structure (green). It is worth mentioning, in this study the signal is considered as superimposition of echoes of known pulse. An envelope detector is used for echo detection by estimating exact time of delay of echoes obtained from local maxim of defined filter evaluated within a pulse time window.

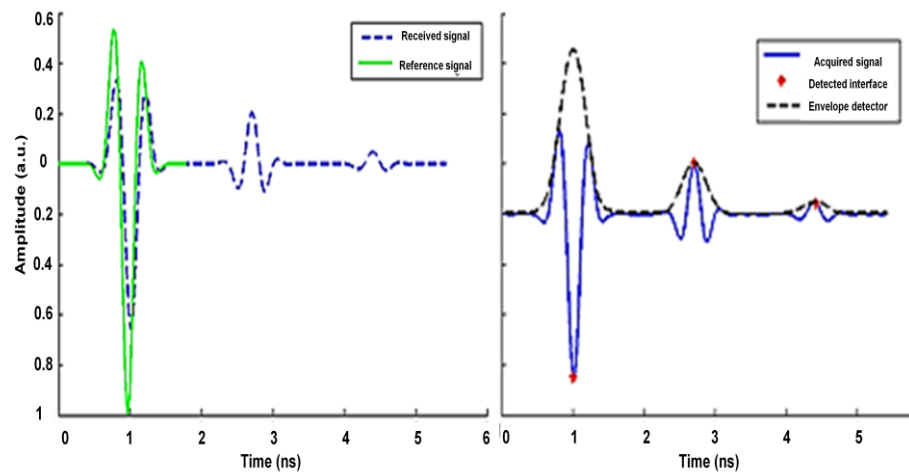


Figure 9.4. (a) Reference signal and received signal (b) Received signal and peak detector

Ultimately, the permittivity profile and interface depth are obtained from the estimation of the interfaces and amplitude derived from synthetic backscattered signal were used in iteratively derivation of thickness layers.

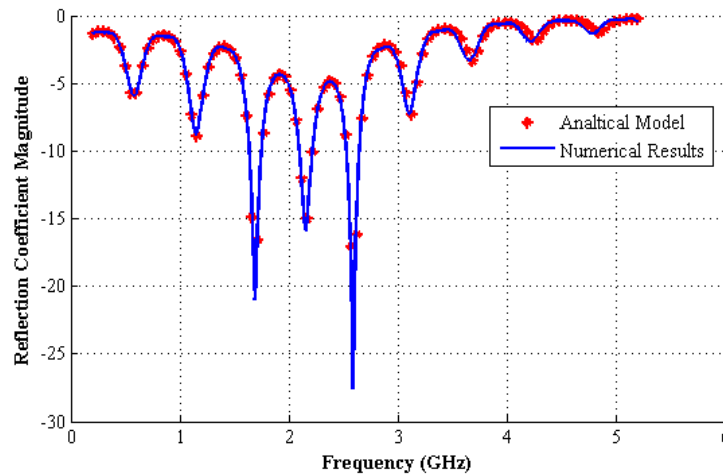


Figure 9. 3 Comparison between the analytical and numerical reflection coefficient magnitude for human tissue

Table.9.1 Numerical assessment of proposed algorithm

Tissues	Permittivity	Thickness
Skin	1.05%	0.51%
Fat	4.1%	1.46%
Muscle	5.21%.	1.98%

9.6 Conclusion

In this chapter overall reflection response from a simplified modeled upper arm structure calculated through propagation matrices toward soft tissue artifact evaluation. A soft tissue thickness calculation methodology is elaborated and verified by simulation. This pilot study can be extended in 3d and attach to other soft tissue artifact measurements to assist tracking and monitoring upper limbs kinematics.

Bibliography

- [1] R. G. Cucu, A. G. Podoleanu, J. A. Rogers, J. Pedro, and R. B. Rosen, "Combined confocal/en face T-scan-based ultrahigh-resolution optical coherence tomography in vivo retinal imaging," *Optics letters*, vol. 31, pp. 1684-1686, 2006.
- [2] J. M. Schmitt, "Optical coherence tomography (OCT): a review," *Selected Topics in Quantum Electronics, IEEE Journal of*, vol. 5, pp. 1205-1215, 1999.
- [3] R. Leitgeb, C. Hitzenberger, and A. Fercher, "Performance of fourier domain vs. time domain optical coherence tomography," *Optics Express*, vol. 11, pp. 889-894, 2003.
- [4] A. G. Podoleanu, "Optical coherence tomography," *The British journal of radiology*, 2014.
- [5] J. Welzel, "Optical coherence tomography in dermatology: a review," *Skin Research and Technology*, vol. 7, pp. 1-9, 2001.
- [6] J. G. Fujimoto, C. Pitris, S. A. Boppart, and M. E. Brezinski, "Optical coherence tomography: an emerging technology for biomedical imaging and optical biopsy," *Neoplasia*, vol. 2, pp. 9-25, 2000.
- [7] A. M. Zysk, F. T. Nguyen, A. L. Oldenburg, D. L. Marks, and S. A. Boppart, "Optical coherence tomography: a review of clinical development from bench to bedside," *Journal of biomedical optics*, vol. 12, pp. 051403-051403-21, 2007.
- [8] W. Drexler and J. G. Fujimoto, *Optical coherence tomography: technology and applications*: Springer Science & Business Media, 2008.
- [9] J. M. Schmitt, A. Knuttel, M. Yadlowsky, and M. Eckhaus, "Optical-coherence tomography of a dense tissue: statistics of attenuation and backscattering," *Physics in Medicine and Biology*, vol. 39, p. 1705, 1994.
- [10] L. Thrane, M. H. Frosz, T. M. Jørgensen, A. Tycho, H. T. Yura, and P. E. Andersen, "Extraction of optical scattering parameters and attenuation compensation in optical coherence tomography images of multilayered tissue structures," *Optics letters*, vol. 29, pp. 1641-1643, 2004.
- [11] J. M. Schmitt, S. Xiang, and K. M. Yung, "Speckle in optical coherence tomography," *Journal of biomedical optics*, vol. 4, pp. 95-105, 1999.
- [12] R. Leitgeb, C. Hitzenberger, and A. F. Fercher, "Performance of fourier domain vs. time domain optical coherence tomography," *Optics express*, vol. 11, pp. 889-894, 2003.

- [13] D. Huang, E. A. Swanson, C. P. Lin, J. S. Schuman, W. G. Stinson, W. Chang, *et al.*, "Optical coherence tomography," *Science*, vol. 254, pp. 1178-1181, 1991.
- [14] A. F. Fercher, W. Drexler, C. K. Hitzenberger, and T. Lasser, "Optical coherence tomography-principles and applications," *Reports on progress in physics*, vol. 66, p. 239, 2003.
- [15] S. Yun, G. Tearney, J. de Boer, N. Iftimia, and B. Bouma, "High-speed optical frequency-domain imaging," *Optics Express*, vol. 11, pp. 2953-2963, 2003.
- [16] T. Wilson, "Confocal microscopy," *Academic Press: London, etc*, vol. 426, pp. 1-64, 1990.
- [17] M. A. Choma, M. V. Sarunic, C. Yang, and J. A. Izatt, "Sensitivity advantage of swept source and Fourier domain optical coherence tomography," *Optics express*, vol. 11, pp. 2183-2189, 2003.
- [18] L. Thrane, H. T. Yura, and P. E. Andersen, "Analysis of optical coherence tomography systems based on the extended Huygens–Fresnel principle," *JOSA A*, vol. 17, pp. 484-490, 2000.
- [19] J. W. Goodman, "Statistical properties of laser speckle patterns," in *Laser speckle and related phenomena*, ed: Springer, 1975, pp. 9-75.
- [20] B. Shapiro, "Large intensity fluctuations for wave propagation in random media," *Physical review letters*, vol. 57, p. 2168, 1986.
- [21] M. A. Webster, K. J. Webb, A. M. Weiner, J. Xu, and H. Cao, "Temporal response of a random medium from speckle intensity frequency correlations," *JOSA A*, vol. 20, pp. 2057-2070, 2003.
- [22] J. W. Goodman, *Introduction to Fourier optics*: Roberts and Company Publishers, 2005.
- [23] J. W. Goodman, *Speckle phenomena in optics: theory and applications*: Roberts and Company Publishers, 2007.
- [24] R. F. Wagner, S. W. Smith, J. M. Sandrik, and H. Lopez, "Statistics of speckle in ultrasound B-scans," *Sonics and Ultrasonics, IEEE Transactions on*, vol. 30, pp. 156-163, 1983.
- [25] M. R. Hee, J. A. Izatt, E. A. Swanson, D. Huang, J. S. Schuman, C. P. Lin, *et al.*, "Optical coherence tomography of the human retina," *Archives of ophthalmology*, vol. 113, pp. 325-332, 1995.
- [26] P. A. Magnin, O. T. von Ramm, and F. L. Thurstone, "Frequency compounding for speckle contrast reduction in phased array images," *Ultrasonic imaging*, vol. 4, pp. 267-281, 1982.
- [27] T. M. Jørgensen, L. Thrane, M. Mogensen, F. Pedersen, and P. E. Andersen, "Speckle reduction in optical coherence tomography images of human skin by a spatial diversity method," in *European Conference on Biomedical Optics*, 2007, p. 6627_22.

-
- [28] N. Iftimia, B. E. Bouma, and G. J. Tearney, "Speckle reduction in optical coherence tomography by "path length encoded" angular compounding," *Journal of biomedical optics*, vol. 8, pp. 260-263, 2003.
- [29] H. L. Resnikoff and O. Raymond Jr, *Wavelet analysis: the scalable structure of information*: Springer Science & Business Media, 2012.
- [30] R. K. Wang, "Reduction of speckle noise for optical coherence tomography by the use of nonlinear anisotropic diffusion," in *Biomedical Optics 2005*, 2005, pp. 380-385.
- [31] D. J. Smithies, T. Lindmo, Z. Chen, J. S. Nelson, and T. E. Milner, "Signal attenuation and localization in optical coherence tomography studied by Monte Carlo simulation," *Physics in Medicine and Biology*, vol. 43, p. 3025, 1998.
- [32] D. C. Adler, T. H. Ko, and J. G. Fujimoto, "Speckle reduction in optical coherence tomography images by use of a spatially adaptive wavelet filter," *Optics letters*, vol. 29, pp. 2878-2880, 2004.
- [33] A. Lopes, R. Touzi, and E. Nezry, "Adaptive speckle filters and scene heterogeneity," *Geoscience and Remote Sensing, IEEE Transactions on*, vol. 28, pp. 992-1000, 1990.
- [34] A. Nieminen, P. Heinonen, and Y. Neuvo, "A new class of detail-preserving filters for image processing," *Pattern Analysis and Machine Intelligence, IEEE Transactions on*, pp. 74-90, 1987.
- [35] Y. Funama, Y. Noguchi, and M. Shimamura, "Reduction of Artifacts in Degraded CT Image by Adaptive Wiener Filter," *Journal of Med. Electron. Biol. Eng.*, vol. 40, pp. 1-6, 2002.
- [36] J. Kim, D. T. Miller, E. Kim, S. Oh, J. Oh, and T. E. Milner, "Optical coherence tomography speckle reduction by a partially spatially coherent source," *Journal of Biomedical Optics*, vol. 10, pp. 064034-064034-9, 2005.
- [37] G. Karasakal and I. Erer, "Speckle noise reduction in SAR imaging using lattice filters based subband decomposition," in *Geoscience and Remote Sensing Symposium, 2007. IGARSS 2007. IEEE International*, 2007, pp. 1476-1480.
- [38] B. K. Alsberg, A. M. Woodward, M. K. Winson, J. Rowland, and D. B. Kell, "Wavelet denoising of infrared spectra," *Analyst*, vol. 122, pp. 645-652, 1997.
- [39] B. Sander, M. Larsen, L. Thrane, J. Hougaard, and T. Jørgensen, "Enhanced optical coherence tomography imaging by multiple scan averaging," *British Journal of Ophthalmology*, vol. 89, pp. 207-212, 2005.
- [40] A. Ozcan, A. Bilenca, A. E. Desjardins, B. E. Bouma, and G. J. Tearney, "Speckle reduction in optical coherence tomography images using digital filtering," *JOSA A*, vol. 24, pp. 1901-1910, 2007.

-
- [41] J. Rogowska and M. E. Brezinski, "Evaluation of the adaptive speckle suppression filter for coronary optical coherence tomography imaging," *Medical Imaging, IEEE Transactions on*, vol. 19, pp. 1261-1266, 2000.
- [42] P. Puvanathan and K. Bizheva, "Speckle noise reduction algorithm for optical coherence tomography based on interval type II fuzzy set," *Optics express*, vol. 15, pp. 15747-15758, 2007.
- [43] M. Avanaki, P. Laissue, A. G. Podoleanu, A. Aber, and S. Hojjatoleslami, "Evaluation of wavelet mother functions for speckle noise suppression in OCT images," *Int. J. Graphics Bioinf. Med. Eng.*, vol. 11, pp. 1-5, 2011.
- [44] L. I. Rudin, S. Osher, and E. Fatemi, "Nonlinear total variation based noise removal algorithms," *Physica D: Nonlinear Phenomena*, vol. 60, pp. 259-268, 1992.
- [45] J.-N. Hwang, S.-R. Lay, and A. Lippman, "Nonparametric multivariate density estimation: a comparative study," *Signal Processing, IEEE Transactions on*, vol. 42, pp. 2795-2810, 1994.
- [46] H. Park, R. Miyazaki, T. Nishimura, and Y. Tamaki, "The speckle noise reduction and the boundary enhancement on medical ultrasound images using the cellular neural networks," *電気学会論文誌. C*, vol. 127, pp. 1726-1731, 2007.
- [47] M. R. Avanaki, P. P. Laissue, A. G. Podoleanu, and A. Hojjat, "Denoising based on noise parameter estimation in speckled OCT images using neural network," in *1st Canterbury Workshop and School in Optical Coherence Tomography and Adaptive Optics*, 2008, pp. 71390E-71390E-9.
- [48] M. R. Avanaki, P. P. Laissue, T. J. Eom, A. G. Podoleanu, and A. Hojjatoleslami, "Speckle reduction using an artificial neural network algorithm," *Applied optics*, vol. 52, pp. 5050-5057, 2013.
- [49] P. M. Shankar, "Speckle reduction in ultrasound B-scans using weighted averaging in spatial compounding," *IEEE transactions on ultrasonics, ferroelectrics, and frequency control*, vol. 33, pp. 754-758, 1986.
- [50] M. Pircher, E. Go, R. Leitgeb, A. F. Fercher, and C. K. Hitzenberger, "Speckle reduction in optical coherence tomography by frequency compounding," *Journal of Biomedical Optics*, vol. 8, pp. 565-569, 2003.
- [51] J. W. Goodman, "Some fundamental properties of speckle*," *Journal of the Optical Society of America*, vol. 66, pp. 1145-1150, 1976/11/01 1976.
- [52] M. R. Avanaki, R. Cernat, P. J. Tadrous, T. Tatla, A. G. Podoleanu, and S. A. Hojjatoleslami, "Spatial compounding algorithm for speckle reduction of dynamic focus OCT images," *Photonics Technology Letters, IEEE*, vol. 25, pp. 1439-1442, 2013.

-
- [53] M. R. Avanaki, M. J. Marques, A. Bradu, A. Hojjatoleslami, and A. G. Podoleanu, "A new algorithm for speckle reduction of optical coherence tomography images," in *SPIE BiOS*, 2014, pp. 893437-893437-9.
- [54] E. Hecht and A. Zajac, "Optics Addison-Wesley," *Reading, Mass*, pp. 301-305, 1974.
- [55] F. Vargas-Martin, P. M. Prieto, and P. Artal, "Correction of the aberrations in the human eye with a liquid-crystal spatial light modulator: limits to performance," *JOSA A*, vol. 15, pp. 2552-2562, 1998.
- [56] M. L. Plett, P. R. Barbier, and D. W. Rush, "Compact adaptive optical system based on blind optimization and a micromachined membrane deformable mirror," *Applied optics*, vol. 40, pp. 327-330, 2001.
- [57] M. Booth, "Wave front sensor-less adaptive optics: a model-based approach using sphere packings," *Optics Express*, vol. 14, pp. 1339-1352, 2006.
- [58] E. Grisan, F. Frassetto, V. Da Deppo, G. Naletto, and A. Ruggeri, "No wavefront sensor adaptive optics system for compensation of primary aberrations by software analysis of a point source image. 1. Methods," *Applied optics*, vol. 46, pp. 6434-6441, 2007.
- [59] M. Nasiri-Avanaki, H. Sarmadi, A. Meadway, A. G. Podoleanu, and S. Hojjatoleslami, "Comparative assessment of three algorithms to control a deformable mirror for an adaptive optics system with no wavefront sensor," in *SPIE BiOS*, 2011, pp. 790415-790415-7.
- [60] J. M. Schmitt and Z. Liang, "Deconvolution and enhancement of optical coherence tomograms," in *BiOS'97, Part of Photonics West*, 1997, pp. 46-57.
- [61] Y. Liu, Y. Liang, G. Mu, and X. Zhu, "Deconvolution methods for image deblurring in optical coherence tomography," *JOSA A*, vol. 26, pp. 72-77, 2009.
- [62] M. Kulkarni, C. Thomas, and J. Izatt, "Image enhancement in optical coherence tomography using deconvolution," *Electronics Letters*, vol. 33, pp. 1365-1367, 1997.
- [63] T. S. Ralston, D. L. Marks, F. Kamalabadi, and S. A. Boppart, "Deconvolution methods for mitigation of transverse blurring in optical coherence tomography," *Image Processing, IEEE Transactions on*, vol. 14, pp. 1254-1264, 2005.
- [64] A. P. Dhawan, R. M. Rangayyan, and R. Gordon, "Image restoration by Wiener deconvolution in limited-view computed tomography," *Applied optics*, vol. 24, pp. 4013-4020, 1985.
- [65] D. Fish, J. Walker, A. Brinicombe, and E. Pike, "Blind deconvolution by means of the Richardson-Lucy algorithm," *JOSA A*, vol. 12, pp. 58-65, 1995.

- [66] S. Hojjatoleslami, M. Avanaki, and A. G. Podoleanu, "Image quality improvement in optical coherence tomography using Lucy–Richardson deconvolution algorithm," *Applied optics*, vol. 52, pp. 5663-5670, 2013.
- [67] J. Ge, R. Erbel, T. Gerber, G. Görge, L. Koch, M. Haude, *et al.*, "Intravascular ultrasound imaging of angiographically normal coronary arteries: a prospective study in vivo," *British heart journal*, vol. 71, pp. 572-578, 1994.
- [68] T. L. Szabo, *Diagnostic ultrasound imaging: inside out*: Academic Press, 2004.
- [69] J. Welzel, E. Lanckenau, R. Birngruber, and R. Engelhardt, "Optical coherence tomography of the human skin," *Journal of the American Academy of Dermatology*, vol. 37, pp. 958-963, 1997.
- [70] T. Gambichler, R. Matip, G. Moussa, P. Altmeyer, and K. Hoffmann, "In vivo data of epidermal thickness evaluated by optical coherence tomography: effects of age, gender, skin type, and anatomic site," *Journal of dermatological science*, vol. 44, pp. 145-152, 2006.
- [71] M. C. Pierce, J. Strasswimmer, B. H. Park, B. Cense, and J. F. de Boer, "Advances in optical coherence tomography imaging for dermatology," *Journal of investigative dermatology*, vol. 123, pp. 458-463, 2004.
- [72] M. Boone, A. Marneffe, M. Suppa, M. Miyamoto, I. Alarcon, R. Hofmann-Wellenhof, *et al.*, "High-definition optical coherence tomography algorithm for the discrimination of actinic keratosis from normal skin and from squamous cell carcinoma," *Journal of the European Academy of Dermatology and Venereology*, vol. 29, pp. 1606-1615, 2015.
- [73] K.-S. Lee, H. Zhao, S. F. Ibrahim, N. Meemon, L. Khoudeir, and J. P. Rolland, "Three-dimensional imaging of normal skin and nonmelanoma skin cancer with cellular resolution using Gabor domain optical coherence microscopy," *Journal of biomedical optics*, vol. 17, pp. 126006-126006, 2012.
- [74] C. Reggiani, M. Manfredini, V. Mandel, F. Farnetani, S. Ciardo, S. Bassoli, *et al.*, "Update on non-invasive imaging techniques in early diagnosis of non-melanoma skin cancer," *Giornale italiano di dermatologia e venereologia: organo ufficiale, Societa italiana di dermatologia e sifilografia*, vol. 150, pp. 393-405, 2015.
- [75] P. B. T. Moraes, M. P. Cohen, E. E. Gomes, d. M. M. Petaccia, d. S. B. M. Ferreira, G. F. J. Tavares, *et al.*, "Optical coherence tomography (OCT) features of nevi and melanomas and their association with intraepidermal or dermal involvement: A pilot study," *Journal of the American Academy of Dermatology*, vol. 73, p. 315, 2015.
- [76] M. Boone, M. Suppa, A. Marneffe, M. Miyamoto, G. Jemec, and V. Del Marmol, "High-definition optical coherence tomography intrinsic skin

- ageing assessment in women: a pilot study," *Archives of dermatological research*, vol. 307, pp. 705-720, 2015.
- [77] H. Ring, A. Hussain, G. Jemec, R. Gniadecki, L. Gjerdrum, and M. Mogensen, "Imaging of cutaneous T-cell lymphomas by optical coherence tomography—a case series study," *Journal of the European Academy of Dermatology and Venereology*, 2015.
- [78] A. A. Hussain, L. Themstrup, and G. B. E. Jemec, "Optical coherence tomography in the diagnosis of basal cell carcinoma," *Archives of dermatological research*, vol. 307, pp. 1-10, 2015.
- [79] N. D. Gladkova, G. Petrova, N. Nikulin, S. Radenska-Lopovok, L. Snopova, Y. P. Chumakov, *et al.*, "In vivo optical coherence tomography imaging of human skin: norm and pathology," *Skin Research and Technology*, vol. 6, pp. 6-16, 2000.
- [80] Y. Pan and D. L. Farkas, "Noninvasive imaging of living human skin with dual-wavelength optical coherence tomography in two and three dimensions," *Journal of biomedical optics*, vol. 3, pp. 446-455, 1998.
- [81] J. Schmitt, M. Yadlowsky, and R. Bonner, "Subsurface imaging of living skin with optical coherence microscopy," *Dermatology*, vol. 191, pp. 93-98, 1995.
- [82] K. Schicho, R. Seemann, M. Binder, and M. Figl, "Optical coherence tomography for planning of follicular unit extraction," *Dermatologic Surgery*, vol. 41, pp. 358-363, 2015.
- [83] N. Greaves, B. Benatar, S. Whiteside, T. Alonso-Rasgado, M. Baguneid, and A. Bayat, "Optical coherence tomography: a reliable alternative to invasive histological assessment of acute wound healing in human skin?," *British Journal of Dermatology*, vol. 170, pp. 840-850, 2014.
- [84] D. P. Popescu, C. Fluerau, Y. Mao, S. Chang, and M. G. Sowa, "Signal attenuation and box-counting fractal analysis of optical coherence tomography images of arterial tissue," *Biomedical optics express*, vol. 1, pp. 268-277, 2010.
- [85] J. Schmitt, A. Knüttel, and R. Bonner, "Measurement of optical properties of biological tissues by low-coherence reflectometry," *Applied Optics*, vol. 32, pp. 6032-6042, 1993.
- [86] S. Kurugol, M. Rajadhyaksha, J. G. Dy, and D. H. Brooks, "Validation study of automated dermal/epidermal junction localization algorithm in reflectance confocal microscopy images of skin," in *SPIE BiOS*, 2012, pp. 820702-820702-11.
- [87] J. K. Barton, K. W. Gossage, W. Xu, J. R. Ranger-Moore, K. Saboda, C. A. Brooks, *et al.*, "Investigating sun-damaged skin and actinic keratosis with optical coherence tomography: a pilot study," *Technology in cancer research & treatment*, vol. 2, pp. 525-535, 2003.
- [88] P. K. Buxton and R. Morris-Jones, *ABC of Dermatology*: John Wiley & Sons, 2013.

- [89] M. R. Avanaki, A. Hojjatoleslami, M. Sira, J. B. Schofield, C. Jones, and A. G. Podoleanu, "Investigation of basal cell carcinoma using dynamic focus optical coherence tomography," *Applied optics*, vol. 52, pp. 2116-2124, 2013.
- [90] M. R. Avanaki, A. Hojjat, and A. G. Podoleanu, "Investigation of computer-based skin cancer detection using optical coherence tomography," *Journal of Modern Optics*, vol. 56, pp. 1536-1544, 2009.
- [91] D. Woodley, "Importance of the dermal-epidermal junction and recent advances," *Dermatology*, vol. 174, pp. 1-10, 1987.
- [92] L. K. Jensen, L. Thrane, P. E. Andersen, A. Tycho, F. Pedersen, S. Andersson-Engels, *et al.*, "Optical coherence tomography in clinical examination of non-pigmented skin malignancies," in *European Conference on Biomedical Optics*, 2003, p. 5140_160.
- [93] S. Neerken, G. W. Lucassen, M. A. Bisschop, E. Lenderink, and T. A. Nuijs, "Characterization of age-related effects in human skin: a comparative study that applies confocal laser scanning microscopy and optical coherence tomography," *Journal of biomedical optics*, vol. 9, pp. 274-281, 2004.
- [94] J. Weissman, T. Hancewicz, and P. Kaplan, "Optical coherence tomography of skin for measurement of epidermal thickness by shapelet-based image analysis," *Optics express*, vol. 12, pp. 5760-5769, 2004.
- [95] Y. Hori, Y. Yasuno, S. Sakai, M. Matsumoto, T. Sugawara, V. D. Madjarova, *et al.*, "Automatic characterization and segmentation of human skin using three-dimensional optical coherence tomography," *optics express*, vol. 14, pp. 1862-1877, 2006.
- [96] A. Mcheik, C. Tauber, H. Batatia, J. George, and J.-M. Lagarde, "Speckle Modelization in OCT Images for Skin Layers Segmentation," in *VISAPP (1)*, 2008, pp. 347-350.
- [97] C. Wang, T. Huo, J.-G. Zheng, N. Zhang, T. Chen, W. Liao, *et al.*, "Automated assessment of epidermal thickness and vascular density of port wine stains oct image," *Journal of Innovative Optical Health Sciences*, vol. 7, p. 1350052, 2014.
- [98] A. Li, J. Cheng, A. P. Yow, C. Wall, D. W. K. Wong, H. L. Tey, *et al.*, "Epidermal segmentation in high-definition optical coherence tomography," in *Engineering in Medicine and Biology Society (EMBC), 2015 37th Annual International Conference of the IEEE*, 2015, pp. 3045-3048.
- [99] G. Josse, J. George, and D. Black, "Automatic measurement of epidermal thickness from optical coherence tomography images using a new algorithm," *Skin Research and Technology*, vol. 17, pp. 314-319, 2011.

-
- [100] M. Mogensen, H. A. Morsy, L. Thrane, and G. B. Jemec, "Morphology and epidermal thickness of normal skin imaged by optical coherence tomography," *Dermatology*, vol. 217, pp. 14-20, 2008.
- [101] K. Hornik, M. Stinchcombe, and H. White, "Multilayer feedforward networks are universal approximators," *Neural networks*, vol. 2, pp. 359-366, 1989.
- [102] M. Minsky and S. Papert, "Perceptrons," 1969.
- [103] J. Goodman, "Statistical Optics John Wiley & Sons," *New York*, 1985.
- [104] J. W. Goodman, "Some fundamental properties of speckle," *JOSA*, vol. 66, pp. 1145-1150, 1976.
- [105] S. Adabi, S. Conforto, A. Clayton, A. G. Podoleanu, A. Hojjat, and M. Avanaki, "An intelligent speckle reduction algorithm for optical coherence tomography images," in *4th International Conference on Photonics, Optics and Laser Technology, PHOTOPTICS 2016*, 2016, pp. 40-45.
- [106] M. Bashkansky and J. Reintjes, "Statistics and reduction of speckle in optical coherence tomography," *Optics Letters*, vol. 25, pp. 545-547, 2000.
- [107] M. Hughes, M. Spring, and A. Podoleanu, "Speckle noise reduction in optical coherence tomography of paint layers," *Applied optics*, vol. 49, pp. 99-107, 2010.
- [108] M. R. Avanaki and A. Hojjatoleslami, "Speckle reduction with attenuation compensation for skin OCT images enhancement," *Proceeding of Medical Image Understanding and Analysis (MIUA), Kingston University, London*, pp. 14-15, 2009.
- [109] T. B. Fitzpatrick, "Soleil et peau," *J Med Esthet*, vol. 2, pp. 33-34, 1975.
- [110] T. Gambichler, G. Moussa, M. Sand, D. Sand, P. Altmeyer, and K. Hoffmann, "Applications of optical coherence tomography in dermatology," *Journal of dermatological science*, vol. 40, pp. 85-94, 2005.
- [111] R. Hou, T. Le, S. D. Murgu, Z. Chen, and M. Brenner, "Recent advances in optical coherence tomography for the diagnoses of lung disorders," *Expert review of respiratory medicine*, vol. 5, pp. 711-724, 2011.
- [112] M. R. Avanaki, A. G. Podoleanu, M. C. Price, S. A. Corr, and S. Hojjatoleslami, "Two applications of solid phantoms in performance assessment of optical coherence tomography systems," *Applied optics*, vol. 52, pp. 7054-7061, 2013.
- [113] D. Harwood, M. Subbarao, H. Hakalahti, and L. S. Davis, "A new class of edge-preserving smoothing filters," *Pattern Recognition Letters*, vol. 6, pp. 155-162, 1987.
- [114] M. Kuwahara, K. Hachimura, S. Eiho, and M. Kinoshita, "Processing of RI-angiocardigraphic images," in *Digital processing of biomedical images*, ed: Springer, 1976, pp. 187-202.

- [115] P. Bakker, L. J. van Vliet, and P. W. Verbeek, "Edge preserving orientation adaptive filtering," in *Computer Vision and Pattern Recognition, 1999. IEEE Computer Society Conference on.*, 1999.
- [116] A. Buades, B. Coll, and J.-M. Morel, "A non-local algorithm for image denoising," in *2005 IEEE Computer Society Conference on Computer Vision and Pattern Recognition (CVPR'05)*, 2005, pp. 60-65.
- [117] K. Dabov, A. Foi, V. Katkovnik, and K. Egiazarian, "Image denoising by sparse 3-D transform-domain collaborative filtering," *IEEE Transactions on image processing*, vol. 16, pp. 2080-2095, 2007.
- [118] J. E. Kyprianidis, H. Kang, and J. Döllner, "Image and video abstraction by anisotropic kuwahara filtering," in *Computer Graphics Forum*, 2009, pp. 1955-1963.
- [119] J. S. Lim, "Two-dimensional signal and image processing," *Englewood Cliffs, NJ, Prentice Hall, 1990, 710 p.*, vol. 1, 1990.
- [120] A. Lopes, R. Touzi, and E. Nezry, "Adaptive speckle filters and scene heterogeneity," *IEEE Transactions on geoscience and remote sensing*, vol. 28, pp. 992-1000, 1990.
- [121] K. Dabov, A. Foi, V. Katkovnik, and K. Egiazarian, "Image restoration by sparse 3D transform-domain collaborative filtering," in *Electronic Imaging 2008*, 2008, pp. 681207-681207-12.
- [122] K. W. Gossage, T. S. Tkaczyk, J. J. Rodriguez, and J. K. Barton, "Texture analysis of optical coherence tomography images: feasibility for tissue classification," *Journal of biomedical optics*, vol. 8, pp. 570-575, 2003.
- [123] K. W. Gossage, C. M. Smith, E. M. Kanter, L. P. Hariri, A. L. Stone, J. J. Rodriguez, *et al.*, "Texture analysis of speckle in optical coherence tomography images of tissue phantoms," *Physics in medicine and biology*, vol. 51, p. 1563, 2006.
- [124] R. M. Haralick and K. Shanmugam, "Textural features for image classification," *IEEE Transactions on systems, man, and cybernetics*, pp. 610-621, 1973.
- [125] K. Vermeer, J. Mo, J. Weda, H. Lemij, and J. de Boer, "Depth-resolved model-based reconstruction of attenuation coefficients in optical coherence tomography," *Biomedical optics express*, vol. 5, pp. 322-337, 2014.
- [126] H. M. Salinas, and Delia Cabrera Fernandez., "Comparison of PDE-based nonlinear diffusion approaches for image enhancement and denoising in optical coherence tomography," *IEEE Transactions on Medical Imaging*, vol. 26, pp. 761-771, 2007.
- [127] Z. Wang, Alan C. Bovik, Hamid R. Sheikh, and Eero P. Simoncelli., "Image quality assessment: from error visibility to structural similarity," *IEEE transactions on image processing* vol. 13, pp. 600-612, 2004.

-
- [128] T. Storen, A. Royset, N.-H. Giskeodegard, H. M. Pedersen, and T. Lindmo, "Comparison of speckle reduction using polarization diversity and frequency compounding in optical coherence tomography," in *Biomedical Optics 2004*, 2004, pp. 196-204.
- [129] R. Williamson, "Polarization Optics Tutorial: Polarizers, Waveplates, Rotators and Lyot Filters," 2005.
- [130] G. E. Hinton, and Ruslan R. Salakhutdinov., "Reducing the dimensionality of data with neural networks," *science* 313.5786, pp. 504-507, 2006.
- [131] P. Refaeilzadeh, L. Tang, and H. Liu, "Cross-validation," in *Encyclopedia of database systems*, ed: Springer, 2009, pp. 532-538.
- [132] F. Jin, P. Fieguth, L. Winger, and E. Jernigan, "Adaptive Wiener filtering of noisy images and image sequences," in *Image Processing, 2003. ICIP 2003. Proceedings. 2003 International Conference on*, 2003, pp. III-349-52 vol. 2.
- [133] E. Rashedi, Abdolreza Mirzaei, and Mohammad Rahmati., "An information theoretic approach to hierarchical clustering combination," *Neurocomputing* vol. 148, pp. 487-497, 2015.
- [134] E. Rashedi, Abdolreza Mirzaei, and Mohammad Rahmati., "Optimized aggregation function in hierarchical clustering combination," *Intelligent Data Analysis*, vol. 20, pp. 281-291, 2016.
- [135] A. Krishnaswamy and G. V. Baranoski, "A study on skin optics," *Natural Phenomena Simulation Group, School of Computer Science, University of Waterloo, Canada, Technical Report*, vol. 1, pp. 1-17, 2004.
- [136] C. Xu, J. M. Schmitt, S. G. Carlier, and R. Virmani, "Characterization of atherosclerosis plaques by measuring both backscattering and attenuation coefficients in optical coherence tomography," *Journal of biomedical optics*, vol. 13, pp. 034003-034003-8, 2008.
- [137] P. Gong, R. A. McLaughlin, Y. M. Liew, P. R. Munro, F. M. Wood, and D. D. Sampson, "Assessment of human burn scars with optical coherence tomography by imaging the attenuation coefficient of tissue after vascular masking," *Journal of biomedical optics*, vol. 19, pp. 021111-021111, 2014.
- [138] V. J. Srinivasan, E. T. Mandeville, A. Can, F. Blasi, M. Klimov, A. Daneshmand, *et al.*, "Multiparametric, longitudinal optical coherence tomography imaging reveals acute injury and chronic recovery in experimental ischemic stroke," *PloS one*, vol. 8, p. e71478, 2013.
- [139] J.-S. Lee, "Digital image enhancement and noise filtering by use of local statistics," *IEEE transactions on pattern analysis and machine intelligence*, pp. 165-168, 1980.
- [140] R. C. Gonzalez, R. E. Woods, and S. L. Eddins, *Digital image processing using MATLAB*: Pearson Education India, 2004.

- [141] M. Avanaki, A. G. Podoleanu, M. C. Price, S. A. Corr, and S. Hojjatoleslami, "Two applications of solid phantoms in performance assessment of optical coherence tomography systems," *Applied optics*, vol. 52, pp. 7054-7061, 2013.
- [142] C. Chen, F. Klämpfl, C. Knipfer, M. Riemann, R. Kanawade, F. Stelzle, *et al.*, "Preparation of a skin equivalent phantom with interior micron-scale vessel structures for optical imaging experiments," *Biomedical optics express*, vol. 5, pp. 3140-3149, 2014.
- [143] C. Chen, F. Klämpfl, C. Knipfer, M. Riemann, R. Kanawade, F. Stelzle, *et al.*, "Preparation of a skin equivalent phantom with interior micron-scale vessel structures for optical imaging experiments," *Biomed Opt Express*, vol. 5, pp. 3140-9, Sep 1 2014.
- [144] http://omlc.org/calc/mie_calc.html.
- [145] M. Van Gemert, S. L. Jacques, H. Sterenborg, and W. Star, "Skin optics," *Biomedical Engineering, IEEE Transactions on*, vol. 36, pp. 1146-1154, 1989.
- [146] A. N. Bashkatov, E. A. Genina, and V. V. Tuchin, "Optical properties of skin, subcutaneous, and muscle tissues: a review," *Journal of Innovative Optical Health Sciences*, vol. 4, pp. 9-38, 2011.
- [147] M. A. Mayer, Anja Borsdorf, Martin Wagner, Joachim Hornegger, Christian Y. Mardin, and Ralf P. Tornow. , "Wavelet denoising of multiframe optical coherence tomography data," *Biomedical optics express*, vol. 3, pp. 572-589, 2012.
- [148] J. G. Fujimoto, "Optical Coherence Tomography," *Applied physics*, pp. 1099-1111, 2001.
- [149] J. M. Schmitt, "Optical Coherence Tomography (OCT): A Review," *IEEE Journal of Selected Topics In Quantum Electronics*, vol. 5, pp. 1205-1215, 1999.
- [150] B. Hermann, E. J. Fernandez, A. Unterhuber, H. Sattman, A. F. Fercher, W. Drexler, *et al.*, "Adaptive-optics ultrahigh-resolution optical coherence tomography," *Opt. Lett.* 29, pp. 2142-2144, 2004.
- [151] T. S. Ralston, D. Marks, F. Kamalabadi, and S. A. Boppart, "Gaussian beam deconvolution in optical coherence tomography," in *SPIE*, 2005.
- [152] J. M. Schmitt and Z. Liang, "Deconvolution and enhancement of optical coherence tomograms," in *Proceedings of SPIE - The International Society for Optical Engineering*, 1997.
- [153] Y. Liu, Y. Liang, G. Mu, and X. Zhu, "Deconvolution methods for image deblurring in optical coherence tomography," *Optical Society of America*, pp. 72-77, 2009.
- [154] P. D. Wooliams, R. A. Ferguson, C. Hart, A. Grimwood, and P. H. Tomlins, "Spatially deconvolved optical coherence tomography," *Applied Optics*, pp. 2014-2021, 2010.

-
- [155] S. A. Hojjatoleslami, M. R. Avanaki, and A. G. Podoleanu, "Image quality improvement in optical coherence tomography using Lucy–Richardson deconvolution algorithm," *Applied Optics*, pp. 5663-5670, 2013.
- [156] B. E. Saleh, M. C. Teich, and B. E. Saleh, *Fundamentals of photonics* vol. 22: Wiley New York, 1991.
- [157] P. D. Woolliams, R. A. Ferguson, C. Hart, A. Grimwood, and P. H. Tomlins, "Spatially deconvolved optical coherence tomography," *Applied optics*, vol. 49, pp. 2014-2021, 2010.
- [158] J. P. Oliveira, J. M. Bioucas-Dias, and M. A. Figueiredo, "Adaptive total variation image deblurring: a majorization–minimization approach," *Signal Processing*, vol. 89, pp. 1683-1693, 2009.
- [159] J. M. Bioucas-Dias, M. A. T. Figueiredo, and J. P. Oliveira, "Total Variation-Based Image Deconvolution: a Majorization-Minimization Approach," in *IEEE International Conference on Acoustics Speech and Signal Processing Proceedings*, 2006.
- [160] A. Hojjatoleslami and M. R. Avanaki, "OCT skin image enhancement through attenuation compensation," *Applied optics*, vol. 51, pp. 4927-4935, 2012.
- [161] M. R. Avanaki, A. G. Podoleanu, J. B. Schofield, C. Jones, M. Sira, Y. Liu, *et al.*, "Quantitative evaluation of scattering in optical coherence tomography skin images using the extended Huygens–Fresnel theorem," *Applied optics*, vol. 52, pp. 1574-1580, 2013.
- [162] C. F. Bohren and D. R. Huffman, *Absorption and scattering of light by small particles*: John Wiley & Sons, 2008.
- [163] W. Y. Yang, W. Cao, T.-S. Chung, and J. Morris, *Applied numerical methods using MATLAB*: John Wiley & Sons, 2005.
- [164] S. J. Chiu, X. T. Li, P. Nicholas, C. A. Toth, J. A. Izatt, and S. Farsiu, "Automatic segmentation of seven retinal layers in SDOCT images congruent with expert manual segmentation," *Optics express*, vol. 18, pp. 19413-19428, 2010.
- [165] D. Giavarina, "Understanding Bland Altman analysis," *Biochemia medica*, vol. 25, pp. 141-151, 2015.
- [166] T. Hinz, L.-K. Ehler, T. Hornung, H. Voth, I. Fortmeier, T. Maier, *et al.*, "Preoperative characterization of basal cell carcinoma comparing tumour thickness measurement by optical coherence tomography, 20-MHz ultrasound and histopathology," *Acta dermato-venereologica*, vol. 92, pp. 132-137, 2012.
- [167] M. R. Avanaki, R. Cernat, P. J. Tadrous, T. Tatla, A. G. Podoleanu, and S. A. Hojjatoleslami, "Spatial compounding algorithm for speckle reduction of dynamic focus OCT images," *IEEE Photonics Technology Letters*, vol. 25, pp. 1439-1442, 2013.

- [168] R. M. Haralick, "Statistical and structural approaches to texture," *Proceedings of the IEEE*, vol. 67, pp. 786-804, 1979.
- [169] I. Jolliffe, *Principal component analysis*: Wiley Online Library, 2002.
- [170] I. Guyon, J. Weston, S. Barnhill, and V. Vapnik, "Gene selection for cancer classification using support vector machines," *Machine learning*, vol. 46, pp. 389-422, 2002.
- [171] S.-i. Amari and S. Wu, "Improving support vector machine classifiers by modifying kernel functions," *Neural Networks*, vol. 12, pp. 783-789, 1999.
- [172] D. W. Hosmer Jr, S. Lemeshow, and R. X. Sturdivant, *Applied logistic regression* vol. 398: John Wiley & Sons, 2013.
- [173] B. Wu, T. Abbott, D. Fishman, W. McMurray, G. Mor, K. Stone, *et al.*, "Comparison of statistical methods for classification of ovarian cancer using mass spectrometry data," *Bioinformatics*, vol. 19, pp. 1636-1643, 2003.
- [174] P. J. Lisboa and A. F. Taktak, "The use of artificial neural networks in decision support in cancer: a systematic review," *Neural networks*, vol. 19, pp. 408-415, 2006.
- [175] K. Langer, "On the anatomy and physiology of the skin: III. The elasticity of the cutis," *British journal of plastic surgery*, vol. 31, pp. 185-199, 1978.
- [176] C.-Y. Chen, C.-A. Yu, T.-F. Hong, Y.-L. Chung, and W.-L. Li, "Contact and frictional properties of stratum corneum of human skin," *Biosurface and Biotribology*, vol. 1, pp. 62-70, 2015.
- [177] T. P. Habif, *Clinical dermatology*: Elsevier Health Sciences, 2015.
- [178] M. Liu and T. Buma, "Biometric mapping of fingertip eccrine glands with optical coherence tomography," *Photonics Technology Letters, IEEE*, vol. 22, pp. 1677-1679, 2010.
- [179] M. Ohmi, M. Tanigawa, Y. Wada, and M. Haruna, "Dynamic analysis for mental sweating of a group of eccrine sweat glands on a human fingertip by optical coherence tomography," *Skin research and technology*, vol. 18, pp. 378-383, 2012.
- [180] G. Pellacani, P. Guitera, C. Longo, M. Avramidis, S. Seidenari, and S. Menzies, "The impact of in vivo reflectance confocal microscopy for the diagnostic accuracy of melanoma and equivocal melanocytic lesions," *Journal of investigative dermatology*, vol. 127, pp. 2759-2765, 2007.
- [181] T. Tsugita, T. Nishijima, T. Kitahara, and Y. Takema, "Positional differences and aging changes in Japanese woman epidermal thickness and corneous thickness determined by OCT (optical coherence tomography)," *Skin Research and Technology*, vol. 19, pp. 242-250, 2013.
- [182] M. Nasiri-Avanaki, A. Aber, S. Hojjatoleslami, M. Sira, J. Schofield, C. Jones, *et al.*, "Dynamic focus optical coherence tomography: feasibility

-
- for improved basal cell carcinoma investigation," in *SPIE BiOS*, 2012, pp. 82252J-82252J-7.
- [183] M. R. Nasiri-Avanaki, M. Sira, A. Aber, S. A. Hojjatoleslami, J. B. Schofield, C. Jones, *et al.*, "Improved imaging of basal cell carcinoma using dynamic focus optical coherence tomography," in *JOURNAL OF INVESTIGATIVE DERMATOLOGY*, 2011, pp. S38-S38.
- [184] T. Gambichler, A. Orlikov, R. Vasa, G. Moussa, K. Hoffmann, M. Stücker, *et al.*, "In vivo optical coherence tomography of basal cell carcinoma," *Journal of dermatological science*, vol. 45, pp. 167-173, 2007.
- [185] M. Mogensen, T. JOERGENSEN, B. M. Nürnberg, H. A. Morsy, J. B. THOMSEN, L. Thrane, *et al.*, "Assessment of Optical Coherence Tomography Imaging in the Diagnosis of Non-Melanoma Skin Cancer and Benign Lesions Versus Normal Skin: Observer-Blinded Evaluation by Dermatologists and Pathologists," *Dermatologic Surgery*, vol. 35, pp. 965-972, 2009.
- [186] M. Mogensen, B. Nürnberg, J. L. Forman, J. B. Thomsen, L. Thrane, and G. Jemec, "In vivo thickness measurement of basal cell carcinoma and actinic keratosis with optical coherence tomography and 20-MHz ultrasound," *British Journal of Dermatology*, vol. 160, pp. 1026-1033, 2009.
- [187] J. M. Olmedo, K. E. Warschaw, J. M. Schmitt, and D. L. Swanson, "Correlation of thickness of basal cell carcinoma by optical coherence tomography in vivo and routine histologic findings: a pilot study," *Dermatologic surgery*, vol. 33, pp. 421-426, 2007.
- [188] T. Maier, M. Braun-Falco, T. Hinz, M. Schmid-Wendtner, T. Ruzicka, and C. Berking, "Morphology of basal cell carcinoma in high definition optical coherence tomography: en-face and slice imaging mode, and comparison with histology," *Journal of the European Academy of Dermatology and Venereology*, vol. 27, pp. e97-e104, 2013.
- [189] J. Schmitt and A. Knüttel, "Model of optical coherence tomography of heterogeneous tissue," *JOSA A*, vol. 14, pp. 1231-1242, 1997.
- [190] H. Kittler, H. Pehamberger, K. Wolff, and M. Binder, "Diagnostic accuracy of dermoscopy," *The lancet oncology*, vol. 3, pp. 159-165, 2002.
- [191] T. D. Desai, A. D. Desai, D. C. Horowitz, F. Kartono, and T. Wahl, "The use of high-frequency ultrasound in the evaluation of superficial and nodular basal cell carcinomas," *Dermatologic Surgery*, vol. 33, pp. 1220-1227, 2007.
- [192] Z. Ansari, Y. Gu, M. Tziraki, R. Jones, P. French, D. Nolte, *et al.*, "Elimination of beam walk-off in low-coherence off-axis photorefractive holography," *Optics letters*, vol. 26, pp. 334-336, 2001.

- [193] J. Richmond, "A wire-grid model for scattering by conducting bodies," *IEEE Transactions on Antennas and Propagation*, vol. 14, pp. 782-786, 1966.
- [194] A. Ludwig, "Wire grid modeling of surfaces," *IEEE Transactions on Antennas and Propagation*, vol. 35, pp. 1045-1048, 1987.
- [195] R. J. Paknys, "The near field of a wire grid model," *IEEE Transactions on Antennas and Propagation*, vol. 39, pp. 994-999, 1991.
- [196] F. Frezza, L. Pajewski, C. Ponti, and G. Schettini, "Accurate wire-grid modelling of buried conducting cylindrical scatterers," *Nondestructive Testing and Evaluation*, vol. 27, pp. 199-207, 2012.
- [197] M. Di Vico, F. Frezza, L. Pajewski, and G. Schettini, "Scattering by a finite set of perfectly conducting cylinders buried in a dielectric half-space: a spectral-domain solution," *IEEE transactions on antennas and propagation*, vol. 53, pp. 719-727, 2005.
- [198] P. Martin, "On acoustic and electric Faraday cages," in *Proc. R. Soc. A*, 2014, p. 20140344.
- [199] A. Taflove and S. C. Hagness, "Computational Electrodynamics The Finite-Difference Time-Domain Artech House," 1995.
- [200] K. Yee, "Numerical solution of initial boundary value problems involving Maxwell's equations in isotropic media," *IEEE Transactions on antennas and propagation*, vol. 14, pp. 302-307, 1966.
- [201] A. Giannopoulos, "Modelling ground penetrating radar by GprMax," *Construction and building materials*, vol. 19, pp. 755-762, 2005.
- [202] C. Charbonnier, L. Assassi, P. Volino, and N. Magnenat-Thalmann, "Motion study of the hip joint in extreme postures," *The Visual Computer*, vol. 25, pp. 873-882, 2009.
- [203] R. Stagni, S. Fantozzi, A. Cappello, and A. Leardini, "Quantification of soft tissue artefact in motion analysis by combining 3D fluoroscopy and stereophotogrammetry: a study on two subjects," *Clinical Biomechanics*, vol. 20, pp. 320-329, 2005.
- [204] A. G. Cutti, G. Paolini, M. Troncossi, A. Cappello, and A. Davalli, "Soft tissue artefact assessment in humeral axial rotation," *Gait & posture*, vol. 21, pp. 341-349, 2005.
- [205] R. Schmidt, C. Disselhorst-Klug, J. Silny, and G. Rau, "A marker-based measurement procedure for unconstrained wrist and elbow motions," *Journal of Biomechanics*, vol. 32, pp. 615-621, 1999.
- [206] L. Yahia-Cherif, B. Gilles, T. Molet, and N. Magnenat-Thalmann, "Motion capture and visualization of the hip joint with dynamic MRI and optical systems," *Computer Animation and Virtual Worlds*, vol. 15, pp. 377-385, 2004.
- [207] A. Rouhandeh, C. Joslin, Z. Qu, and Y. Ono, "Non-invasive assessment of soft-tissue artefacts in hip joint kinematics using motion capture data and ultrasound depth measurements," in *Engineering in Medicine and*

-
- Biology Society (EMBC), 2014 36th Annual International Conference of the IEEE*, 2014, pp. 4342-4345.
- [208] E. C. Fear, X. Li, S. C. Hagness, and M. A. Stuchly, "Confocal microwave imaging for breast cancer detection: Localization of tumors in three dimensions," *IEEE Transactions on Biomedical Engineering*, vol. 49, pp. 812-822, 2002.
- [209] M. Lazebnik, L. McCartney, D. Popovic, C. B. Watkins, M. J. Lindstrom, J. Harter, *et al.*, "A large-scale study of the ultrawideband microwave dielectric properties of normal breast tissue obtained from reduction surgeries," *Physics in medicine and biology*, vol. 52, p. 2637, 2007.
- [210] P. M. Meaney, D. Goodwin, A. H. Golnabi, T. Zhou, M. Pallone, S. D. Geimer, *et al.*, "Clinical microwave tomographic imaging of the calcaneus: A first-in-human case study of two subjects," *IEEE transactions on biomedical engineering*, vol. 59, pp. 3304-3313, 2012.
- [211] S. Gabriel, R. Lau, and C. Gabriel, "The dielectric properties of biological tissues: II. Measurements in the frequency range 10 Hz to 20 GHz," *Physics in medicine and biology*, vol. 41, p. 2251, 1996.
- [212] A. Peyman and C. Gabriel, "Cole–Cole parameters for the dielectric properties of porcine tissues as a function of age at microwave frequencies," *Physics in medicine and biology*, vol. 55, p. N413, 2010.
- [213] S. J. Orfanidis, "Electromagnetic Waves and Antennas, Online Book," ed, 2008.
- [214] J. R. Wait, *Electromagnetic Waves in Stratified Media: Revised Edition Including Supplemented Material* vol. 3: Elsevier, 2013.
- [215] D. Jenn, "Notes for EC3630 (Radiowave Propagation)," *Naval Postgraduate School*, 2003.
- [216] P. Bélanger, "Beam propagation and the ABCD ray matrices," *Optics Letters*, vol. 16, pp. 196-198, 1991.
- [217] I. Al-Qadi and S. Lahouar, "Measuring layer thicknesses with GPR—Theory to practice," *Construction and building materials*, vol. 19, pp. 763-772, 2005.
- [218] S. Caorsi, M. Pastorino, and M. Raffetto, "EM field prediction inside lossy multilayer elliptic cylinders for biological-body modeling and numerical-procedure testing," *IEEE transactions on biomedical engineering*, vol. 46, pp. 1304-1309, 1999.